

NORTHWESTERN UNIVERSITY

**Growth and Characterization of Si/Ge
Heterostructures on Si(001) Surface and Ge
Nano-Dots on Patterned Si(001) Surface**

A DISSERTATION

SUBMITTED TO THE GRADUATE SCHOOL
IN PARTIAL FULFILLMENT OF THE REQUIREMENTS

for the degree

DOCTOR OF PHILOSOPHY

Field of Physics and Astronomy

By

William Pascal Rodrigues

EVANSTON, ILLINOIS

December 2000

© Copyright by William Pascal Rodrigues 2000
All Rights Reserved

ABSTRACT

Growth and Characterization of Si/Ge/ Heterostructures on Si(001) Surface and Ge Nano-dots on Patterned Si(001) Surface

William Pascal Rodrigues

The epitaxial growth of Si/Ge heterostructures on the Si(001) surface has been the subject of much research because of its interesting properties and technological applications. Scientifically Ge/Si(001) is interesting because it is an ideal system to study strained heteroepitaxy. Such strained heteroepitaxial layers of Si/Ge on Si(001) can have superior device performance compared to Si based devices.

In this thesis, using x-ray synchrotron radiation, we have performed structural studies of Si/Ge heterostructures grown on Si(001) by surfactant mediated epitaxy with Bi as the surfactant. High resolution measurements were performed using the x-ray standing wave technique to characterize the structure of atomic layers in ultra-thin Ge films on Si(001). Our results indicate that the Ge atomic layers are highly commensurate with the Si substrate lattice in the in-plane direction but less so in the surface normal direction. Using grazing incidence x-ray diffraction we measured the critical thickness for pseudomorphic growth of Ge on Si(001) with Bi as surfactant to be 7 monolayers (ML). In comparison with Ge growth without Bi, segregation of Ge in the Si cap layer was suppressed and the Ge film was partially relaxed at 10 ML. Using x-ray specular reflectivity we measured the Ge-Si cap interface roughness and found it to be significantly larger for Ge film thicknesses above 7 ML.

We also investigated the morphology of Ge nano-dots grown by molecular beam epitaxy on lithographically patterned Si(001) stripe-mesas. Our atomic force

microscopy (AFM) images for Ge grown on stripe-mesas show increased uniformity in Ge nano-dot size, shape, and orientation compared with Ge nano-dots grown on a planar Si(001) surface. On stripe-mesas we also observed preferential growth of Ge nano-dots along the edges of the stripe-mesas.

Acknowledgments

I would like to thank my advisor Prof. Michael Bedzyk for his constant encouragement, guidance and support. This thesis work would not have been possible without the generous financial support from Argonne National Laboratory and for that I am grateful to Dr. Wenbing Yun and Dr. Barry Lai. Wenbing Yun and Michael Bedzyk introduced me to the Advanced Photon Source at ANL.

At Northwestern University I would like to thank all my coworkers especially Tien-Lin Lee and Osami Sakata for all their help and advice. I am also thankful to Prof. John Ketterson and his group for introducing me to electron-beam lithography and photolithography and for the free use of those facilities in their lab.

At ANL I would like to thank the SR1-2 staff members, postdoctoral fellows, technicians and outside users, in particular Wenbing Yun, Barry Lai, Zhonghou Cai, and Peter Ilinski, for introducing me to the new and exciting field of x-ray microscopy. I am also thankful to Derrick Mancini and Yong Chu for their advice and Joseph Arko for all his valuable help. I would also like to thank Peter Baldo from MSD-ANL for performing the RBS measurements.

I am thankful to all my friends at Northwestern for making my stay very pleasurable and memorable one. Finally I am very grateful to my family for their support. I dedicate this thesis to my parents.

Dedicated to my parents

Ursula and Pascal Ludrick

Contents

Abstract	iii
Acknowledgments	v
1 Introduction	1
2 Brief Overview of Ge/Si(001)	4
2.1 Introduction	4
2.2 Epitaxial Growth Modes	4
2.3 Epitaxial growth of Ge on Si(001)	6
2.4 Epitaxial Growth of Si on Ge	8
2.5 Surfactant Mediated Epitaxy	8
3 Experimental Techniques	11
3.1 Introduction	11
3.2 XSW Technique	11
3.2.1 XSW Experimental Setup	18
3.3 GIXD	22
3.4 X-ray Specular Reflectivity	24
3.4.1 Experimental Setup for GIXD and x-ray reflectivity mea- surements	26
4 Sample Preparation and Standard Characterization	28

4.1	Preparation of Si Substrates for X-ray Experiments	28
4.2	Preparation of Lithographically Patterned Si Surfaces	29
4.2.1	Photolithography	30
4.2.2	E-beam Lithography	31
4.2.3	Etching	33
4.3	UHV Chamber and MBE Growth	34
4.3.1	MBE Surface Science Chamber	34
4.3.2	MBE growth	39
4.4	<i>In situ</i> LEED and AES Studies	40
4.4.1	Clean Si(001) surface	40
4.4.2	Bi terminated Si(001) surface	42
4.5	Ge Coverage Calibration	44
5	X-ray Scattering Studies	49
5.1	Introduction	49
5.2	Previous GIXD Studies	50
5.3	GIXD and Reflectivity Results	51
6	X-ray Standing Wave Studies	62
6.1	Introduction	62
6.2	Structural models	63
6.2.1	Fixed bond length model	64
6.2.2	Strained Ge layer model based on elasticity theory	65
6.2.3	Relaxed Ge layer Model	66
6.3	XSW Results and Discussions for Ge	66
6.3.1	Model 1 for Static Debye-Waller Factor	80
6.3.2	Model 2	81
6.3.3	Effect of surfactant	87
6.3.4	XSW (008) Measurement	89

6.4	XSW Results of Si Cap	90
6.4.1	X-ray evanescent wave effect	90
7	Ge Growth on Patterned Si(001)	98
7.1	Introduction	98
7.2	Electronic properties	98
7.3	Self assembled Ge island growth on Si(001)	99
7.3.1	Island distribution	99
7.3.2	Lateral ordering	101
7.3.3	Vertical ordering	103
7.4	Growth of Ge on patterned Si(001)	105
7.4.1	Growth on stripe-mesas	107
7.4.2	Growth on square-mesas	108
7.5	<i>In situ</i> LEED Studies	110
7.5.1	Coverage dependence	110
7.5.2	Temperature dependence	112
7.6	Morphology Studies	115
8	Summary	123
8.1	Thesis Summary	123
8.2	Future Work	125
	References	126
	Appendices	133
A	Shiraki Etch for Si	134
A.1	CP4 Etch	134
A.2	Shiraki Etch	134
B	MBE Control System	136

List of Tables

1	Measured coverages of Ge for all the samples. *No Bi was used for this sample.	47
2	Results of (004) and (022) XSW measurements for the Ge for all samples	68
3	Results of (004) XSW measurements for the Si cap. ^a Measured values, ^b from continuum elasticity theory and ^c based on measured Ge P_{004} values.	97

List of Figures

1	Growth modes in epitaxy: Frank–van der Merwe (FM), Volmer–Weber (VW) and Stranski–Krastanov (SK).	5
2	After Mo <i>et al</i> [18]. STM images of single “hut” cluster. (a) Perspective plot. Scan area $400 \text{ \AA} \times 400 \text{ \AA}$. (b) Curvature mode grey scale plot. The inclined surfaces are $\{105\}$ facets.	7
3	Schematic of XSW technique using Bragg reflection from perfect crystals. The period of the XSW field is equal to the d–spacing for the diffraction planes.	12
4	From reference [54]. (a) the real and imaginary part of the E–field ratio E_H/E_0 as a function of the relative Bragg angle. (b) the phase v of the E–field ratio. (For the symmetric Si(004) reflection at the photon energy of 12 keV). The above is for the origin defined in figure 5 for the Si unit cell.	15
5	The unit cell for bulk Si. The cubic unit cell has 8 Si atoms. The coherent position P_H are measured with respect to the origin placed at the center of symmetry as shown.	17
6	Side–view (except for the Ge fluorescent detector) schematic of the XSW setup at the 5IDC station at APS. The L–N ₂ cooled Si(111) monochromator is 30 m from the undulator. The other components starting with ion chamber IC1 sitting on a optical table in the front end of the 5ID-C hutch are approximately 55 m from the undulator.	19
7	DuMond diagram (a) for the x–ray optics used for XSW measurements, (b) for Si(004) reflection and (c) for Si(022) reflection. X–axis is the incident angle in μrad and Y–axis is the wavelength.	20
8	Schematic diagram for GIXD. In our GIXD experiments $\alpha_i = \alpha_f$	23
9	Schematic diagram for x–ray specular reflectivity. $\alpha > \alpha_c$	24

10	Schematic of experimental setup for GIXD and x-ray reflectivity at APS.	27
11	Partial pressures for residual gases inside the chamber under UHV conditions. The H ₂ partial pressure is 2×10^{-10} torr.	35
12	Schematic side-view of the MBE chamber. All the essential ports are shown. The LEED port is out of the plane of the paper while the STM port is diametrically opposite to the LEED.	36
13	An isometric view of the manipulator head. The manipulator is machined out of Mo. The two sample holder plates for direct and indirect sample heating are also shown.	38
14	2-domain 2×1 LEED pattern of clean Si(001) surface.	41
15	Auger spectrums for clean and unclean Si(001) surfaces. Note that for clean surface the sensitivity was increased by a factor of 10 for $E > 130$ eV.	42
16	Bi(NOO)/Si(LMM) Auger intensity ratio as a function of substrate temperature. Bi coverage beyond 400°C decreases linearly with temperature.	44
17	(a) 2-domain $2 \times n$ LEED pattern for Bi terminated Si(001) surface, resulting from missing Bi dimer as shown in (b). Atoms in the second layer form a dimer at that site. With $n \sim 5$, the coverages is estimated to be $1 - 1/n$ about 0.8 ML.	45
18	Atomic view of Si/Ge growth on Si(001) with Bi as the surfactant. (a) Bi dimers on Si(001) surface after 1ML Bi coverage. (b) after Ge deposition on Bi covered surface, and (c) after Si deposition following Ge growth. Driven by the surface free energy minimization, Bi segregates to the growth surface and forms a Bi-Bi dimer at each stage.	46
19	Calibration of Ge coverage by exciting Ge K α fluorescence. Solid lines are Gaussian fits to the data (points). The Ge coverage is proportional to the area under the peak.	48
20	Scattering depth Λ for 11 keV x-rays as function of L. The incident and exit angles are equal.	52

21	<i>H, K</i> scans through (22 <i>L</i>) with $L = 0.01$ for Si/Ge layers with a) 10.0 ML of Ge grown with Bi and b) 10.0 ML of Ge grown without Bi. The scans are shifted vertically for clarity. The inset represents the scanning in reciprocal space.	54
22	<i>H, K</i> scans through (22 <i>L</i>), with $L = 0.04$ for a) 10.0 ML Ge without Bi, b) 10.0 ML Ge with Bi, c) 7.1 ML Ge with BI and d) 1.7 ML Ge with Bi.	55
23	<i>H, K</i> scans through (22 <i>L</i>), with various values of L for sample with 10.0 ML of Ge coverage grown with Bi. The scans are shifted vertically for clarity.	56
24	X-ray reflectivity data (points) and model fits (lines) for a) 7.1 ML Ge grown with Bi b) 10.0 ML of Ge grown with Bi. For 10 ML of Ge without Bi only the data is shown.	58
25	Scattering depth Λ for 11 keV x-rays as function of L . The incident and exit angles are equal.	59
26	Positions of various Ge layers above the Si substrate. The bulk Si(004) diffraction planes, where $P_{004} = 0$, are represented by the dashed lines.	64
27	Two structural models for Ge epitaxial growth on Si; (a) bond lengths conserved, (b) continuum elasticity theory model.	65
28	Calculated coherent position of Ge for (a) fixed bond length model, (b) elastic model (c) relaxed Ge model as a function of coverage. . .	67
29	Angular dependence of (004) (top) and (022) (bottom) XSW data and best fit (solid lines) for normalized Ge $K\alpha$ and fluorescence yield and reflectivity for 1.6 ML Ge grown with Bi on Si(001).	69
30	Angular dependence of (004) (top) and (022) (bottom) XSW data and best fit (solid lines) for normalized Ge $K\alpha$ and fluorescence yield and reflectivity for 1.1 ML Ge grown on Si(001).	70
31	Angular dependence of (004) (top) and (022) (bottom) XSW data and best fit (solid lines) for normalized Ge $K\alpha$ and fluorescence yield and reflectivity for 3.4 ML Ge grown with on Si(001).	71
32	Angular dependence of (004) (top) and (022) (bottom) XSW data and best fit (solid lines) for normalized Ge $K\alpha$ and fluorescence yield and reflectivity for 3.0 ML Ge grown with Bi on Si(001).	72

33	Angular dependence of (004) (top) and (022) (bottom) XSW data and best fit (solid lines) for normalized Ge $K\alpha$ and fluorescence yield and reflectivity for 7.1 ML Ge grown with Bi on Si(001).	73
34	Angular dependence of (004) (top) and (022) (bottom) XSW data and best fit (solid lines) for normalized Ge $K\alpha$ and fluorescence yield and reflectivity for 4.6 ML Ge grown with Bi on Si(001).	74
35	Angular dependence of (004) (top) and (022) (bottom) XSW data and best fit (solid lines) for normalized Ge $K\alpha$ and fluorescence yield and reflectivity for 10.0 ML Ge grown with Bi on Si(001).	75
36	Angular dependence of (004) (top) and (022) (bottom) XSW data and best fit (solid lines) for normalized Ge $K\alpha$ fluorescence yield and reflectivity for 1.7 ML Ge grown with Bi on Si(001).	76
37	Ge (004) and (022) measured positions (markers) and calculated positions (lines) using continuum elasticity theory as a function of Ge coverage.	77
38	Ge (004) and (022) measured coherent fractions (markers) and calculated coherent fractions (lines) using continuum elasticity theory as a function of Ge coverage.	79
39	Calculated values of static DW factor and σ_{004} as a function of Ge coverage.	81
40	Calculated values of static DW factor and σ_{022} as a function of Ge coverage.	82
41	Atomic distributions for Ge layers grown on Si(001) using Bi as the surfactant. (a) Ideal model with each layer uniformly strained and no defects. Each layer is designated by a delta-function. The dotted lines are positions that Si atoms would occupy. (b) A Gaussian distribution for layers to incorporate defects within a layer used in model 2. The width of the distribution increases linearly with the layer number.	84
42	Fits to data (dots) for F_{004} and F_{022} using non-uniform static Debye-Waller factor as in model 2.	85
43	Angular dependence of (004) XSW data (markers) and best fit (solid lines) for Ge $K\alpha$ fluorescence yield and reflectivity for 1.6 ML Ge with Bi and 1.1 ML without Bi on Si(001).	88

44	Angular dependence of (004) (top) and (008) (bottom) XSW data and best fit (solid lines) for normalized Ge $K\alpha$ and fluorescence yield and reflectivity for 1.7 ML Ge grown with Bi on Si(001).	91
45	X-ray evanescent wave emission effect to probe surface layers.	92
46	Escape depth of Si $K\alpha$ fluorescence in Si as function of take-off angle. 93	
47	XSW cap measurements for 1.6 ML Ge coverage (top) and 1.1 ML Ge coverage (bottom) performed at 8.0 keV.	95
48	XSW cap measurements for 3.4 ML Ge coverage (top) and 3.0 ML Ge coverage (bottom) performed at 8.0 keV.	96
49	After Williams <i>et al</i> [76] (a) Atomic force microscope topograph of a 13 eq-ML film of Ge deposited onto Si(001) and annealed for 30 min at 550°C. The gray scale is keyed to the local facet angle with respect to the substrate plane, with darker shades corresponding to steeper angles. Pyramids, domes and superdomes are readily recognized by both their size and shading. (b) scatter plot showing the exposed surface area of the islands versus their volumes on a $1\ \mu\text{m}^2$ area for the same sample as in part a. Each island shape forms a family of points on the graph, allowing the members of each family to be identified for statistical analysis.	102
50	Schmidbauer <i>et al</i> [90], (a) Power spectrum of AFM micrograph and (b) GISAXS intensity profile along $\langle 100 \rangle$ and $\langle 110 \rangle$ for $\text{Si}_{1-x}\text{Ge}_x$ ($x = 0.25$) islands on Si(001).	104
51	Tersoff <i>et al</i> [64], AFM images of $\text{Si}_{0.25}\text{Ge}_{0.75}/\text{Si}$ superlattices. Scanning direction is $[110]$. (a) $0.8\ \mu\text{m} \times 0.8\ \mu\text{m}$ image after deposition of the first alloy layer;(b) $1.25\ \mu\text{m} \times 1.25\ \mu\text{m}$ image after deposition of the 20th alloy layer.	106
52	Kamins <i>et al</i> [93], AFM images of Ge islands grown on Si stripe-mesas showing ordering of several rows of Ge islands near the edges of the flat Si(001) surface. Widths of Si(001) surface: (a) 670 nm, (b) $1.0\ \mu\text{m}$, (c) $1.7\ \mu\text{m}$	109
53	Jin <i>et al</i> [96], (a) A 3D AFM image with four Ge islands located at the corners on square mesa with the base lines parallel to the $\langle 110 \rangle$ directions. The Ge thickness is 9 ML. (b) A 3D AFM image with five Ge islands with 10 ML Ge. The fifth pyramidal island is formed in the central region.	111

54	LEED images after various coverages of Ge. (a) clean Si surface, 2-domain 2×1 reconstruction, (b) after 3 ML of Ge $2 \times n$ reconstruction; cont'd. in figure ??	113
55	LEED images after various coverages of Ge, cont'd. from figure ?? (c) after 5 ML of Ge additional spots with 4-fold symmetry due to the faceted surfaces on the islands appear, (d) after 12 ML of Ge the reconstruction is similar to (c) with higher intensity in the spots from faceted surfaces.	114
56	(a) LEED image of clean Si(001) surface. (b)–(f) LEED images after annealing the the sample at temperatures indicated. The Ge coverage was fixed at 10 ML. All the LEED images were taken at RT.	116
57	AFM micrograph of Si surface patterned into a column of stripe-mesas by e-beam lithography and RIE.	117
58	AFM micrograph of Ge islands on unpatterned Si(001) surface. The Ge coverage is about 15 ML.	118
59	AFM micrograph of Ge islands on patterned Si(001) surface. The island rows are along $\langle 110 \rangle$ direction. The Ge coverage is about 10 ML.	119
60	High resolution AFM micrograph of Ge islands on patterned Si(001). The edges are along $\langle 110 \rangle$ direction. The Ge coverage is about 10 ML.	121
61	Control system for the LEED imaging, Auger, RGA, and sample and Knudsen cell heating on the UHV-MBE system.	138

Chapter 1

Introduction

The epitaxial growth of Ge on Si is a classical system for the study of strained layered heteroepitaxy. This system is interesting both scientifically and technologically. Since both Ge and Si are group IV elements, they have very similar chemical and physical properties. The most important physical difference between them is the difference between their lattice constants. Thus the Ge/Si system is an ideal system to study the role of strain in heteroepitaxy.

Technologically Si is to date the most important semiconductor material used for making electronic devices. For more than half a century after the invention of the transistor, Si has been extensively studied. The demand for better, faster and smaller devices is continuously increasing. The current Si device dimensions are approaching their limits. Further improvements can be achieved by using different materials with higher electron and hole mobilities. The III-V compound semiconductors, like GaAs, offer higher electron mobilities than Si and have been used to make much better devices. In spite of their superior performance III-V semiconductors are not considered to be effective replacements for Si because of processing difficulties.

On the other hand, Ge–Si heterostructure based devices have the potential to replace Si devices because they can have better performance and they require small modifications to existing Si processing techniques. SiGe alloy based discrete devices are already in commercial production. Still, SiGe heterostructures are not suitable for device integration due to large number of defects resulting from the lattice misfit. A significant amount of current research on Si–Ge systems is focused towards growing high quality heteroepitaxial structures needed for device integration. Recently Ge/Si has attracted much attention because of its ability to form uniform and coherent nanometer sized islands called quantum dots. These quantum dots have novel electronic and optical properties which are currently being explored for making new devices that offer much superior performance.

Due to both technological applications and interesting properties Ge/Si(001) system has been extensively studied in the last decade. In this thesis we did structural studies of Si/Ge heterostructures on Si(001) grown by Molecular Beam Epitaxy (MBE). The growth of Ge on Si(001) is modified in the presence of surfactants. In our studies we used Bi as a surfactant. In addition to standard surface science techniques, the structural studies featured the use of x-ray synchrotron based techniques. We also studied the morphology of Ge islands grown on patterned Si(001) surface by atomic force microscopy (AFM).

In chapter 2, I will give an overview of the Ge/Si system. I will give a brief review of past research performed, on the Ge/Si system and the status of current research.

In chapter 3, I will discuss the experimental techniques I used to perform structural studies. I will discuss the x-ray standing wave (XSW) technique, grazing incidence x-ray diffraction (GIXD) and x-ray reflectivity that I used to probe the layer

by layer structure of Ge layers grown on Si(001) with Bi as the surfactant. The x-ray studies were performed at the 5ID-C undulator and 2BM-B bending-magnet beamlines of the Advanced Photon Source (APS) located at Argonne National Laboratory.

In chapter 4, I will present my sample preparation methods. I will discuss photolithography, electron beam lithography and reactive-ion etching (RIE) techniques that I used to pattern my Si(001) surface. I will then introduce our MBE chamber that I used to grow my samples, both planar heterostructures and Ge islands on patterned Si. In this chapter I will also discuss my *in situ* surface analysis during the growth of my samples with low energy electron diffraction (LEED) and Auger electron spectroscopy (AES). I will also discuss the calibration of Ge coverage with Rutherford back-scattering (RBS) and x-ray fluorescence.

In Chapter 5, I will discuss my GIXD and x-ray reflectivity studies performed on Ge layers buried under Si and grown with Bi as surfactant. Our studies directly measured the increase in the critical thickness of Ge on Si(001) due to Bi. Some comparisons with Ge grown without Bi will also be included. The XSW results on same samples will be discussed in chapter 6. Here, I will present two models that can explain my XSW results and are also consistent with my GIXD and x-ray reflectivity studies.

In chapter 7, I will discuss a very new field of research in directed self assembly of nano-structures in which I grew Ge nano-dots (also known as quantum dots) on patterned Si. I will give an overview of the work done on this system so far. My *in situ* LEED studies of growth of Ge islands on Si will be shown. I will also present the morphology studies of Ge islands by AFM. I will conclude and summarize in chapter 8.

Chapter 2

Brief Overview of Ge/Si(001)

2.1 Introduction

In the late 1960s and early 1970s there were many attempts at growing $\text{Ge}_x\text{Si}_{1-x}$ multilayers for device applications, but they suffered from poor interfacial quality due to the 4.2% lattice misfit between Ge and Si. The interest in growth of pure Ge strained films on Si increased dramatically first after Copel *et al* [1] showed that with the use of surfactants, 2D growth of Ge on Si can be improved and then soon after Eaglesham and Cerullo showed that Ge grows into 3D islands that are initially dislocation free [2].

2.2 Epitaxial Growth Modes

Epitaxial growth has been classified into three different growth modes [3]: Frank–Van der Merwe (FM) [4], Volmer–Weber (VW) [5], and Stranski–Krastanov (SK) [6]. Respectively, they are briefly described as 2D or layer–by–layer growth, 3D or island growth and layer–by–layer plus island growth (see figure 1). In general terms the growth mode for a given system depends on the lattice mismatch and the

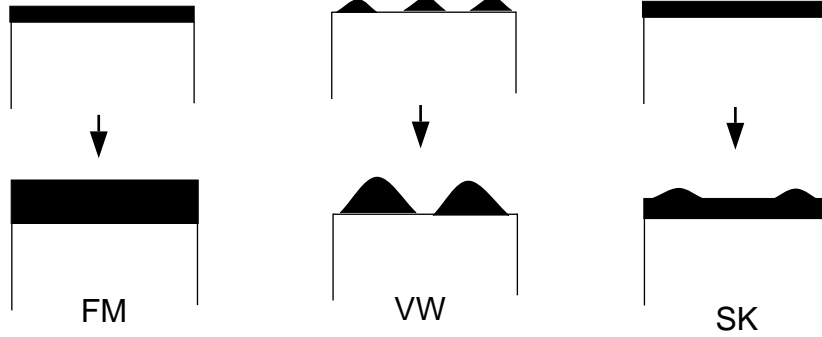


Figure 1: Growth modes in epitaxy: Frank–van der Merwe (FM), Volmer–Weber (VW) and Stranski–Krastanov (SK).

interface and surface free energies [7].

Consider heteroepitaxial growth consisting of two different materials A and B. Let γ_A and γ_B be their surface free energies and γ_{AB} be their interface free energy. The interface free energy can be written as $\gamma_{AB} = \gamma_{AB}^c + \gamma_{AB}^0$, where the first term is the strain contribution and the second term is due to the chemical interaction between A and B (review in refer [8]). The growth of A on B depends on the total energy of the system written as

$$\gamma_{tot} = \gamma_A + \gamma_{AB}^c + \gamma_{AB}^0 \quad (1)$$

If $\gamma_{tot} \leq \gamma_B$ for any thickness then A will wet the surface of B and grow in FM mode. This is always true for homoepitaxy because $\gamma_{AB} = 0$. For the heteroepitaxy of lattice–matched systems $\gamma_{AB}^c = 0$ and therefore the inequality is satisfied if γ_{AB}^0 is negligible and $\gamma_A < \gamma_B$.

For the heteroepitaxy of systems with lattice mismatch even if $\gamma_A < \gamma_B$ the strain contribution γ_{AB}^c increases with thickness and after a certain critical thickness called d_{SK} , $\gamma_{tot} > \gamma_B$ and island or 3D growth begins. This mode of growth

is called SK growth. If $\gamma_A > \gamma_B$ then $\gamma_{tot} > \gamma_B$ is always true and the growth is purely 3D. This growth mode is VW growth.

2.3 Epitaxial growth of Ge on Si(001)

The growth of Ge on Si(001) is in Stranski–Krastanov mode [9, 10]. The surface free energy for Ge is less than Si by 0.07 eV/atom [11], ($\gamma_{Ge} < \gamma_{Si}$). The lattice mismatch between Ge and Si (4.2%) therefore leads to SK mode of growth for Ge on Si. Early studies of Ge growth on Si(001) gave conflicting values for critical thickness. Reflective high energy electron diffraction (RHEED) studies showed island formation after $\sim 10 \text{ \AA}$ of Ge growth with critical thickness to be about 6 ML [14]. Auger electron spectroscopy (AES) indicated that the thickness for island formation to be 3 ML [15, 10]. The discrepancies in the various reported values is probably because of the difference in growth conditions and the difference in the techniques used to determine d_{SK} . It is now more or less accepted that the critical thickness is 3 ML. The critical thickness for Ge growth on Si(001) given by Matthews and Blakeslee theory [12] from total energy (strain the dislocation) minimization is ~ 3 ML. Using an equilibrium thermodynamics model which takes into account surface free energy and the onset of island formation, Tersoff calculated the same value [13].

Continued growth beyond the 3 ML wetting layer results in the formation of islands. Earlier it was believed that the islands had dislocations as the observation of incoherent interface and strain relaxation coincided with island formation [9, 16]. Later transmission electron microscopy (TEM) studies showed that onset of island formation is before the onset of dislocations and the islands are coherent up to

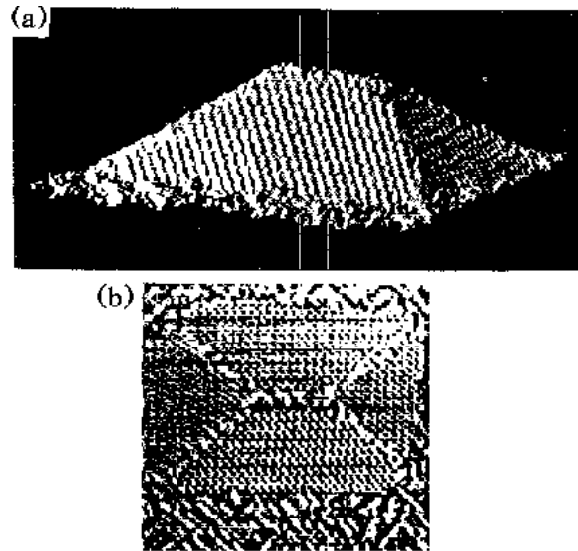


Figure 2: After Mo *et al* [18]. STM images of single “hut” cluster. (a) Perspective plot. Scan area $400 \text{ \AA} \times 400 \text{ \AA}$. (b) Curvature mode grey scale plot. The inclined surfaces are $\{105\}$ facets.

1000 \AA in diameter and 500 \AA in thickness [2]. Williams *et al* showed by x-ray diffraction that the islands are relaxed [17]. The coherent island relaxation is achieved by local deformation of the Si substrate [2].

Mo *et al* studied the transition from 2D to 3D growth with *in situ* scanning tunneling microscopy (STM) [18]. They first showed that initially the islands have a $\{105\}$ faceted structure with rectangular base as shown in figure 2. They called the faceted islands as “hut” clusters. The principle axes of the huts are along the $\langle 100 \rangle$ directions. These hut clusters are metastable and upon annealing form larger stable islands similar to those seen in reference [2]. At the Ge/Si interface the huts are completely strained but relax to bulk Ge lattice at the top [19]. Recently it was found that although rectangular shaped huts are metastable, square shaped pyramids are stable with respect to annealing [20]. The islands formation will be discussed further in chapter 7.

2.4 Epitaxial Growth of Si on Ge

Si growth on Ge is important for growing Si/Ge superlattice structures and for heterojunction bipolar transistors. Compared to Ge growth on Si, growth of Si on Ge is relatively less studied. Since Ge growth on Si is in SK mode it follows from equation 1 that Si growth on Ge is in VW mode [10, 22, 21]. Earlier studies of growing Si/Ge heterostructures on Si(001) have shown significant segregation of Ge into Si while Si capping has resulted into Si island formation on Ge [23, 24].

2.5 Surfactant Mediated Epitaxy

The fundamental thermodynamic limitations imposed by the previously described different growth modes can be circumvented by modifying the energetics at the growth surface. It was realized that one has to restrict the kinetics at the growth surface to prevent island formation in SK and VW growth [7]. One possibility is to perform growth at lower substrate temperatures [25, 26]. At lower temperatures due to lower surface diffusion island formation is suppressed but at the expense of poor crystal quality for the films.

Copel *et al* [1] found an elegant way to modify the kinetics at the growth surface by using surface-active-species which they called “surfactants”. They used As for a surfactant to grow Si/Ge/Si(001) heterostructures. They observed that As suppressed island formation and Ge segregation in Si without sacrificing epitaxial quality. They attributed this effect to the reduction in the surface free energies of both Ge and Si by As. Due to the As termination of the surface the total energy of the system given in equation 1 is significantly reduced as $\gamma_{As} \ll \gamma_{Ge}, \gamma_{Si}$.

Although surfactants reduce the surface energy, later it was correctly pointed

out by several researchers that island formation and Ge segregation in Si is suppressed because the diffusion of atoms on the growth surface is reduced by the surfactant [27, 28, 30]. For Ge growth below d_{SK} predeposition or coevaporation of the surfactant is found to be not important [29]. High temperature annealing leads to island formation suggesting that 2D growth in the presence of surfactant is metastable [30].

Although the thermodynamics of SME is now very well known, the mechanism at the atomic level of how surfactants work is not very well known. Group V elements like As [1, 31], Sb [31], and Bi [40, 41] have been effective in suppressing island formation, while group III elements have not been shown to be effective. In fact some studies have shown group III elements like Ga and In enhance diffusivity in Si homoepitaxy and promote 3D islanding in Ge/Si heteroepitaxy [32]. It is also very well known that group V elements passivate the Si(001) surface by saturating the two dangling bonds [33, 34]. Photoemission studies have shown that the top Si surface layer is in bulk-like atomic positions when Si(001) is terminated with a group V adsorbate [34]. All these studies indicate that effectiveness of a surfactant in preventing 3D growth depends on how well it can “float” on the surface by incorporating growth species below the surface. Several exchange models between the surfactant species and the growth species have been proposed for As and Sb as surfactants. A two-dimer correlated exchange mechanism model by Tromp *et al* [35] proposed that initially Ge breaks the As dimers before exchanging sites. Another model by Yu *et al* [36] proposed that the Ge dimers are formed in between the As dimer rows before Ge exchanging positions with As. To date there is no conclusive experimental evidence for any of the models proposed.

As and Sb are the two most studied surfactants. With As the Ge films have been shown to be pseudomorphic up to 8 ML [37]. With Sb the critical thickness

increased to 11 ML [38]. Formation of islands is suppressed even beyond 50 ML of Ge growth on Si(001) with As and Sb as surfactants. Sb has the advantage of being less volatile and can be used over a wide range of temperatures.

Besides As and Sb, there are reports of other group V element Bi [40], group VI element Te [42], and group IV elements Sn [43] and Pb [44] used as surfactants. Although As and Sb are very effective as surfactants they also act as n-type dopants. There are no reports of group III elements being effective in increasing the critical thickness although Ga has been used to prevent Ge segregation in Si [39]. There is therefore a lack of surfactant to grow p-type Ge layers. A means to circumvent this problem is to grow ultra-pure Ge layers and dope them later with p-type dopants. Group IV element Pb and Sn are less effective as surfactants. The solubility of Bi and Te is at least two orders of magnitude lower than that of As, Sn or Sb. The drawback of Te is that it can be used only at temperatures below 300°C [45] as it completely desorbs at higher temperatures and therefore may not be very effective.

Bi on the other hand may be the most effective surfactant for growing pure Ge strained films on Si(001). Although it has been shown to prevent 3D islanding and Ge segregation [40] and has also been used to grow thick relaxed Ge layers on Si(111), [46] very little is known about how effective Bi is in growing strained Ge layers on Si(001). The advantages of Bi are: it has very low solubility in Ge and Si and it can be used up to a substrate temperature of 550°C. In this thesis we investigated the effectiveness of Bi as a surfactant in growing strained buried Ge layers on Si(001).

Chapter 3

Experimental Techniques

3.1 Introduction

The structural characterization of the MBE grown Si/Ge/Si(001) samples was performed *ex situ* by X-ray standing wave (XSW), grazing incidence x-ray diffraction (GIXD) and x-ray reflectivity measurements using synchrotron radiation. In this chapter I will discuss these techniques.

3.2 XSW Technique

The XSW technique is based on the dynamical diffraction of x-rays. The XSW technique was first demonstrated by Batterman [52]. He used dynamical Bragg diffraction to produce the XSW field within a Ge single crystal. Zegenhagen has reviewed the XSW technique and its application [53]. In this section I will give a brief review of the XSW technique as applied to the case of determining the positions of atoms that reside above the surface of a diffracting single crystal.

In general when two coherently coupled plane waves, with wave vectors \mathbf{K}_0 and \mathbf{K}_H where $|\mathbf{K}_0| = |\mathbf{K}_H| = 1/\lambda$, interfere, they produce a standing wave field. The

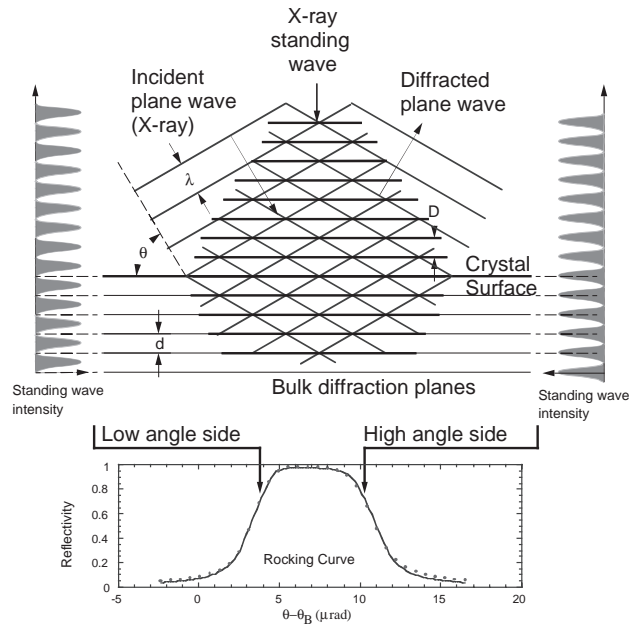


Figure 3: Schematic of XSW technique using Bragg reflection from perfect crystals. The period of the XSW field is equal to the d -spacing for the diffraction planes.

period T of this standing wave field is then given by

$$T = \frac{\lambda}{2 \sin \theta} \quad (2)$$

where 2θ is the angle between \mathbf{K}_0 and \mathbf{K}_H . The standing wave pattern will shift by a single period every time the phase between \mathbf{K}_0 and \mathbf{K}_H is changed by 2π radians. The above generalization is strictly true for two plane waves interfering in vacuum.

There are several ways to make two coherent x-ray beams interfere with each other. The most frequently used method is to use Bragg reflection from a perfect single crystal. That is also the method I used in this thesis for my XSW measurements and I will only discuss that. For perfect crystals neglecting absorption the reflectivity is close to unity at the Bragg condition and therefore the interference

effect is maximum. For a Bragg reflection $\lambda = 2d_H \sin \theta$ where d_H is the lattice spacing of the planes satisfying the Bragg condition, and therefore the period T of the XSW field is equal to d_H . As shown in figure 3, the phase difference between the incident and the diffracted beam changes by 180° as the angle is scanned from the low angle side of the Bragg reflection to high angle side, and therefore the XSW pattern shifts inwards into the crystal by one-half of d_H . Since the photo-effect cross-section is (in the dipole approximation) proportional to the E-field intensity at the center of an atom, the photoelectron, Auger and fluorescent yields from adatoms residing in this XSW field are thus modulated as the angle is scanned through the Bragg reflection. From this modulation the position of the adatoms with respect to the the H planes can be very accurately determined.

For the Bragg diffraction condition the incident and the diffracted electric field (E-field) plane waves can be written as:

$$\mathbf{E}_0 = E_0 e^{2\pi i(\nu t - \mathbf{K}_0 \cdot \mathbf{r})} \quad (3)$$

for the incident wave and

$$\mathbf{E}_H = E_0 e^{2\pi i(\nu t - \mathbf{K}_H \cdot \mathbf{r})} \quad (4)$$

for the diffracted wave. Where ν is the wave frequency and \mathbf{K}_0 and \mathbf{K}_H are the incident and the diffracted wave vectors inside the crystal and are related to the reciprocal lattice vector by the Bragg diffraction condition:

$$\mathbf{K}_H = \mathbf{K}_0 + \mathbf{H} \quad (5)$$

In this thesis the x-rays used were σ polarized i.e the incident and the diffracted

E-field vectors are collinear. For σ polarization the total E-field can be written as

$$\mathbf{E}_{\mathbf{T}} = E_0 e^{-2\pi i \mathbf{K}_0 \cdot \mathbf{r}} [1 + |(E_H/E_0)| e^{iv - 2\pi i \mathbf{H} \cdot \mathbf{r}}] \quad (6)$$

where we have dropped the frequency term $e^{2\pi i \nu t}$ for convenience and written $E_H/E_0 = |E_H/E_0| e^{iv}$. If R is the reflectivity then $R = |E_H/E_0|^2$. Then the total E-field intensity, can be written as

$$I = \mathbf{E}_{\mathbf{T}} \cdot \mathbf{E}_{\mathbf{T}}^* = |E_0|^2 [1 + R + 2\sqrt{R} \cos(v - 2\pi \mathbf{H} \cdot \mathbf{r})] e^{-\mu_e z} \quad (7)$$

where μ_e is the effective linear absorption coefficient of the primary x-rays and takes into account normal x-ray absorption and the extinction effect. Figure 4 shows the plots for the real and imaginary part and the phase v of the E-field amplitude ratio E_H/E_0 around the Bragg angle calculated from dynamical diffraction theory [54]. The phase of the reflected beam relative to the incident beam changes by 180° as the angle is scanned from the low angle side of the Bragg peak to high angle side.

From x-ray dynamical diffraction the angular width of the reflectivity curve or the ‘‘Darwin width’’, henceforth referred to as the rocking curve (RC) width is given by

$$\omega = \frac{2\Gamma F'_H}{\sqrt{|b|} \sin 2\theta_B} \quad (8)$$

where $\Gamma = r_e \lambda^2 / \pi V_c$, $r_e = 2.82 \times 10^{-5} \text{ \AA}$ is the classical electron radius and V_c is the volume of the unit cell; F'_H is the real part of the structure factor $F_H = F'_H + iF''_H$ for the \mathbf{H} Bragg reflection and b is the asymmetry factor also called the ‘‘b-factor’’ and is given by

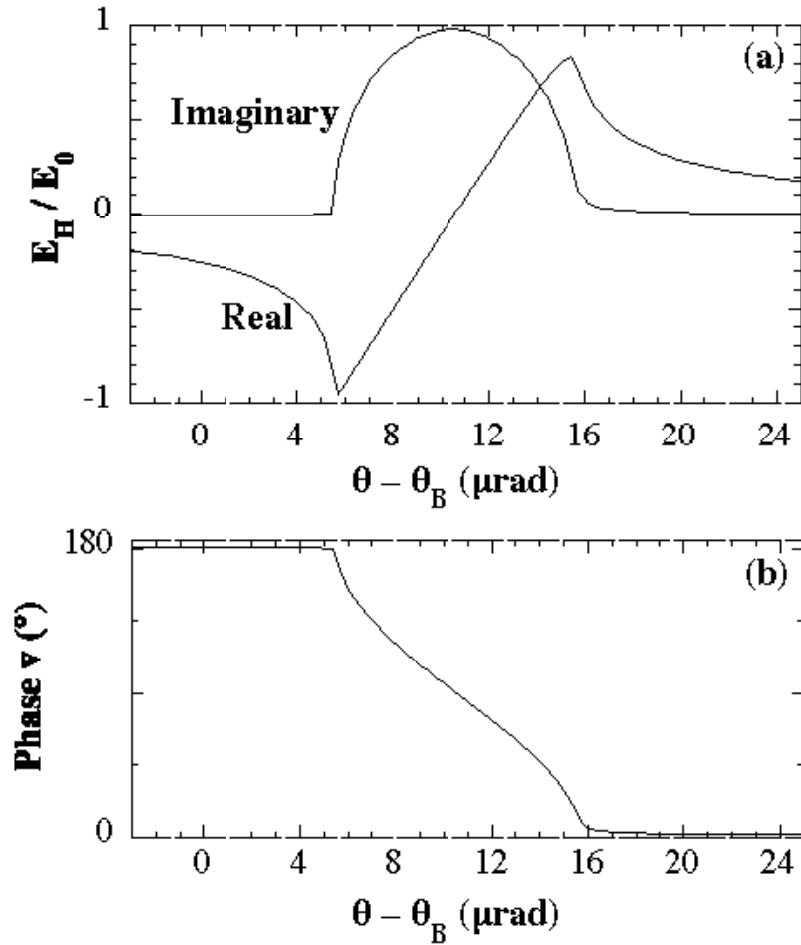


Figure 4: From reference [54]. (a) the real and imaginary part of the E-field ratio E_H/E_0 as a function of the relative Bragg angle. (b) the phase v of the E-field ratio. (For the symmetric Si(004) reflection at the photon energy of 12 keV). The above is for the origin defined in figure 5 for the Si unit cell.

$$b = \frac{-\sin(\theta_B - \phi)}{\sin(\theta_B + \phi)} \quad (9)$$

where ϕ is the angle between the diffraction planes and the surface of the crystal, also called the “miscut angle”. For a symmetric reflection $\phi = 0$ and therefore $b = -1$

For XSW structural analysis we will only consider the dipole approximation. The total fluorescence yield Y from the adatoms can be written as [53]

$$Y = Y_{\text{OB}}[1 + R + 2\sqrt{R} \int_{V_c} \rho(\mathbf{r}) \cos(v - 2\pi \mathbf{H} \cdot \mathbf{r}) d\mathbf{r}] \quad (10)$$

where $\rho(\mathbf{r})$ is the normalized spatial distribution function for the fluorescent species and \mathbf{r} is the projected position of the adatoms into the bulk unit cell as shown in figure 5 and $\int_{V_c} \rho d\mathbf{r} = 1$. The H th Fourier component of $\rho(\mathbf{r})$ can be written as

$$\mathcal{F}_{\mathcal{H}}\{\rho(\mathbf{r})\} = \int_{V_c} \rho(\mathbf{r}) e^{2\pi i \mathbf{H} \cdot \mathbf{r}} d\mathbf{r} = f_H e^{2\pi i P_H} \quad (11)$$

equation 10 then can be written as

$$Y = Y_{\text{OB}}[1 + R + 2\sqrt{R} f_H \cos(v - 2\pi P_H)] \quad (12)$$

The two parameters coherent fraction f_H and coherent position P_H from equation 11 are given by $f_H = |\mathcal{F}_{\mathcal{H}}\{\rho(\mathbf{r})\}|$ and $P_H = (2\pi)^{-1} \arg(\mathcal{F}_{\mathcal{H}}\{\rho(\mathbf{r})\})$. Using equation 12 a fit to XSW data can be obtained with just Y_{OB} , f_H and P_H as the fitting parameters. The XSW measurements performed in this thesis work are discussed in chapter 6.

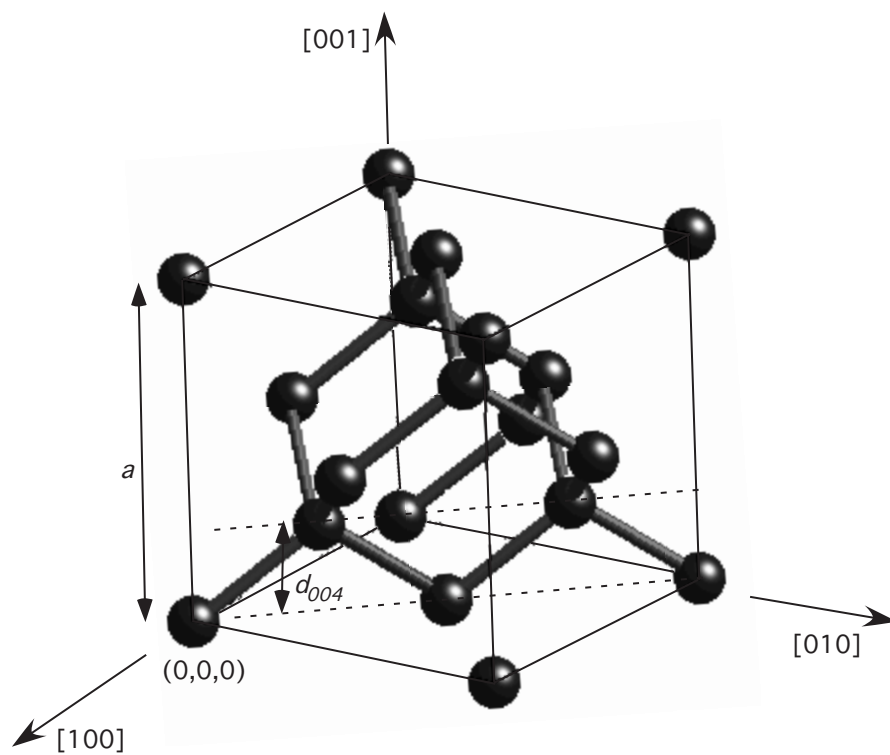


Figure 5: The unit cell for bulk Si. The cubic unit cell has 8 Si atoms. The coherent position P_H are measured with respect to the origin placed at the center of symmetry as shown.

3.2.1 XSW Experimental Setup

The XSW experiments were performed at the 5ID-C undulator beamline of the APS. The schematic of the experimental setup is shown in figure 6. The fundamental spectral peak from the APS undulator source is monochromatized by the liquid-nitrogen cooled Si(111) double crystal monochromator. To filter out photons from higher order harmonics that would normally also be selected the second crystal of the Si(111) monochromator is detuned with respect to the first one. The detuning is on the low angle side of the Si(111) rocking curve by an amount such that the output beam intensity is about 70–80% of its peak intensity. Further energy resolution and angle collimation is achieved by a post-monochromator consisting of two Si(004) channel cut crystals. The beam size is defined by a pair of x-y Huber slits. The sample is held at the center of a four-circle diffractometer. The beam diffracted by the sample is monitored by an in-house built Si avalanche photo-diode (APD) detector. The APD offers high dynamic range in photon counting mode. The fluorescence spectrum from the sample is collected by a liquid-nitrogen cooled Ge solid-state detector. There are four ion-chambers (ICs) to monitor the beam at each stage before the beam hits the sample.

Super fine (sub- μ radians) angular motion for each channel cut is achieved by a piezo driven rotary motion stage with a torsion bearing. Each channel cut was stabilized by using a error integrated feedback from an electronic monochromator stabilizer (MOSTAB) [55]. The MOSTAB continuously monitors the current from the ICs before and after a channel cut and keeps their ratio fixed by adjusting the piezo voltage. Thus the channel cut can be positioned at any point on the Si(004) rocking curve. Using this feature the two channel cuts could be detuned with respect to each other without sacrificing beam stability.

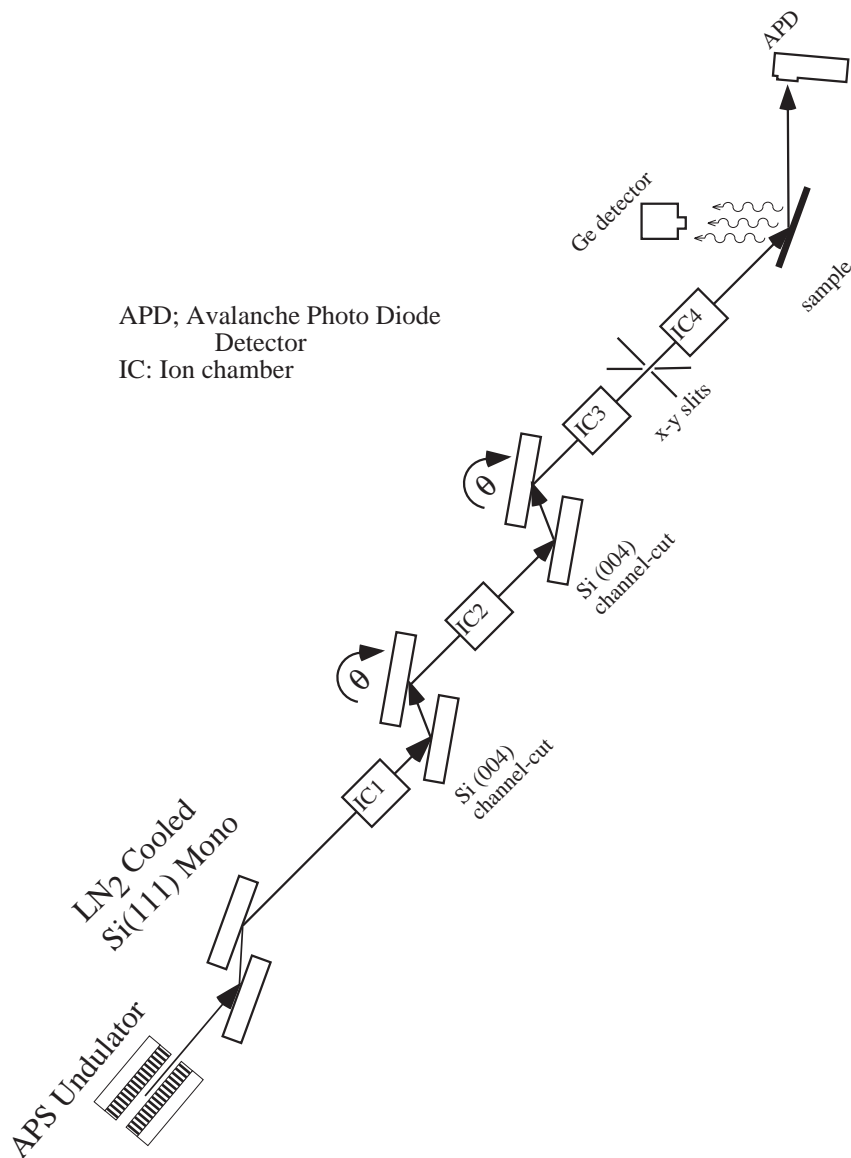


Figure 6: Side-view (except for the Ge fluorescent detector) schematic of the XSW setup at the 5IDC station at APS. The L-N₂ cooled Si(111) monochromator is 30 m from the undulator. The other components starting with ion chamber IC1 sitting on a optical table in the front end of the 5ID-C hutch are approximately 55 m from the undulator.

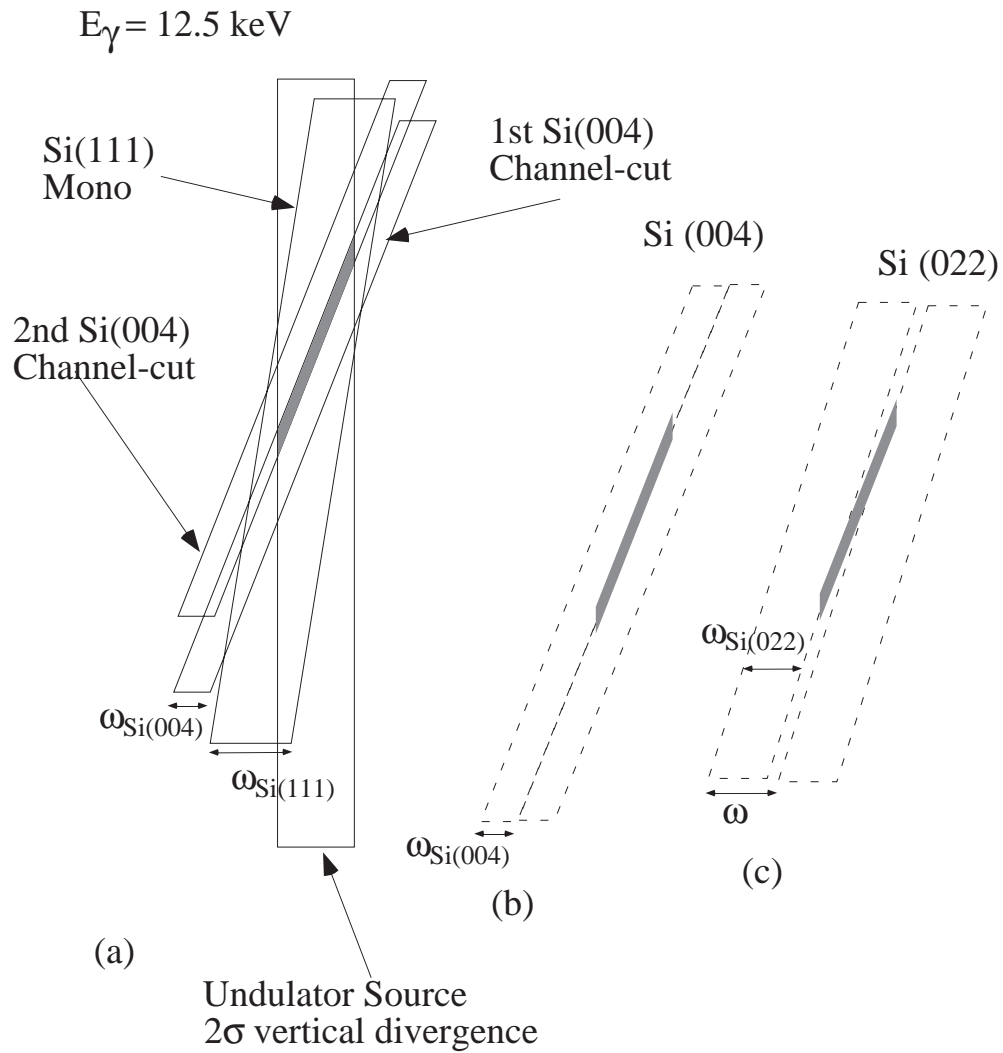


Figure 7: DuMond diagram (a) for the x-ray optics used for XSW measurements, (b) for Si(004) reflection and (c) for Si(022) reflection. X-axis is the incident angle in μrad and Y-axis is the wavelength.

In this thesis XSW measurements were performed for the Si(004), (008) and (022) Bragg reflections. For XSW analysis the angular divergence of the incident beam has to be small compared to the rocking curve width for the sample reflection. The Si(111) rocking curve width is about 2.2 times wider than the Si(004) and 1.4 times wider than the Si(022). Therefore the beam divergence from the Si(111) monochromator was further reduced by detuning the Si(004) channel cuts with respect to each other. This is equivalent to changing the b-factor in equation 8. The DuMond diagram for the x-ray optics at 12.5 keV photon energy is shown in figure 7a. The x-axis is the incident angle in μ radians and the y-axis is the wavelength. The stripes represent the the Bragg reflection condition with the horizontal width equal to the Darwin width. The slope of the stripes is derived from Bragg's law

$$\frac{d\lambda}{d\theta} = 2d_H \cos \theta_B \quad \text{or} \quad \frac{\Delta\lambda}{\lambda} = \cot \theta \Delta\theta \quad (13)$$

In figure 7a the vertical rectangle represents the output from the undulator when its fundamental peak has been tuned to 12.5 keV. This has a very narrow width of $2\sigma = 20 \mu\text{rad}$. Since the widths are extremely narrow the stripes appear as rectangles. The shaded patch at the intersection represents the x-ray beam incident on the sample. As evident in the DuMond diagram, by detuning the two channel cuts the width of the shaded area can be made very small. Figure 7b and 7c depicts the overlap as the sample is scanned for the (004) and (022) reflections respectively. As seen, the measured rocking curve width for the (004) reflection will be almost equal to the theoretical width. For the (022) reflection because of the d-spacing mismatch with the Si(004) channel cut, the rocking curve will be broadened somewhat. The XSW measurements will be discussed in chapter 6.

3.3 GIXD

Due to their very high frequencies, the refractive index at x-ray frequencies is slightly less than unity, $n = 1 - \delta - i\beta$. For all materials $\delta, \beta \ll 1$ but varies from material to material. Therefore from Snell's law [60], x-rays undergo total external reflection at the critical angle $\alpha_c = \sqrt{2\delta} \sim 0.1^\circ$ to 0.5° . In conventional x-ray diffraction the x-rays are incident on the sample surface at some angle α_i that is much larger than the critical angle α_c for total external reflection for x-rays. The penetration depth for x-rays as a function of incident angle is given by [56]

$$Z = \frac{\lambda}{2\sqrt{2}\pi \left(\sqrt{(\alpha^2 - \alpha_c^2)^2 + 4\beta^2} + \alpha_c^2 - \alpha_i^2 \right)^{1/2}} \quad (14)$$

From the time reversibility theorem the depth Z_s from which x-rays will escape out of the sample at an exit angle α_f is the same as given by equation 14 but with α_i replaced by α_f . It can be shown that the effective depth or the scattering depth (Λ) is:

$$\frac{1}{\Lambda} = \frac{1}{Z} + \frac{1}{Z_s} \quad (15)$$

In this thesis we will only consider the special case when $\alpha_i = \alpha_f$, then $\Lambda = Z/2$. For $\alpha_i \gg \alpha_c$, $\Lambda \sim \sin \alpha / (2\mu)$ is very deep. Therefore in conventional diffraction experiments there is a very large contribution from the bulk. For $\alpha_i \ll \alpha_c$, Λ is very shallow, typically about 20–30Å. Λ increases dramatically above the critical angle. This phenomena can be explained qualitatively by total external reflection of x-rays. Below the critical angle x-rays are completely reflected, and there is only an evanescent wave, which decays exponentially, and therefore the scattering depth is shallow. Above the critical angle the x-rays are transmitted, and therefore

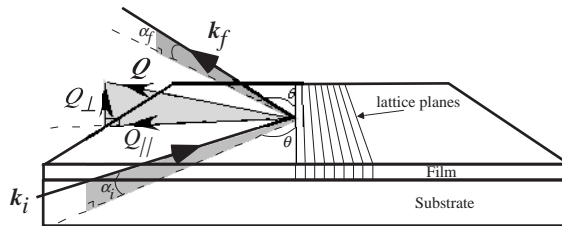


Figure 8: Schematic diagram for GIXD. In our GIXD experiments $\alpha_i = \alpha_f$.

the scattering depth increases dramatically.

The x-ray scattering from an ultra-thin film of a few atomic layers is very weak compared to the substrate below it. Therefore it is very difficult to get structural information about these films with conventional diffraction. At grazing incidence, x-ray scattering from the bulk can be decreased by keeping the incident wavevector \mathbf{k}_i at a very glancing angle. The momentum transfer vector $\mathbf{Q} = \mathbf{k}_f - \mathbf{k}_i$ is split into two components Q_{\parallel} and $Q_{\perp} = k(\sin \alpha_i + \sin \alpha_f)$; $k = 2\pi/\lambda$. For small α_i and α_f , $Q_{\parallel} \sim Q$ and the scattering is almost parallel to the surface. If the sample is now rotated about its surface normal then at some point the Bragg condition for some lattice planes perpendicular to the surface will be met and a diffracted beam will emerge out as shown in figure 8. This is called grazing incidence x-ray diffraction (GIXD). Since even an ultra-thin epitaxial film will have large number ($\sim 10^8$) lattice planes that are perpendicular to the surface the diffraction spots can be very narrow and intense. Therefore the long-range periodicity parallel to the surface can be probed by GIXD [57]. By increasing α_i and α_f the scattering depth can be increased and therefore the in-plane structure of buried layers can also be probed.

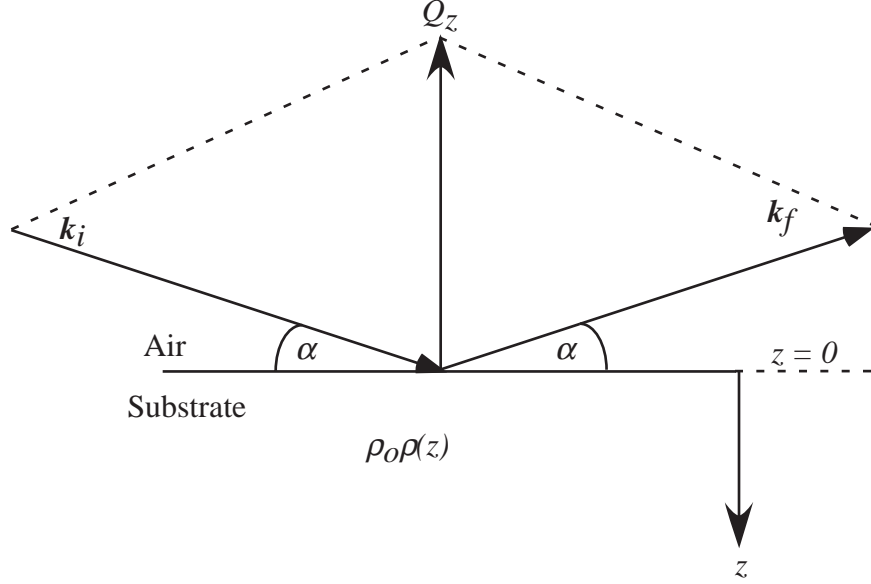


Figure 9: Schematic diagram for x-ray specular reflectivity. $\alpha > \alpha_c$.

3.4 X-ray Specular Reflectivity

X-ray specular reflectivity is a powerful technique for studying film thickness and interfacial and surface roughness of ultra-thin layered structures. This technique is just sensitive to the electron density profile in the surface normal direction and therefore can be used for studying epitaxial as well as amorphous films.

Consider an interface between air and a material of average electron density ρ_0 as shown in figure 9. Let the surface be at $z = 0$ and $\rho(z)$ be the normalized electron density profile. The electron density at distance z below the surface is then $\rho_0 \rho(z)$. For specular reflectivity $Q_{\parallel} = 0$ and $|\mathbf{Q}| = Q_{\perp} = Q_z = 4\pi \sin \alpha / \lambda$. In the kinematic approximation the x-ray reflectivity then is given by [59]

$$R(Q_z) = \left(\frac{4\pi r_e \rho_0}{Q_z^2} \right)^2 \left| \int_{-\infty}^{\infty} \frac{d}{dz} \langle \rho(z) \rangle e^{-iQ_z z} dz \right|^2 \quad (16)$$

where $\langle \rho(z) \rangle$ is averaged in the x - y plane parallel to the interface at z .

For an ideally sharp interface the Fresnel reflectivity is given by [60]

$$R_F(Q_z) = \left| \frac{\sin \alpha - \sqrt{n^2 - \cos^2 \alpha}}{\sin \alpha + \sqrt{n^2 - \cos^2 \alpha}} \right|^2 \quad (17)$$

where $n = 1 - \delta = \sqrt{1 - \rho_0 r_e \lambda^2 / 2\pi} = \sqrt{1 - \alpha_c}$ and we have neglected absorption. For x-ray reflectivity usually α is very small and therefore equation 17 can be written as

$$R_F(Q_z) = \left| \frac{\alpha - \sqrt{\alpha^2 - \alpha_c^2}}{\alpha + \sqrt{\alpha^2 - \alpha_c^2}} \right|^2 \quad (18)$$

for $\alpha \gg \alpha_c$ then

$$R_F(Q_z) = \left(\frac{\alpha_c}{2\alpha} \right)^4 = \left(\frac{4\pi r_e \rho_0}{Q_z^2} \right)^2 \quad \text{for } \alpha \gg \alpha_c \quad (19)$$

Then from equations 16 and 19 we get

$$\frac{R(Q_z)}{R_F(Q_z)} = \left| \int_{-\infty}^z \frac{d}{dz} \langle \rho(z) \rangle e^{-iQ_z z} dz \right|^2 \quad (20)$$

This equation can be used to calculate x-ray reflectivity for any arbitrary electron density profile. Note that because we measure intensity in an experiment phase information is lost and therefore information obtained is model dependent. I will discuss GIXD and x-ray reflectivity measurements in chapter 5.

3.4.1 Experimental Setup for GIXD and x-ray reflectivity measurements

The GIXD and X-ray reflectivity measurements were performed using a 6-circle diffractometer at the 5ID-C undulator and a 4-circle diffractometer at the 2BM-B bending magnet beamlines of the APS. The setup is shown in figure 10.

The x-ray beam after the liquid-nitrogen cooled monochromator is reflected off of a Au coated mirror to filter out higher order harmonic photons from the beam. The scattering plane is in the vertical direction. To reduce background x-ray intensity the entire beam path is either under high vacuum or in a He atmosphere. The sample to detector slits distance was typically 1 m and the slits were vertically about 1 mm to give an angular resolution of about 1 mrad. Due to the grazing incidence the vertical entrance slit size was kept not more than 0.1 mm for GIXD and less than 1 mm for reflectivity measurements.

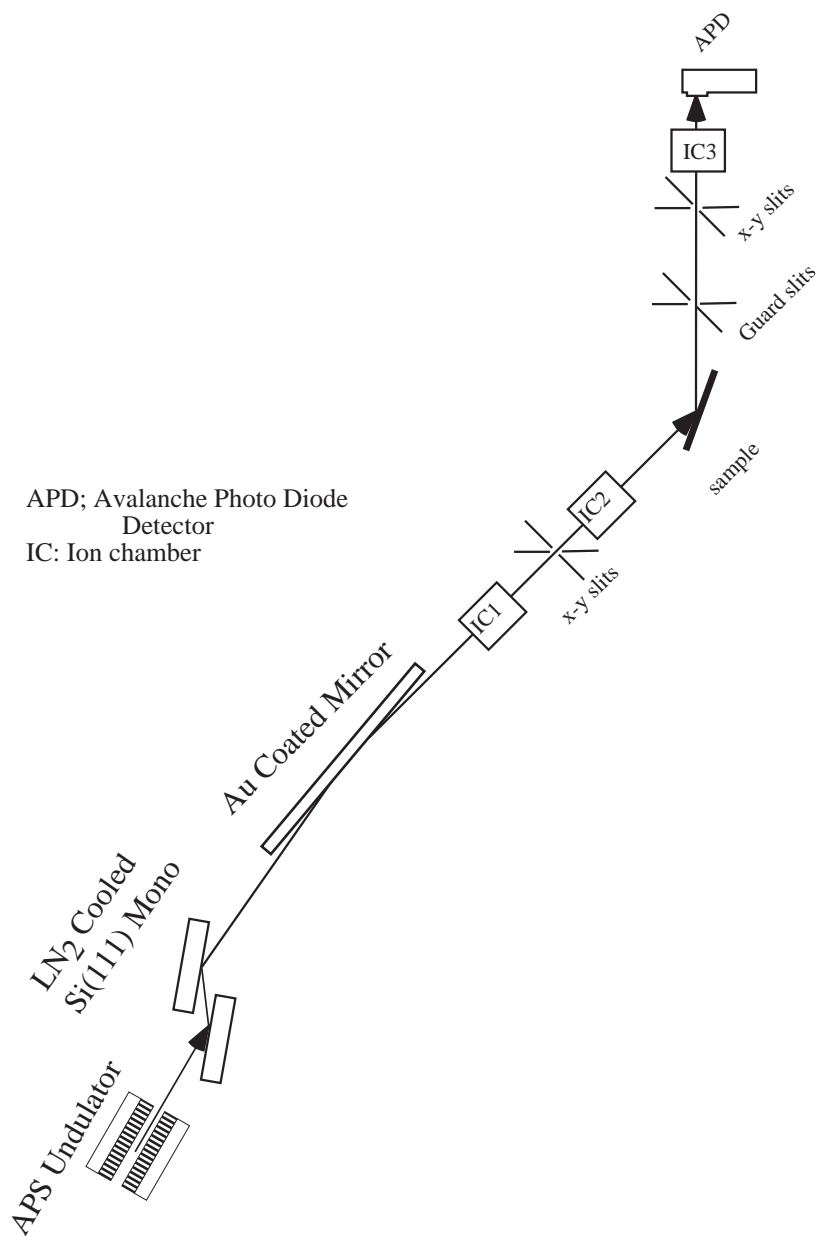


Figure 10: Schematic of experimental setup for GIXD and x-ray reflectivity at APS.

Chapter 4

Sample Preparation and Standard Characterization

All substrates used in this thesis were Si with an (001) surface orientation with less than 0.2° miscut with the surface. For the x-ray scattering experiments the substrates were cut and polished in-house. For the AFM studies of Ge-nanodots n-type Si(001) wafers (P as dopant) with resistivity of $0.04 \Omega\text{-cm}$, were bought from Virginia Semiconductor Inc.

4.1 Preparation of Si Substrates for X-ray Experiments

Substrates were cut from a single boule grown by vacuum float-zone method and had a very low dopant concentration. The substrates were $10 \times 10 \text{ mm}^2$ in size and 3 mm in thickness. The substrates had wings about 1 mm thick for mounting them in an way that would not strain the growth surface. After diamond saw cutting the substrates were etched in CP4 solution (see appendix A) for 30s each time to remove the Si that was damaged during the cutting process. After each etch process x-ray rocking curve measurements were done on a high resolution x-ray

diffractometer to determine the perfect single crystal quality of the substrates. For selected substrates the measured x-ray rocking curve was close to the ideal Darwin width. The substrates were then Syton[®] polished to obtain a near atomically flat single-crystal surface. The perfect single crystal quality of the substrates was verified for a final time by x-ray rocking curve measurements. The substrates were then degreased as follows:

- 10 min. in boiling trichloroethylene
- 10 min. ultrasonic cleaning in acetone
- 10 min. ultrasonic cleaning in methanol
- Rinsed thoroughly in deionised water

The degreased substrates were then Shiraki etched [61] (see appendix A) to grow a layer of native oxide about 10–20 Å in thickness. The native oxide protects the underlying Si for atmospheric contaminants. The native oxide can be easily removed by annealing the substrate under UHV conditions to obtain a clean Si(001) surface.

4.2 Preparation of Lithographically Patterned Si Surfaces

Samples were prepared to study the growth of Ge on Si stripe-mesas. The widths of the stripe-mesas that we were interested in were in the sub-micron range. To make these sub-micron features we opted to use e-beam lithography. Although current photolithography can achieve sub-micron resolution, the equipment is very

expensive and we lacked access to such equipment. In terms of throughput e-beam writing is much slower than photolithography. For example, to expose a $180\mu\text{m} \times 180\mu\text{m}$ area with $0.1\mu\text{m}$ resolution it would take us about 12 hours by e-beam compared to less than a minute for photolithography. In the following sections we will describe the entire patterning process.

4.2.1 Photolithography

The use of e-beam lithography requires an electron beam to be focussed on a charge sensitive layer of material, in our case poly-methyl-methacrylate (PMMA). The focusing of the electron beam is almost always done visually by monitoring the rastered image of the signal from a secondary electron detector (SED). The contrast in the SED signal arises because the number of secondary electrons generated depends on the atomic number. A planar surface coated with PMMA offers no such Z contrast. In addition, one has to somehow prevent accumulation of electron charge on the non-conductive PMMA. Focusing an electron beam on a planar surface with PMMA is thus a challenge.

To overcome or at least minimize these problems, predeposition of metal pads is necessary. We deposited Au pads to focus the electron beam. The Au pads were made by photolithography. The photolithography process was as follows:

- Thoroughly degrease the Si wafer as described in the previous section
- Spin coat the Si wafer with Shipley 1813 positive photoresist at 4000 RPM for 45 s
- Bake in a convection oven at 90°C for 30 min.

- Soak in chlorobenzene for 10–12 min to desensitize the top region of the photoresist
- Blow dry with dry N₂ and bake for 2–3 min at 90°C to remove chlorobenzene
- Expose with UV light for 10–12 s
- Develop in Shipley developer for 45s
- Blow dry and then bake for 5–10 min to completely dry the sample
- Deposit 500–600 Å thick Au from an e–beam evaporator
- Lift–off in acetone.

Chlorobenzene desensitizes the top region of the photoresist layer and therefore the development is slower. This results in an inverted–V profile for the photoresist after development. When Au is deposited it is disconnected from the open and photoresist covered regions on the Si wafer. The Au layer on the photoresist lifts–off when the photoresist is dissolved in acetone leaving behind Au pads with sharp edges.

4.2.2 E–beam Lithography

The Si wafer with Au pads is then coated with PMMA and electron beam lithography is performed. The following are the main steps involved in e–beam lithography:

- Spin coat Si wafer with 100K PMMA at 2000 RPM for 45s
- Bake at 170°C for 1 hr
- Spin coat 500K PMMA at 5000 RPM for 45s

- Bake at 170°C for 1 hr
- Perform e-beam exposure
- Develop in 1 : 3 solution of methyl-isobutyl-ketone and isopropyl-alcohol for 45 s
- Blow dry with dry N₂ and then bake 5–10 mins to completely dry the wafer
- Deposit 500–600 Å Al as etch-stop material
- Lift-off in acetone.

The thickness of the each PMMA layer is about 200 nm. A bilayer of PMMA is used for the purpose of achieving clean lift-off. The top 500K PMMA is less sensitive than the bottom 100K PMMA layer. The Al layer is therefore not continuous and as in photolithography it lifts-off giving sharp features.

The e-beam exposure was done using a Cambridge StereoScan Scanning Electron Microscope (SEM) that was modified to achieve e-beam writing. An external computer reads an AUTOCAD drawing of a mask and accordingly controls the exposure of the e-beam. The dosage D of the beam is determined by three factors: the beam current i , the size of a single pixel x , and the dwell time t . The beam current is set by the emission current and the settings of the condensers. The computer digitizes any pattern to be exposed into a definite number of pixels. The above three parameters have to be optimized to obtain maximum resolution and minimum exposure time. A significant fraction of the total exposure is from backscattered electrons. For larger patterns where poor resolution is tolerable the beam current and the pixel size can be increased. The dwell time can be adjusted to get correct exposure. For very fine patterns the pixel size has to be very small,

but to minimize backscattering the dwell time and the beam current should be as small as possible. The exposure resolution is given by

$$x = \sqrt{\frac{it}{D}} \quad (21)$$

All the exposures were carried out at 20 keV accelerating voltage. Typical dosage for Si was $370 \mu\text{C}/\text{cm}^2$ for sub-micron features at 5–10 pA beam current.

4.2.3 Etching

The Si wafer with sub-micron wide Al lines obtained by the combination of e-beam lithography and deposition is then etched by reactive ion etching (RIE) using CF_4 . RIE is a dry form of etching and can be well controlled. The atomic F present in the CF_4 plasma generated by a RF power supply, reacts with Si to form volatile products which are immediately removed from the system by continuous pumping. The etching of Si thus continues steadily. On the other hand fluorine forms an extremely stable compound with Al which prevents its etching. The Al lines and the Si underneath them is thus protected. Si etching in CF_4 plasma is isotropic so significant under cutting of the Si is observed. The RIE etching was performed as follows.

The RIE chamber is first pumped down to less than 1 mtorr pressure. CF_4 gas is then purged several times to remove impurity gases especially water vapor which can effect the etching characteristics. Since the CF_4 gas is constantly consumed during the etching process, its flow rate and pressure are important process parameters. The following step ensured consistency from run to run. The main valve of the turbo pump is kept open and the CF_4 gas pressure is maintained at 20 mtorr. The valve is then throttled until the pressure increases to 50 mtorr. Under

these conditions the Si etch rate is about 10 Å/sec at 50 watts. The etching is carried for 1 min. The Al is then removed by dipping the Si wafer in concentrated HNO₃ for 10 min.

4.3 UHV Chamber and MBE Growth

All the Si/Ge/Si(001) and Ge/Si(001) samples were grown by Molecular Beam Epitaxy (MBE) in our MBE chamber at Northwestern University (NU).

4.3.1 MBE Surface Science Chamber

The MBE surface science chamber is an in-house-built ultra high vacuum chamber in our lab at NU. It was designed to provide surface preparation, surface analysis and MBE growth capability in a single compact chamber. The chamber has the capability to achieve UHV with better than 1×10^{-10} torr base pressure. The chamber is equipped with an oil-free turbo pump, an ion-pump, and a titanium sublimation pump (TSP). Standard vacuum practices were employed to achieve the aforementioned pressure conditions. The partial pressures for residual gases under UHV conditions are plotted in figure 11. The schematic of the chamber is shown in figure 12. The chamber has dedicated as well as many standard ports for any future additions. The dedicated ports are for the sample introduction, sample manipulator, LEED, cylindrical mirror analyzer (CMA) for Auger spectroscopy, MBE and the STM junction.

The superior vacuum in the chamber is preserved during sample introduction by the use of a load-locked chamber which is isolated from the main chamber by a gate valve. With the Si substrate inside, the load-locked chamber is pumped from atmospheric pressure down to 10^{-7} torr in 30 min. The isolation valve between the

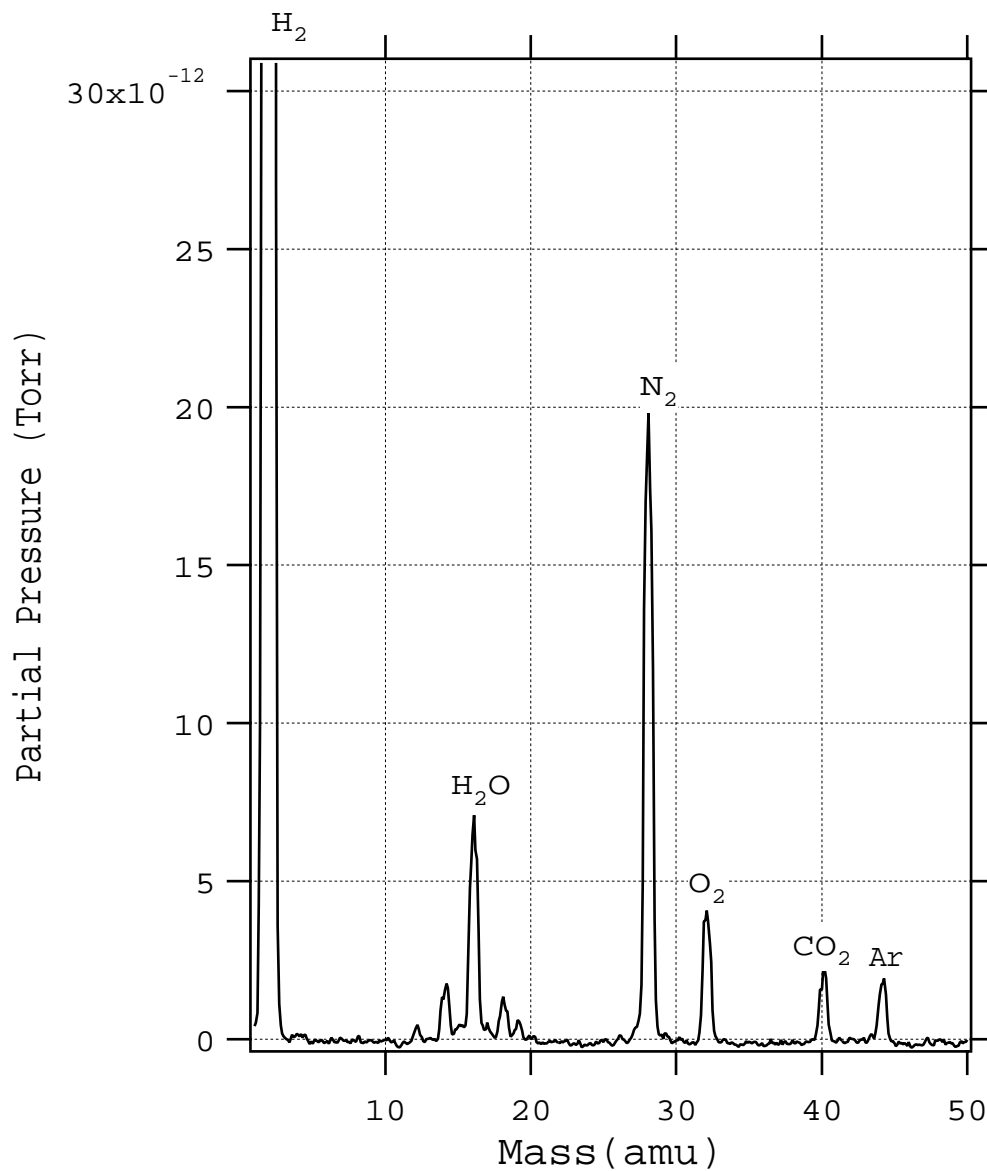


Figure 11: Partial pressures for residual gases inside the chamber under UHV conditions. The H_2 partial pressure is 2×10^{-10} torr.

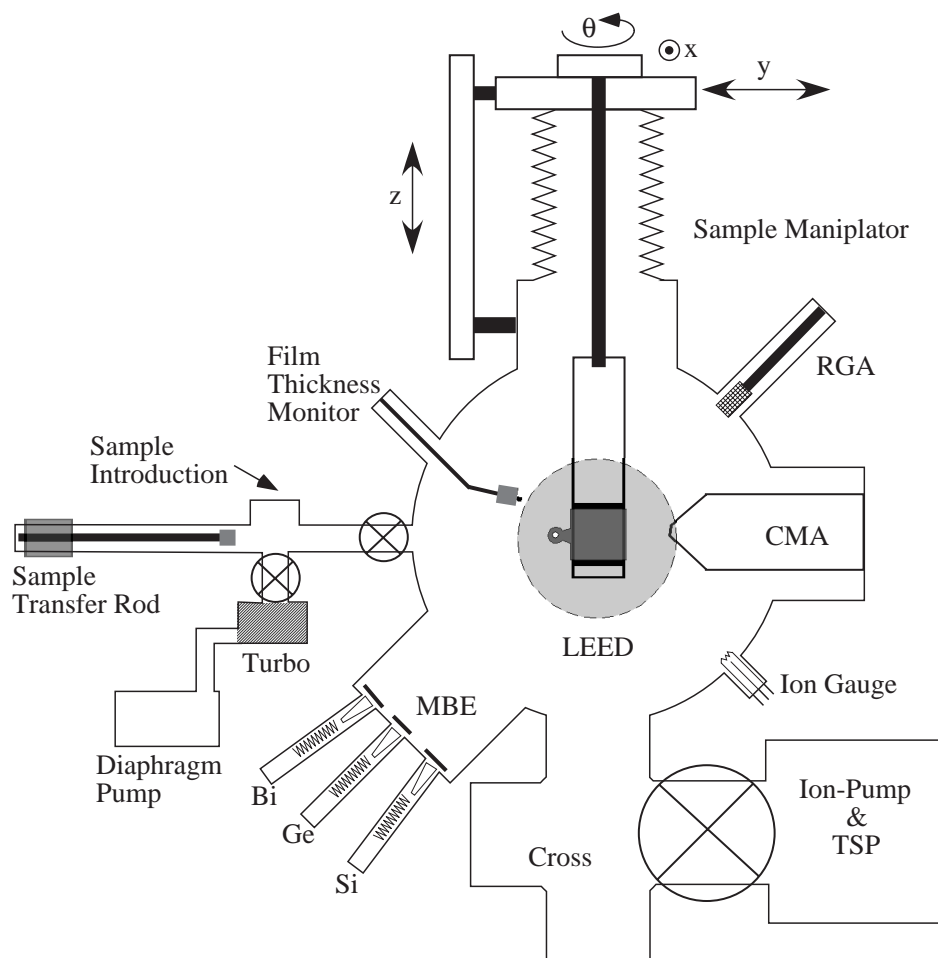


Figure 12: Schematic side-view of the MBE chamber. All the essential ports are shown. The LEED port is out of the plane of the paper while the STM port is diametrically opposite to the LEED.

main chamber and the load-locked chamber is opened and the sample is quickly transferred into the chamber. During this brief time the chamber pressure rises only to about 10^{-9} torr. The chamber vacuum quickly recovers as soon as the isolation valve is closed. The use of a load-locked chamber thus ensures quick transfer without having to break UHV condition, which is a long and tedious process to recover from.

Inside the chamber the sample is held vertically by the manipulator. The manipulator has four degrees of freedom: horizontal x-y, vertical z and angular in the horizontal plane. An isometric view of the manipulator head is shown in figure 13. The manipulator head also has a tungsten filament heater positioned behind the sample and a K-type thermocouple above the sample. The sample can be heated from room temperature to 1000°C by radiative heating using the filament heater. The manipulator also has the capability of heating the sample by passing current through the sample. The latter is ideal for semiconductor samples like Si because the heating is localized and therefore higher temperatures can be reached without significant outgassing from surrounding surfaces. The high resistivity of the XSW samples prevented the use of direct current heating. There can be strong variations in current densities across the sample surface from direct heating which can excessively strain the Si crystal. The indirect filament heating was thus used because it provided a strain free way of heating the Si samples, up to 1000°C .

The LEED and the CMA point radially inward along the horizontal plane of the spherical chamber. The reverse-view LEED from Omicron is equipped with a CCD camera to capture diffraction images. The PHI single-pass CMA has a concentric electron gun and electron detection system. The working distance for the CMA is about 18 mm. The LEED image capturing and the AES data collection are both computer controlled (see appendix B).

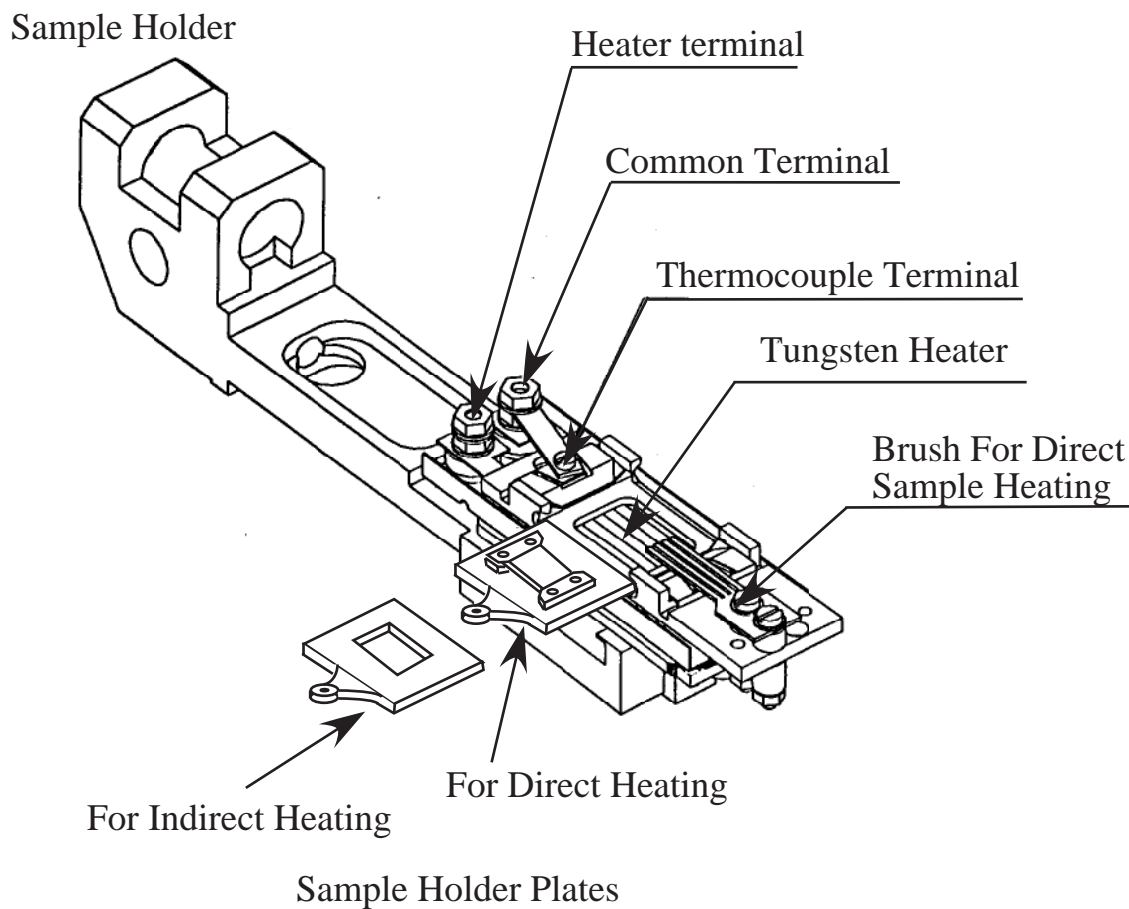


Figure 13: An isometric view of the manipulator head. The manipulator is machined out of Mo. The two sample holder plates for direct and indirect sample heating are also shown.

4.3.2 MBE growth

The samples were prepared by molecular beam epitaxy (MBE) in an ultra high vacuum (UHV) chamber with a base pressure of better than 1×10^{-10} torr. The samples were degreased and Shiraki etched before being introduced into the chamber. Samples were then out-gassed for at least 12-hrs at 650°C and then flash annealed at 950°C to achieve a clean Si(001) surface, which was verified by a sharp 2-domain 2×1 LEED pattern. No oxygen or carbon contamination of the surface was observed by Auger electron spectroscopy (AES). Samples were prepared with and without Bi as a surfactant with Ge coverages ranging from 1–10 ML. Throughout the growth, the temperature of the sample was held at 400°C . Initially about a ML of Bi was deposited from a Knudsen cell held at 550°C and then Ge deposition was carried out at a rate of 0.06 ML/min by evaporation from a Knudsen cell held at 1200°C . During the Ge growth a constant overpressure of Bi was maintained to compensate for the desorption of Bi. After Ge deposition was complete Si deposition was carried out at a rate of about 1 ML/min from an e-beam evaporator. Typical e-beam evaporator power was 105 watts. The Bi flux was turned off after 20 ML deposition of Si. The nominal thickness of the deposited Si was typically 100 Å. The absolute Ge coverage of each sample was measured by Ge $K\alpha$ fluorescence comparison with a standard sample that was calibrated by Rutherford back-scattering. At each stage of the film deposition the surface was studied by LEED and AES at room temperature.

For the Ge growth on the patterned Si(001) surfaces, the substrates were 0.5 mm thick wafers. The growth methods were the same as above expect for the following: The sample heating was achieved by passing a current through the samples as it was more convenient and did not affect AFM studies. The Ge islands

were grown at a substrate temperature of 640°C. No surfactant was used and to preserve the morphology of the Ge islands no Si cap was deposited after Ge deposition.

4.4 *In situ* LEED and AES Studies

The mean-free path for electrons in solids for kinetic energies in the range of 10 to 2000 eV is only about 4–20 Å [62]. At these energies electrons are very suitable for studying surfaces. LEED can reveal the structure of periodic surfaces while AES can be used to study the elemental composition on the surface.

4.4.1 Clean Si(001) surface

For a bulk like terminated Si(001) surface the topmost Si layer has two dangling bonds per surface Si atom. This is a highly energetic surface which lowers its energy by surface reconstruction. Two adjacent Si atoms in the same layer form a dimer leaving just one dangling bond per surface atom. The surface period is doubled along the direction of the dimer. As shown in figure 14a every time there is a step on the surface the direction of the dimer is rotated by 90°. As both domains are equally populated the LEED pattern of a clean Si(001) surface appears as shown in figure 14b. This is the LEED pattern we observed after cleaning the Si substrates in our chamber. The diffraction pattern is therefore a superposition of a 2×1 and 1×2 patterns that are rotated with respect to each other by 90°.

Figure 15 shows the Auger spectrum of a clean Si(001) surface. The derivative of the AES intensity is plotted as a function of electron energy. Only a Si LMM-peak at 92 eV is observed. Note that the sensitivity after 130 eV is 10 times higher. No O KLL-peak or C KLL-peak are observed indicating a clean surface.

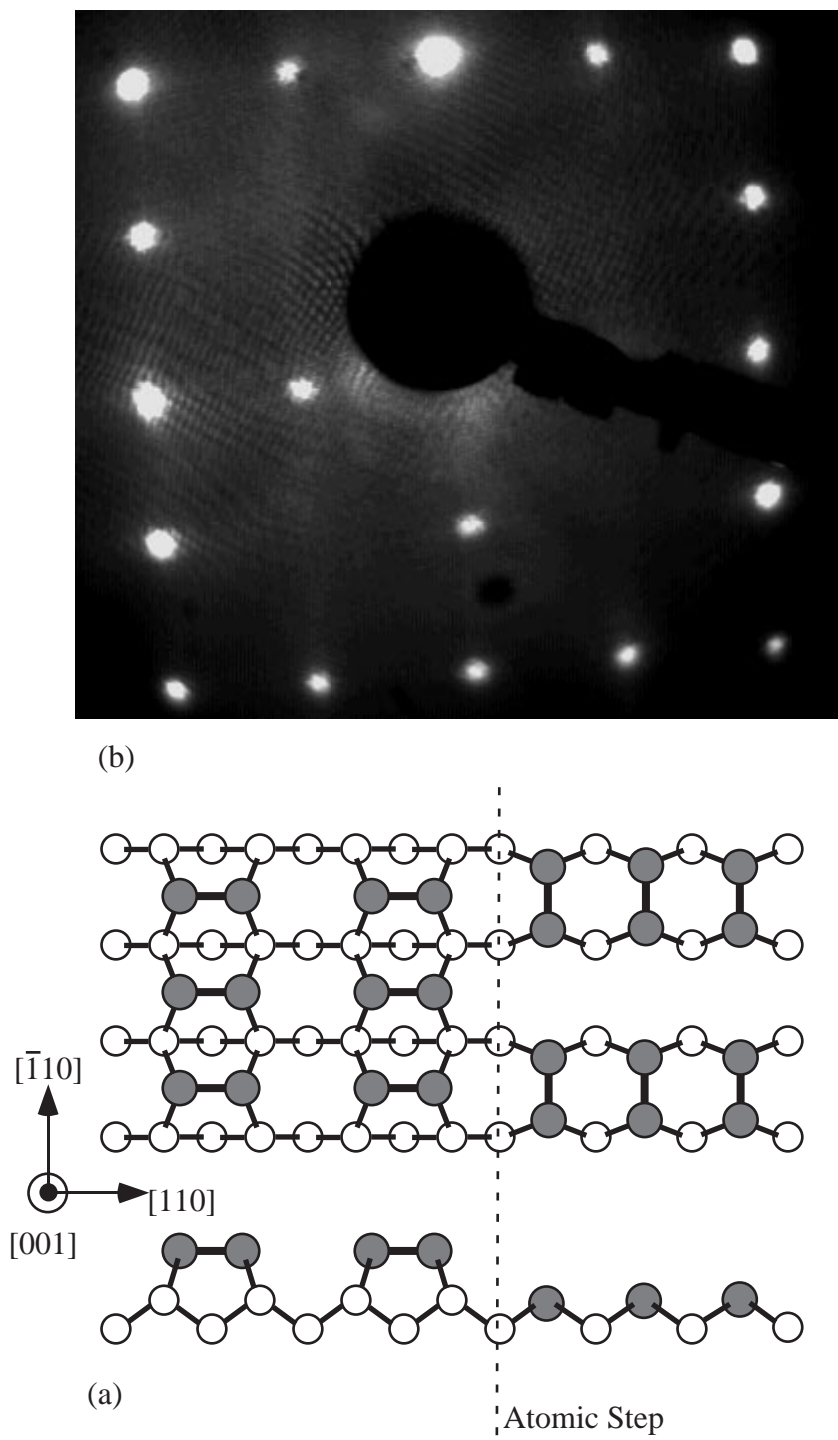


Figure 14: 2-domain 2×1 LEED pattern of clean Si(001) surface.

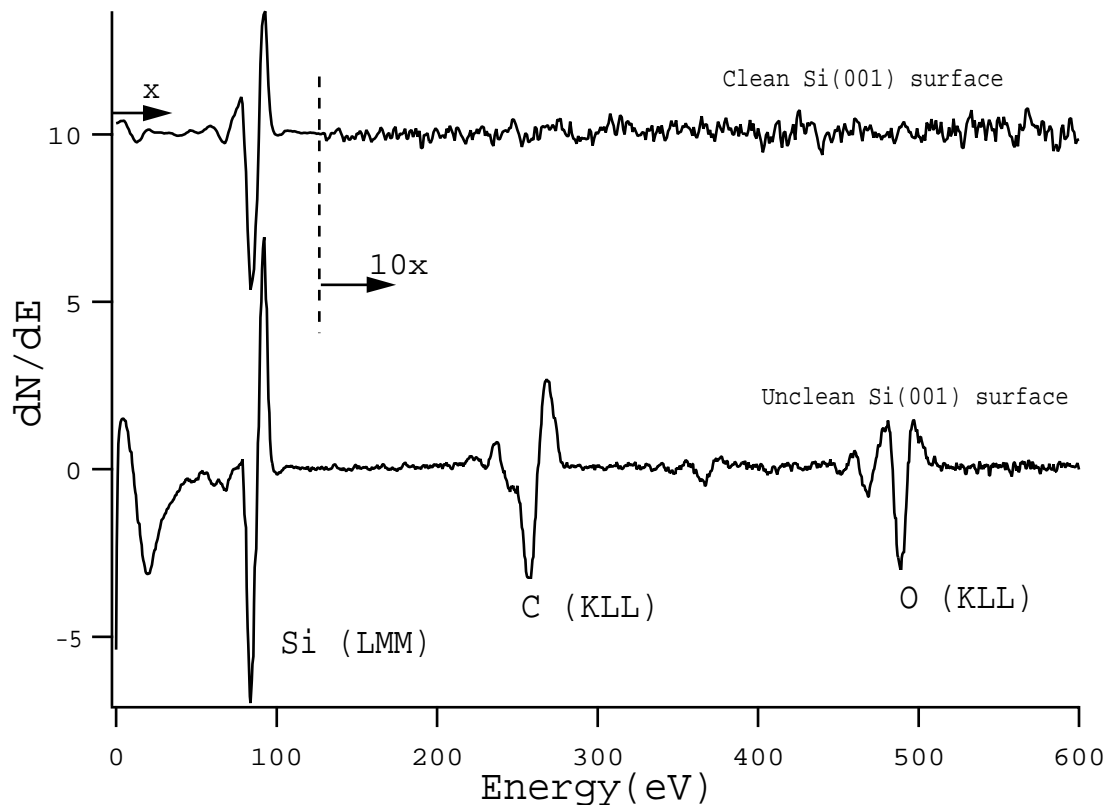


Figure 15: Auger spectrums for clean and unclean Si(001) surfaces. Note that for clean surface the sensitivity was increased by a factor of 10 for $E > 130$ eV.

For comparison an Auger spectrum performed on a Si surface just after being introduced into the chamber is also shown. A strong O peak from the oxide and a C peak are seen.

4.4.2 Bi terminated Si(001) surface

Interest in the Bi terminated Si(001) surface grew after it was used as a surfactant for the epitaxial growth of Ge/Si(001) [40] and two distinct local structures 1×2 and 2×2 for Bi/Si(001) were reported [49]. LEED, AES, and RHEED experiments [47, 48] show a $2 \times n$ reconstruction with n ranging from 5 to 13

for sub-monolayer Bi/Si(001) surface. Qian *et al* [50] found a thermally activated transition from the metastable 2×2 phase to the stable 1×2 phase by x-ray standing wave (XSW) measurements. These two structures were predicted by Tang *et al* [51] using first-principles local-density molecular cluster calculations. Due to the extra valence electron in the group VI Bi, the Bi-dimerized surface is very stable, i.e. chemically inert.

The Bi saturation coverage on Si(001) depends on the substrate temperature. We deposited several monolayers of Bi on Si at RT and then measured the relative Bi coverage as a function of temperature. At each temperature the sample was annealed for 2 min. Figure 16 shows the temperature dependence of Bi(NO₂)/Si(LMM) AES. As seen the Bi/Si intensity ratio falls sharply as loosely bound and excess Bi is quickly desorbed when the temperature is raised. After 400°C the Bi/Si intensity decreases linearly with temperature. At 575°C Bi is completely desorbed from the surface.

The LEED pattern observed for Bi/Si(001) depends on Bi coverage and hence on the maximum temperature to which the substrate is exposed after Bi deposition. Figure 17(a) shows 2-domain $2 \times n$ LEED pattern obtained at 400°C which is the growth temperature for our samples. The coverage can be determined as $1 - 1/n$ [47]. From our LEED pattern $n \sim 5$ and therefore the Bi saturation coverage at 400°C was estimated to be about 0.8 ML. As shown in figure 17(b) the n th order peaks result from missing Bi dimers that are formed to relieve the strain due to the large lattice mismatch between Bi and Si.

Even at constant temperature we observed Bi desorption from the sample (n decreasing) and therefore we had to maintain a constant flux of Bi to compensate for the desorption. LEED observations made at several points during the Ge and Si growth showed similar patterns as shown in figure 17 with about 10% variation

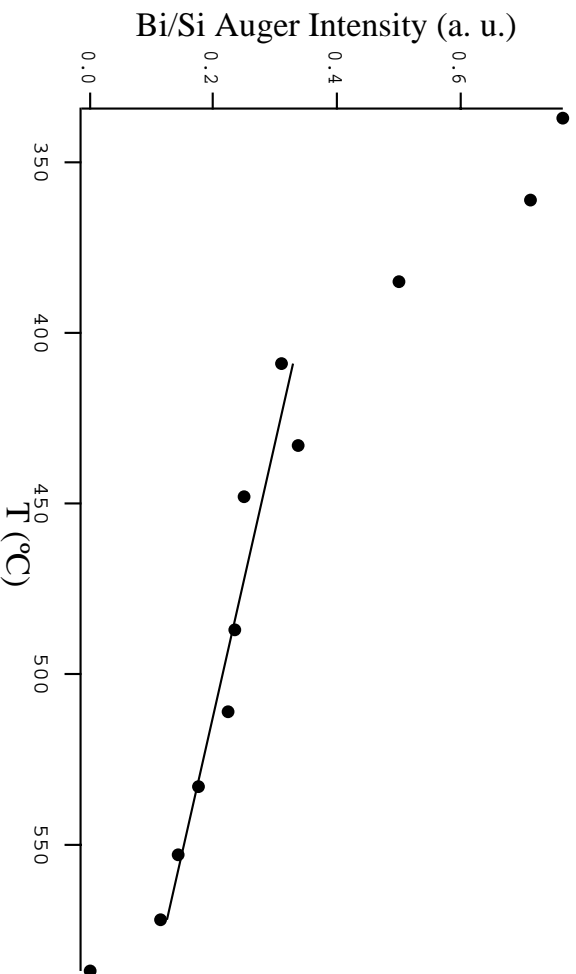


Figure 16: Bi(NOO)/Si(LMM) Auger intensity ratio as a function of substrate temperature. Bi coverage beyond 400°C decreases linearly with temperature.

in Bi coverage. Figure 18 depicts the expected growth mechanism for surfactant mediated epitaxy of Ge on Si with Bi as a surfactant.

4.5 Ge Coverage Calibration

The Ge coverages were measured by Rutherford Back-Scattering (RBS) and x-ray fluorescence. A Si(001) substrate with a shallow ($\sim 300\text{\AA}$) ion implanted layer of Ge which was designated as the standard was accurately calibrated by performing RBS in the Material Science Division at Argonne National Laboratory. The Ge coverage on each sample was then measured by comparing the Ge $K\alpha$ fluorescence yield produced from it to that from the standard. The standard and the samples were identical in size and shape. The incident x-ray energy was set at 12 keV. The incident x-rays, the substrate, and the detector geometry was fixed and was far from any Bragg diffraction condition. The incident x-ray beam was monitored

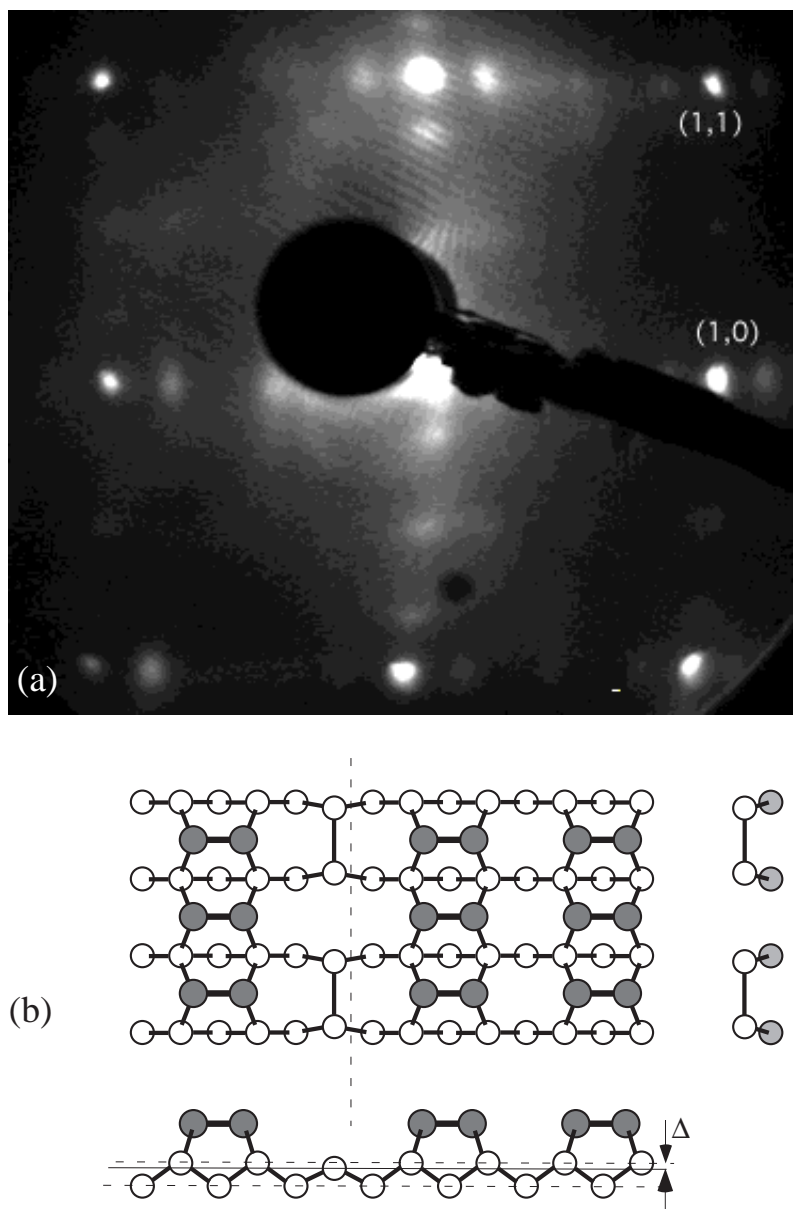


Figure 17: (a) 2-domain $2 \times n$ LEED pattern for Bi terminated Si(001) surface, resulting from missing Bi dimer as shown in (b). Atoms in the second layer form a dimer at that site. With $n \sim 5$, the coverages is estimated to be $1 - 1/n$ about 0.8 ML.

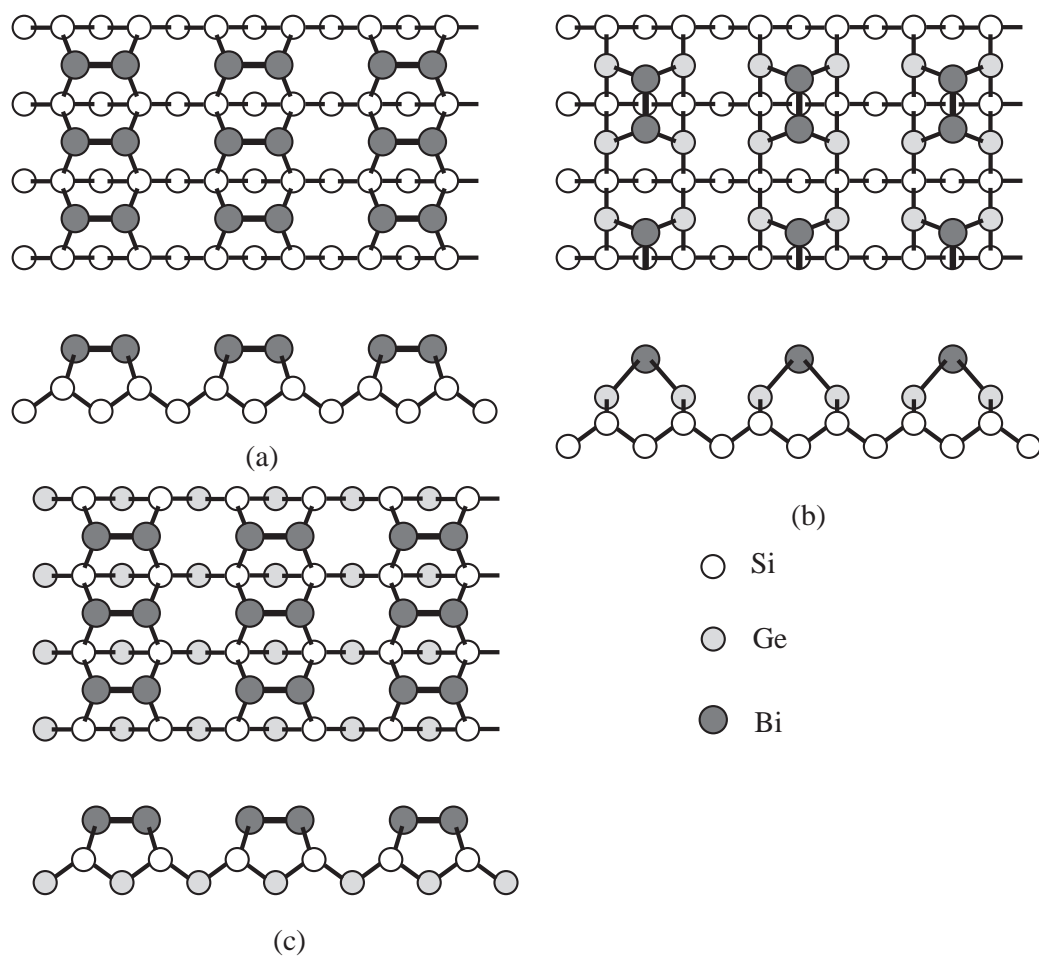


Figure 18: Atomic view of Si/Ge growth on Si(001) with Bi as the surfactant. (a) Bi dimers on Si(001) surface after 1ML Bi coverage. (b) after Ge deposition on Bi covered surface, and (c) after Si deposition following Ge growth. Driven by the surface free energy minimization, Bi segregates to the growth surface and forms a Bi-Bi dimer at each stage.

Sample #	Coverage ± 0.1 ML
003	1.6
004*	1.1
005	3.4
006	3.0
007	7.1
008	4.6
009	10.0
010	1.7

Table 1: Measured coverages of Ge for all the samples. *No Bi was used for this sample.

by an ion-chamber operating in the linear region and with pure He gas flowing through it at a constant rate to ensure a flat temporal response curve. The Ge $K\alpha$ fluorescence counts were collected for 400 s live time for each case. The fluorescence counts normalized to the incident x-ray intensity are shown in figure 19 and the estimated coverages in table 1. The solid line are Gaussian fits to the data. The peak width and position were fixed for all the fits. The coverage Θ was then calculated as follows

$$\Theta = \frac{A}{A_s} \Theta_s \quad (22)$$

Where A and A_s are the area under the peaks for a sample and the standard respectively in figure 19. The Ge coverage Θ_s for the standard measured by RBS was 0.86 ± 0.01 ML ($1 \text{ ML} = 6.67 \times 10^{14} \text{ atoms/cm}^2$). The error in our coverage measurement is less than 0.1 ML. The variation in Ge coverage over each sample area was found to be negligible indicating uniform Ge growth.

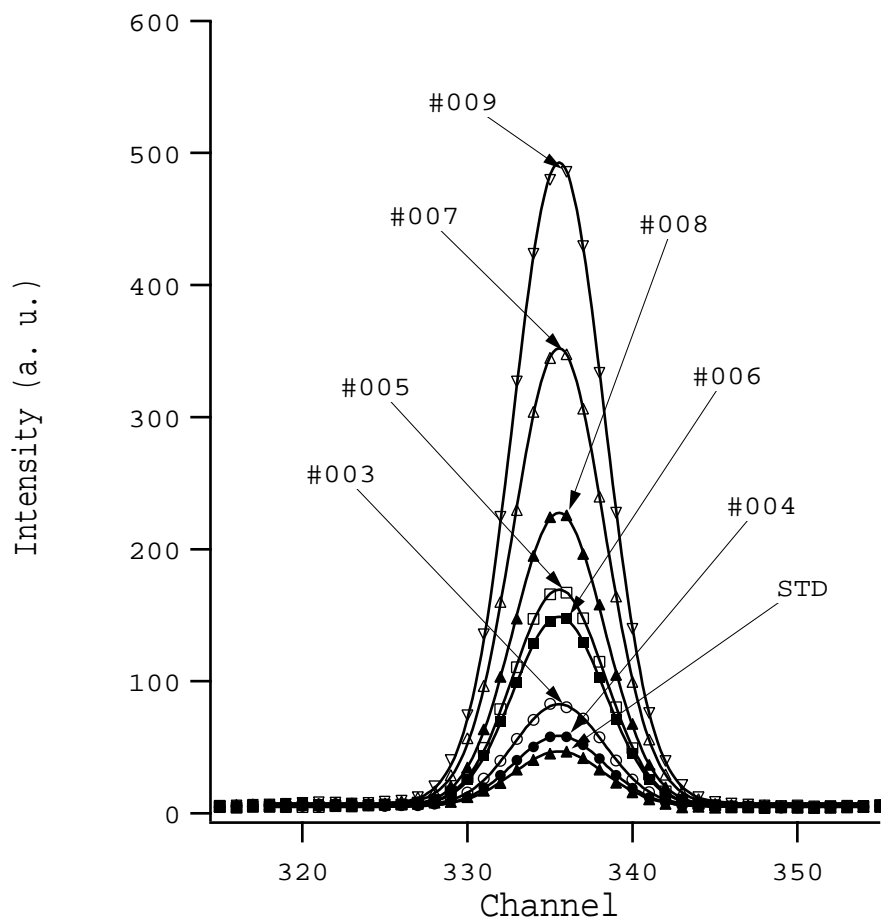


Figure 19: Calibration of Ge coverage by exciting Ge $K\alpha$ fluorescence. Solid lines are Gaussian fits to the data (points). The Ge coverage is proportional to the area under the peak.

Chapter 5

X-ray Scattering Studies

5.1 Introduction

Ge growth on Si(001) is pseudomorphic only up to 3–4 ML [10] after which it forms coherent islands or dislocations depending on the growth temperature [2]. In the pseudomorphic regime the Ge in-plane lattice constant is constrained to match that of the Si substrate. When the islands begin to form or dislocations form the Ge layers are relaxed either partially or completely and therefore their in-plane lattice constant is then larger than the Si substrate. GIXD can probe the in-plane crystallinity and therefore can establish the onset of island formation or dislocations [57].

X-ray reflectivity is sensitive to the electron density profile along the depth and therefore reveals information about the surface and interface roughness and film thickness [59]. We used a combination of GIXD and x-ray reflectivity to study surfactant mediated epitaxy of Ge on Si(001) with Bi as the surfactant.

The critical thickness d_{sk} for Ge growth on Si(001) can be estimated by using equation given by Matthews and Blakeslee [12] for calculating critical thickness for dislocation formation

$$d_{SK} \sim \frac{b}{8\pi(1+\nu)f} \left[\ln\left(\frac{d_{SK}}{b}\right) + 1 \right] \quad (23)$$

where b is the magnitude of Burgers vector of the dislocation (for (100) semiconductor systems $b = a/\sqrt{2}$), $\nu = 0.274$ is the Poisson's ratio, $f = 0.042$ is the lattice mismatch between Ge and Si, and $a = 5.430 \text{ \AA}$ is the lattice constant for Si. Putting these values the critical thickness $d_{SK} \sim 3 \text{ ML}$.

5.2 Previous GIXD Studies

Early *in situ* GIXD experiments by Williams *et al* [17] showed that the critical thickness for strain relaxation is 3–4 ML for Ge growth on Si(001) at 500°C. By precisely controlling the scattering depth for the diffraction they mapped the strain distribution in 10 ML thick Ge films. They found two components in the strain distribution; one which is fully relaxed and other exhibiting a lattice constant intermediate between Ge and Si. By varying the scattering depth they clearly established that the intermediate lattice is that of the wetting layer of Ge and the islands at the top were fully relaxed. Headrick *et al* [65] characterized buried Ge layers in Si(001) with GIXD x-ray reflectivity and Raman scattering. For Ge coverages above 3 ML they found intermixing of Si and Ge at the interfaces.

Thornton *et al* [38] performed *in situ* GIXD studies of Ge grown on Si(001) using Sb as the surfactant. They measured the critical thickness for strain relaxation or pseudomorphic growth to be $\sim 11 \text{ ML}$. In contrast to Ge grown without surfactants they found that the Ge layers remained partially relaxed even at high coverage $\sim 55 \text{ ML}$ and complete relaxation was achieved only after annealing at 700°C. Their x-ray reflectivity measurements showed that the Ge growth in the presence of Sb layer on the surface was 2D and not in SK mode.

5.3 GIXD and Reflectivity Results

The x-ray measurements were performed at the Advanced Photon Source on a six-circle diffractometer at beamline 5ID-C and a 4-circle diffractometer at beamline 2BM-B. A Si(111) monochromator was used to select a x-ray energy at 11 keV. A platinum coated flat mirror was used to filter out the higher harmonic photons from the x-ray beam. The slits on the detector were set to give an angular resolution of 1 mrad.

Figures 21 and 22 show the collected scattered intensities for GIXD radial scans in the [110] direction passing through the (22L) rod (see the inset in figure 21). Each scan was performed at a fixed value of L corresponding to an angle near the critical angle ($\alpha_c = 0.16^\circ$) for total-external x-ray reflection from Si at 11 keV. The exit angle was equal to the incident angle. Under this scattering geometry the x-ray scattering depth (Λ) is approximately half of the x-ray penetration depth [58] and is depicted as a function of L in figure 20. The incident angle α is related to L as $L = 2d\alpha/\lambda$ ($d = 5.431 \text{ \AA}$). For radial scans at $L = 0.01$ the evanescent wave dramatically reduces the scattering depth to $\Lambda = 20 \text{ \AA}$, thus causing the scattered intensity to be originating entirely from the 100 \AA Si cap layer. Above the critical angle, at $L = 0.04$, $\Lambda \sim 3000 \text{ \AA}$ and therefore the scattered intensity has contributions from the substrate, Ge layer and the Si cap layer. This ability of GIXD to probe the in-plane lattice parameter at various depths makes it possible to estimate the strain in both the buried Ge layer and the Si cap layer. Specular x-ray reflectivity measurements (see figure 24) were also performed to estimate the surface and the interface roughness, and the thickness of the Ge and Si cap layers.

The LEED and Auger surface analysis indicates that Bi segregated to the surface at all times during the MBE growth. The surface reconstruction of Bi

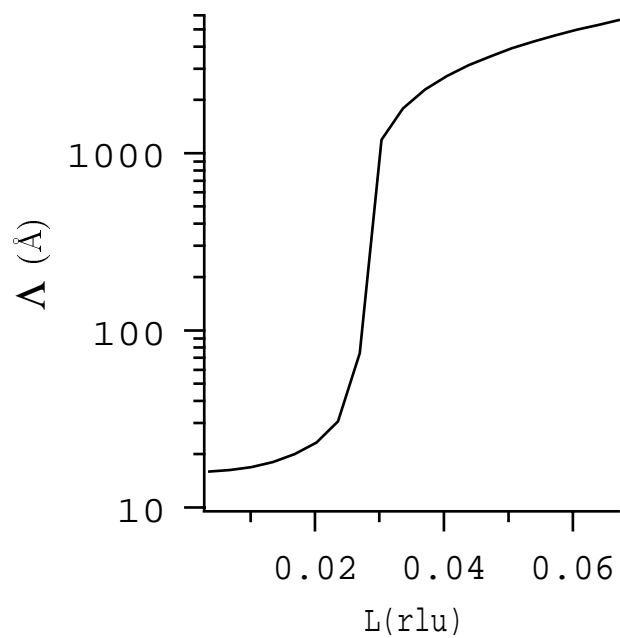


Figure 20: Scattering depth Λ for 11 keV x-rays as function of L. The incident and exit angles are equal.

on Si(001) is coverage dependent. The LEED pattern after Bi deposition on Si at 400°C was 2—domain ($2 \times n$) with n equal to 4 or 5. The saturation coverage is then equal to $(n - 1)/n$ ML [47] which is approximately 0.8 ML based on previous x-ray standing wave measurements [66]. On Bi surfactant samples, the LEED pattern after Ge deposition was $2 \times n$ with n varying between 2 and 5. The decrease in n can be explained by Bi desorption. The LEED observations were similar after the deposition of the Si cap layer, however the spots were more diffuse. Using AES no Ge was detected on the surface after Si deposition. This clearly shows that Bi segregated to the growth surface for both Ge and Si. For normal Ge growth without Bi, the Ge surface reconstruction was 2×1 during 2-D growth. For sample 1 after 10 ML of Ge deposition we observed a LEED pattern that had additional spots consistent with the 3-D growth of Ge pyramid shaped islands with $\{105\}$ facets [18, 19, 63]. After depositing the Si cap layer a diffuse 2×1 LEED pattern was observed and traces of Ge were detected by AES. Part of the Ge thus diffused into the Si layer and segregated to the surface, when Bi was not used as a surfactant.

Figure 21 shows the H, K scans at $L = 0.01$ for the 10 ML Ge samples with (a) and without (b) Bi. The x-ray scattering depth was approximately 35 Å, ensuring that only the top layers in the Si cap layer were probed. For the 10 ML sample with Bi there was only one peak at the $(2 \ 2 \ L)$ Si bulk position indicating that the Si layer was of very high crystallinity. For the 10 ML sample without Bi there were two additional peaks one at H, K = 1.92 that corresponds to a relaxed Ge layer and another at H, K = 1.98 from a Si-Ge alloy. Figure 22 shows the H, K scans for all four samples at $L = 0.04$, where the x-rays penetrated ~ 3000 Å. Therefore all the layers were probed with contribution to the scattered x-ray intensity decreasing with depth due to absorption. For 10 ML without Bi,

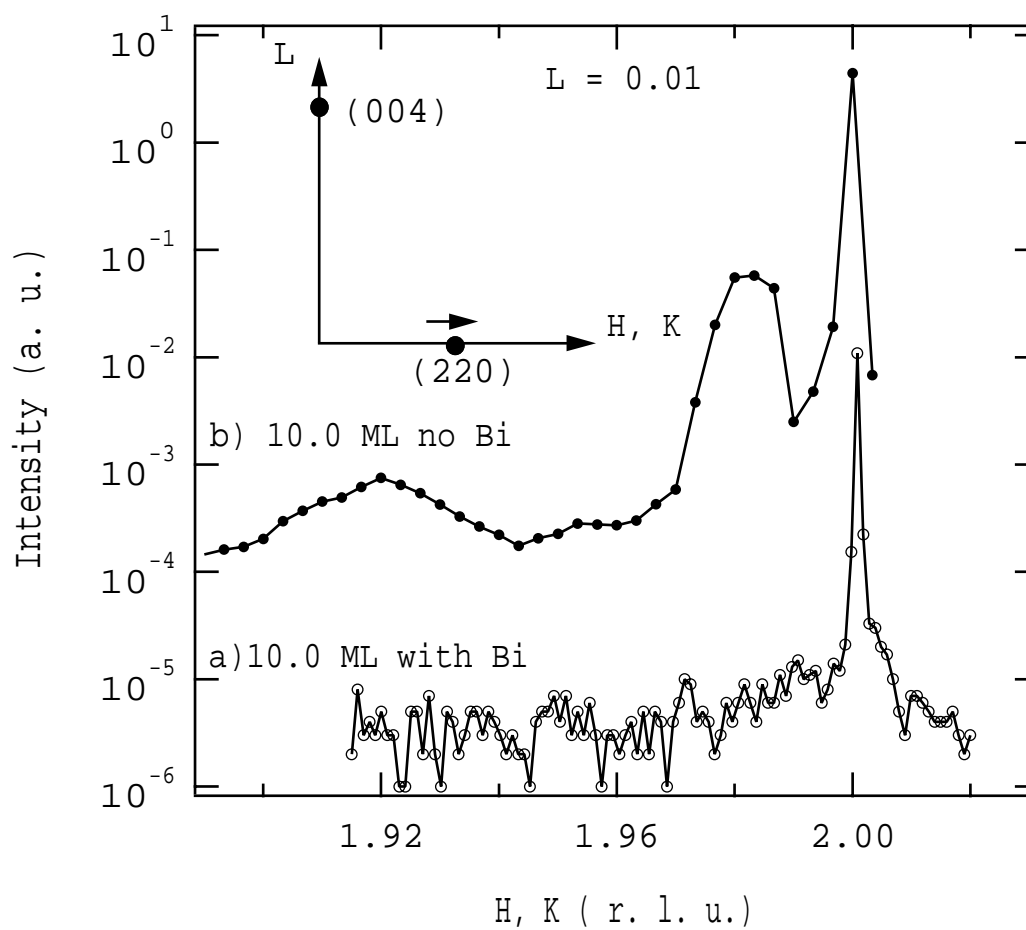


Figure 21: H, K scans through $(22L)$ with $L = 0.01$ for Si/Ge layers with a) 10.0 ML of Ge grown with Bi and b) 10.0 ML of Ge grown without Bi. The scans are shifted vertically for clarity. The inset represents the scanning in reciprocal space.

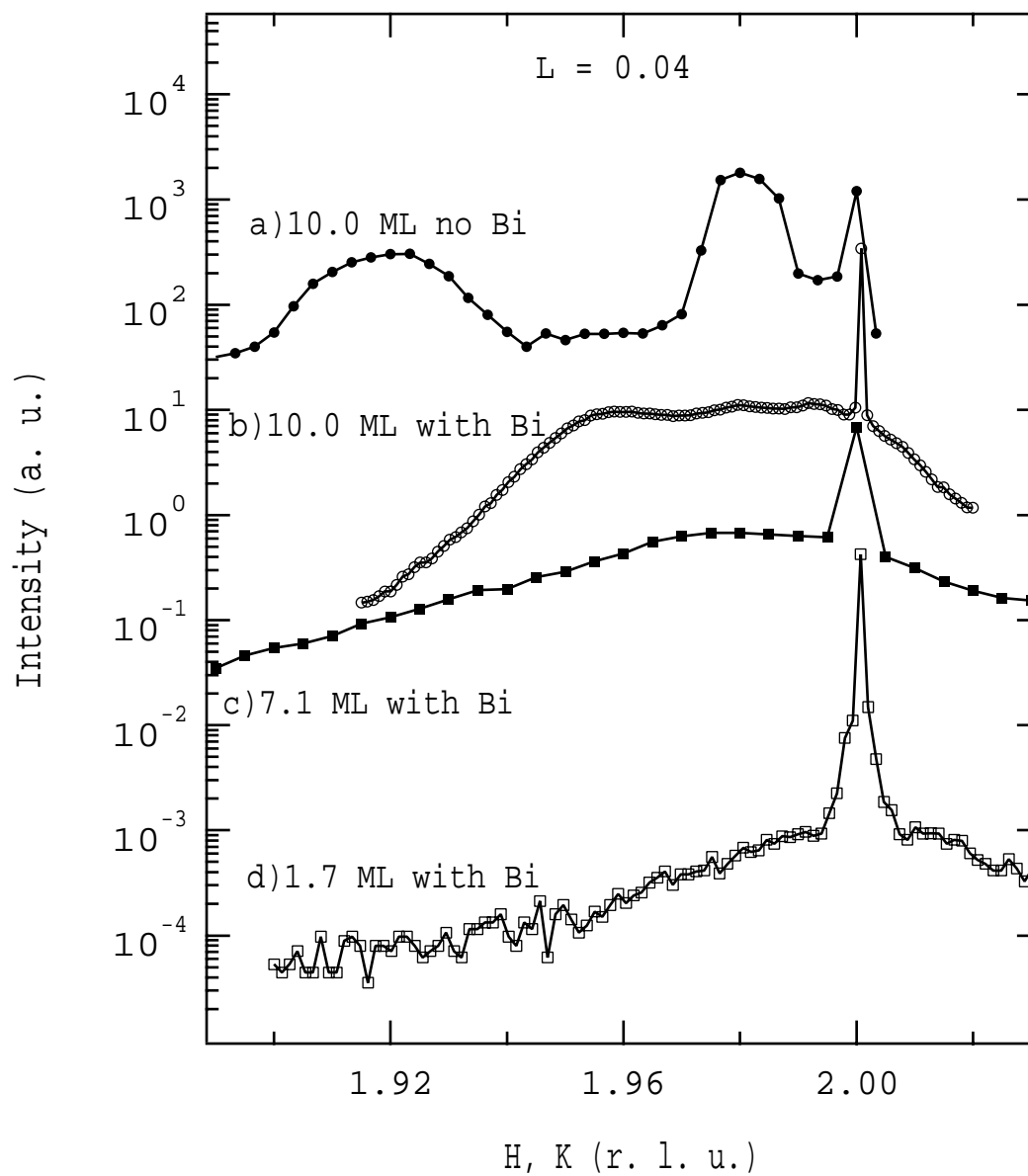


Figure 22: H, K scans through $(22L)$, with $L = 0.04$ for a) 10.0 ML Ge without Bi, b) 10.0 ML Ge with Bi, c) 7.1 ML Ge with BI and d) 1.7 ML Ge with Bi.

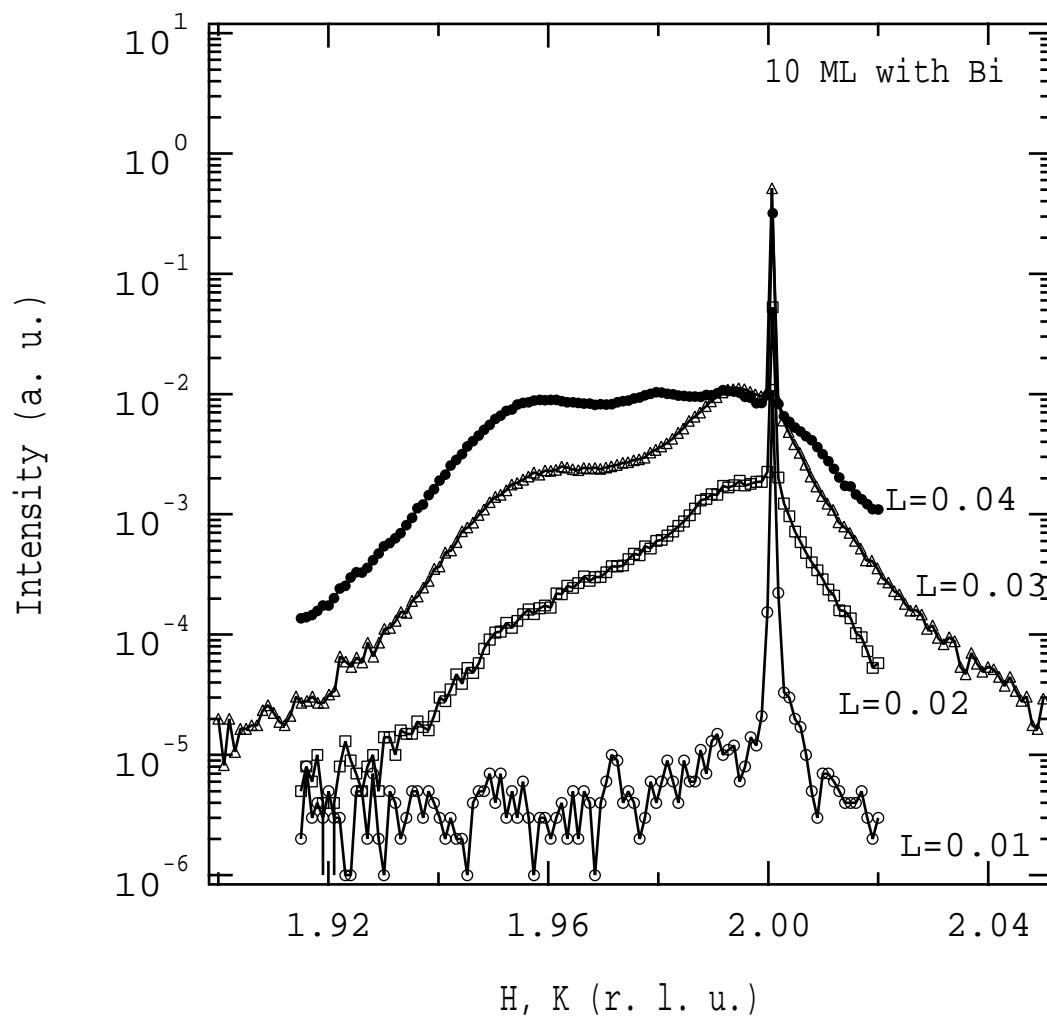


Figure 23: H, K scans through $(22L)$, with various values of L for sample with 10.0 ML of Ge coverage grown with Bi. The scans are shifted vertically for clarity.

the two scans in Figure 21 and Figure 22 had the same three peaks, with the relaxed Ge peak at $H, K = 1.92$ increasing in relative intensity as the scattering depth was increased. As seen in Figure 22 the 7.1 ML Ge film grown with Bi was still pseudomorphic as no scattering was observed at the Ge bulk position of $H, K = 1.92$. For 10 ML Ge film grown with Bi the broad peak in between the Ge and Si bulk positions indicates that the Ge atomic layers were partially relaxed. For a Ge coverage of 1.7 ML the film was found to be completely pseudomorphic. To probe the strain relaxation in the Si/Ge heterostructure as a function of depth we performed additional scans at $L = 0.02$ and $L = 0.03$ for 10 ML sample with Bi, as shown in figure 23. These scans clearly showed the non-uniform nature of the strain.

The x-ray specular reflectivity measurements in figure 24 were compared to the relative electron density profile model shown in figure 25. The periodic oscillations are x-ray interference fringes from the Si cap layer. The following equation derived in chapter 3 was used to calculate the x-ray reflectivity curves for fitting to measured reflectivity.

$$R(Q_z) = R_F(Q_z) \left| \int_{-\infty}^{\infty} \frac{d}{dz} \langle \rho(z) \rangle e^{-iQ_z z} dz \right|^2 \quad (24)$$

The roughness was incorporated as a Gaussian smearing of the interface with σ as the width of the Gaussian. The parameters used in above equation were Si cap layer thickness t_{Si} , Ge layer thickness t_{Ge} , Si cap-Ge interface roughness σ_{Ge} and Si substrate roughness σ_{Si} . An additional 20–25 Å silicon-oxide layer had to be included in the model to fit the data properly. This is from the natural oxidation of Si surface in air. Using the model shown it was not possible to fit the reflectivity curve for 10 ML sample without Bi as it had both 2-D and 3-D structures. For

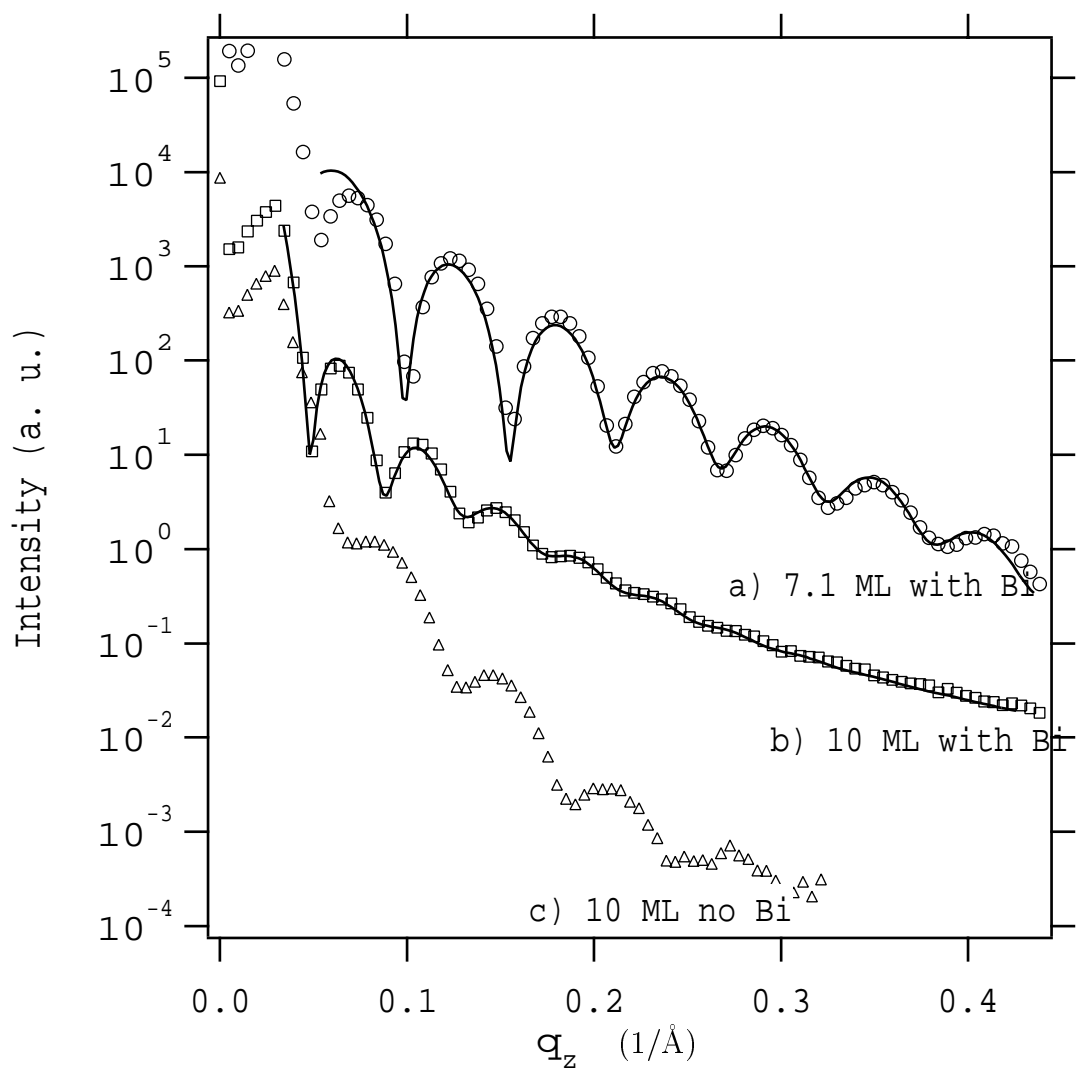


Figure 24: X-ray reflectivity data (points) and model fits (lines) for a) 7.1 ML Ge grown with Bi b) 10.0 ML of Ge grown with Bi. For 10 ML of Ge without Bi only the data is shown.

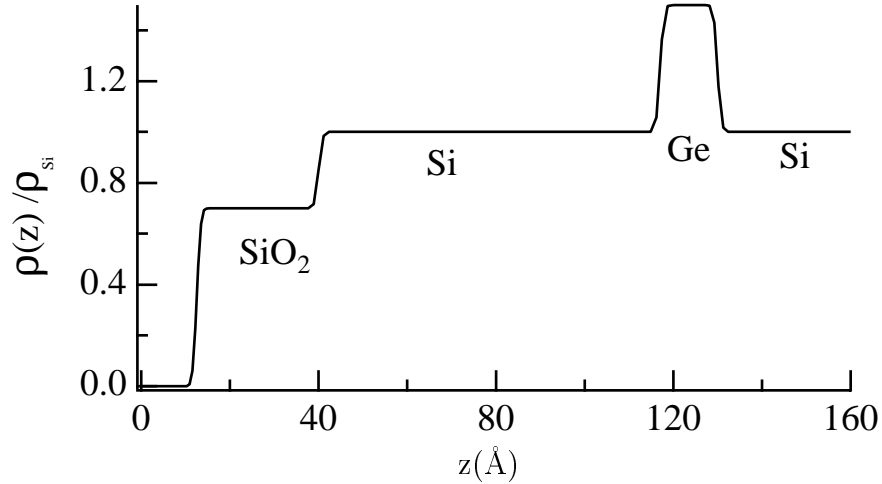


Figure 25: Scattering depth Λ for 11 keV x-rays as function of L . The incident and exit angles are equal.

the 10 ML Ge films the one grown with Bi clearly has sharper interfaces as seen from the oscillations.

The 7.1 ML film grown with Bi has less roughness and sharper interfaces than the 10 ML sample with Bi. The Si substrate roughness was measured to be $5.19 \pm 0.50 \text{ \AA}$ for 7.1 ML Ge sample and $6.35 \pm 0.50 \text{ \AA}$ for the 10 ML Ge sample, which are not very different. This is probably because the Si(001) substrate roughness is determined by the annealing temperature for cleaning the surface prior to growth which is same at 950°C for all samples. The Si cap and Ge layer interface roughness increased $3.20 \pm 0.50 \text{ \AA}$ to $11.53 \pm 0.75 \text{ \AA}$ as the Ge coverage increased from 7.1 ML to 10.0 ML. This increase is very dramatic and is probably because of Ge beginning to relax around 10 ML coverage which is also consistent with our GIXD analysis. The Ge layer thickness of $10.35 \pm 0.50 \text{ \AA}$ and $14.53 \pm 0.50 \text{ \AA}$ agrees very well with our independent coverage measurements of 7.1 ML and 10.0 ML respectively ($1\text{ML} \sim 1.5 \text{ \AA}$).

Our conclusions for the Ge grown on Si(001) with Bi as a surfactant are as follows. Ge has a 4% larger lattice constant than Si, but it wetted the Si surface. This resulted in layer by layer growth of Ge up to 3 ML and thereafter island formation began to relieve the strain in the Ge layer. These islands were faceted with $\{105\}$ planes. The peak at $H, K = 1.92$ was from the Ge layers at the top of the islands which were completely relaxed. Ge segregated in Si and therefore Si growth on Ge resulted in Ge diffusing into the Si layer and the formation of a Si-Ge alloy. This alloy had a lattice constant in between Si and Ge which gave rise to the peak at $H, K = 1.98$. The formation of Ge islands and the Ge-Si intermixing resulted in a very rough and diffuse interface. For the Bi surfactant mediated epitaxy case, Bi segregated strongly in both Ge and Si layers. Due to its larger atomic radius Bi was not easily incorporated into the film. Bi inhibited the diffusion of Ge atoms along the surface, which resulted in layer by layer pseudomorphic growth of Ge up to 7 ML. This is equivalent to that reported by LeGoues *et al* for the case of As as a surfactant [37], while Thornton *et al* measured *in situ* ~ 11 ML of pseudomorphic Ge growth using Sb as a surfactant before the onset of strain relaxation [38]. At 10 ML of Ge, the film with Bi was only partially relaxed. In Figure 23 at $L = 0.02$ ($\Lambda \sim 30 \text{ \AA}$) a weak broad peak appeared at $H, K = 1.99$. The intensity of this peak increased further at $L = 0.03$ ($\Lambda \sim 900 \text{ \AA}$). The absence of such a peak for 1.7 ML of Ge with Bi rules out any intermixing of Ge and Si. We thus infer that the Si atomic layer at the bottom of the cap close to the Ge interface had an in-plane lattice spacing that is about 0.05 % larger than bulk Si. This strain in the Si cap layer at the Si-Ge interface is due to the fact that the underlying Ge had partially relaxed. The presence of Bi on the surface again prevented Ge diffusion and made Si grow layer by layer. In contrast to the Si/10 ML Ge structure grown without Bi, no alloying was observed for the Si/Ge SME

samples. The partially relaxed Ge layer also made the interface rough as seen in the reflectivity measurements. For the SME grown structures the film roughness increased considerably from 7 ML to 10 ML. Roughening increased the surface area and allowed the top Ge layer to partially relax. Interface roughening thus can achieve partial strain relief where island formation is kinetically inhibited. In summary we studied, in the pseudomorphic regime, the strain and morphology of Si/Ge heterostructures grown using surfactant mediated MBE with Bi as the surfactant. Using LEED, AES, GIXD and x-ray reflectivity we observed that Bi segregated to the growth surface, prevented segregation of Ge in Si and promoted layer by layer growth. We found that up to 7 ML of pseudomorphically strained Ge can be grown on Si(001) with Bi. Our measurements indicate that at 10 ML the Ge layers grown with Bi were partially relaxed and strained the Si cap layer. We observed that Ge films grown with Bi as a surfactant undergo partial relaxation by increasing the roughness of the Ge–Si interface.

Chapter 6

X-ray Standing Wave Studies

6.1 Introduction

X-ray standing wave measurements were performed to study the structure and ordering of the Ge layer and the Si cap layer in Si/Ge/Si(001) heterolayer structures grown by surfactant mediated epitaxy (SME) with Bi as the surfactant. A single monolayer of Ge buried in Si(001) has been previously analyzed with XSW by Takahasi *et al* [68] and Falta *et al* [69]. Falta *et al* measured a coherent position of $P_{004} = 1.03$ and coherent fraction of $F_{004} = 0.87$ for 1 ML of Ge buried under 100 Å of Si and grown at 350°C. For a 1 ML Ge SME grown sample with Sb as surfactant they reported a coherent position of $P_{004} = 1.06$ and coherent fraction of $F_{004} = 0.97$. For 1 ML of Ge buried under an 800 Å Si cap layer and grown at 500°C Takahasi measured $P_{004} = 1.058$ and $F_{004} = 0.786$. We studied 1 to 10 ML of Ge buried under Si grown by SME with Bi as the surfactant. As a control, we also studied a Si/Ge/Si(001) heterostructure grown without SME.

6.2 Structural models

As explained in § 3.2, XSW analysis measures the position of atoms with respect to the crystal lattice of the substrate. Ge has a lattice constant greater than that of Si by 4.2%. A single atomic layer of Ge grown on a Si crystal surface will take a position that is above the ideal Si lattice plane. Each successive Ge atomic layer will take up a different position with respect to the spacing of Si lattice planes along the growth direction. Figure 26 shows this pictorially. The geometrical structure factor a_{004} of all of the Ge layers with respect to the Si (004) lattice planes decreases as the number of Ge layers increases. The coherent fraction measured in XSW experiments follows a similar trend. The measured coherent fraction thus has a geometric factor to it purely based on the lattice construction for the Ge layers. We denote this geometric factor by a_H , which is also the modulus of the H th Fourier component of the atomic positions. Assuming each layer with surface normal along H to be a delta-function a_H can be shown to be [46]

$$a_H = \frac{1}{N} \frac{\sin N\pi p_H}{\sin \pi p_H} \quad (25)$$

where N is the number of Ge layers and p_H is the fractional difference between the Ge film lattice spacing and Si substrate lattice spacing for planes of index H . The coherent position P_H measured in XSW experiments is just the average of all the position the Ge atoms take and therefore is

$$P_H = \frac{1}{N} \sum_{n=1}^N n C_n p_H \quad C_n = 1 \text{ for } 0 \leq n < N, \text{ and } C_N = \Theta - [\Theta] \quad (26)$$

where C_n is the occupancy for the n th layer, Θ is the coverage and $[\Theta]$ is the largest integer value less than Θ .

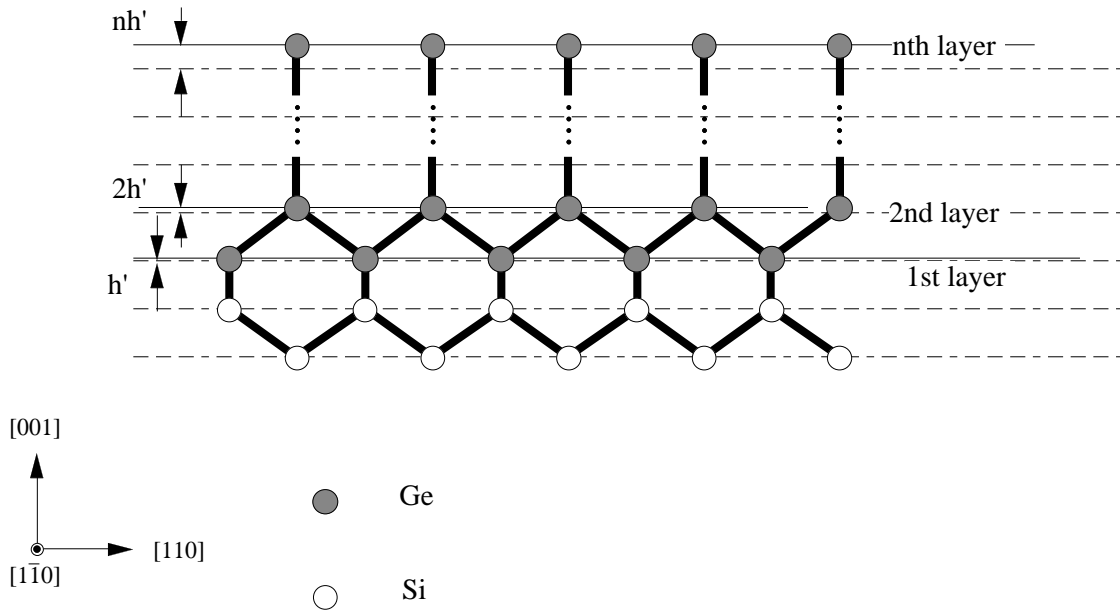


Figure 26: Positions of various Ge layers above the Si substrate. The bulk Si(004) diffraction planes, where $P_{004} = 0$, are represented by the dashed lines.

Let us consider the two extreme cases of Ge grown on Si(001) surface. In the first case the Ge is pseudomorphic or ideally strained and in the second case it is completely relaxed.

6.2.1 Fixed bond length model

For the pseudomorphic case Ge atoms take the same in-plane lattice positions as the Si substrate. Due to the lattice mismatch the Ge lattice is under compression and thus tetragonally distorted. The Ge lattice spacing perpendicular to the surface is greater than the in-plane lattice spacing. We will consider two possible structures for the pseudomorphic case; one in which the bond-lengths are fixed and the lattice distortion is purely due to change in bond-angles; while in the other case both the bond-lengths and bond-angles are changed. In a pure Ge crystal at room temperature and atmospheric pressure the Ge-Ge bond length is 2.451 Å

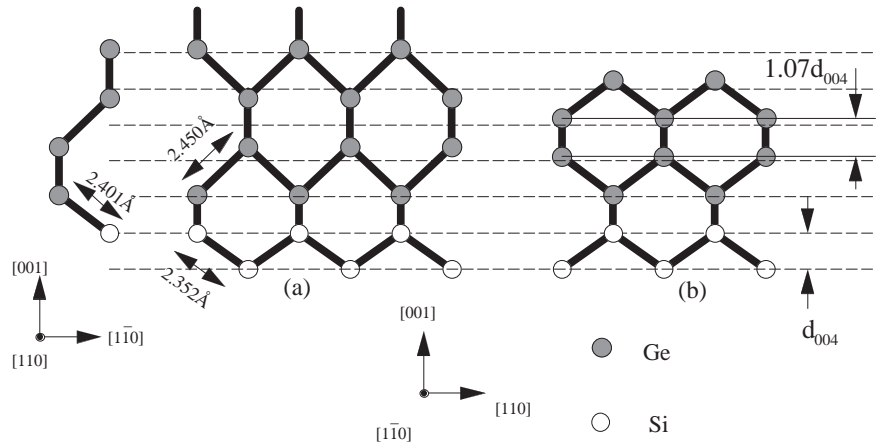


Figure 27: Two structural models for Ge epitaxial growth on Si; (a) bond lengths conserved, (b) continuum elasticity theory model.

and Si–Si bond length is 2.352 Å. For an estimate of the Ge–Si bond length at the interface we would take the average of these two values. The strained lattice for the Ge films that preserves the bond-lengths is shown in figure 27a and the corresponding P_H as a function of number of Ge layers is shown in Figure 28.

6.2.2 Strained Ge layer model based on elasticity theory

Consider the continuum elasticity theory for bulk Ge in which the Ge is biaxially strained in the plane perpendicular to the [001] direction. The strain in the [001] direction, ϵ_{\perp} is then related to the in-plane strain, ϵ_{\parallel} by the elastic constants c_{11} and c_{12}

$$\epsilon_{\perp} = -\frac{c_{12}}{c_{11}}\epsilon_{\parallel} \quad (27)$$

where $c_{11} = 12.40 \times 10^{10} \text{ Nm}^{-2}$ and $c_{12} = 4.13 \times 10^{10} \text{ Nm}^{-2}$ for Ge [70]. For $\epsilon_{\parallel} = 4.2\%$ based on the lattice mismatch between Si and Ge, the Ge lattice then expands by 3.0% in the [001] direction. With respect to the Si lattice the Ge lattice spacing

along the [001] direction is 1.07 larger. Figure 27b shows the lattice reconstruction of Ge film using continuum elasticity theory and the corresponding calculated P_H as a function of coverage is also plotted in figure 28. The coherent position for the first Ge layer turns out to be almost same using continuum elasticity theory (using average of Si and Ge elastic constants) and fixed Si–Ge bond. Note that in figure 27b the Ge–Ge bond length in the strained film is smaller than the bulk value. Also note that the P_H values reported by Falta *et al* for SME grown 1 ML Ge and by Takahasi *et al* closely match each other and also match to the value calculated using the Si–Ge bond length of 2.401 Å, in the fixed bond length model.

Although for 1 ML the Ge positions can be very well explained by fixing the bond-lengths, for elastically strained bulk Ge crystals the lattice is tetragonally distorted. It is interesting to find out what happens when more than one layer of Ge is grown. Which model explains the positions correctly.

6.2.3 Relaxed Ge layer Model

When the Ge film is completely relaxed its lattice spacing in any given direction is larger than the Si lattice spacing by 4.2% which is the lattice mismatch between the two. The P_H as a function of number of Ge layers is also plotted in Figure 28.

6.3 XSW Results and Discussions for Ge

The XSW measurements were performed at the 5ID–C beamline at the Advanced Photon Source in open air. Refer to § 3.2.1 for details about the XSW setup. The b factor was kept at 0.3 by appropriately detuning the two Si channel-cut post-monochromators. The normal (004) and off-normal (022) measurement were performed. The (004) and (022) measurements for various Ge coverages are shown

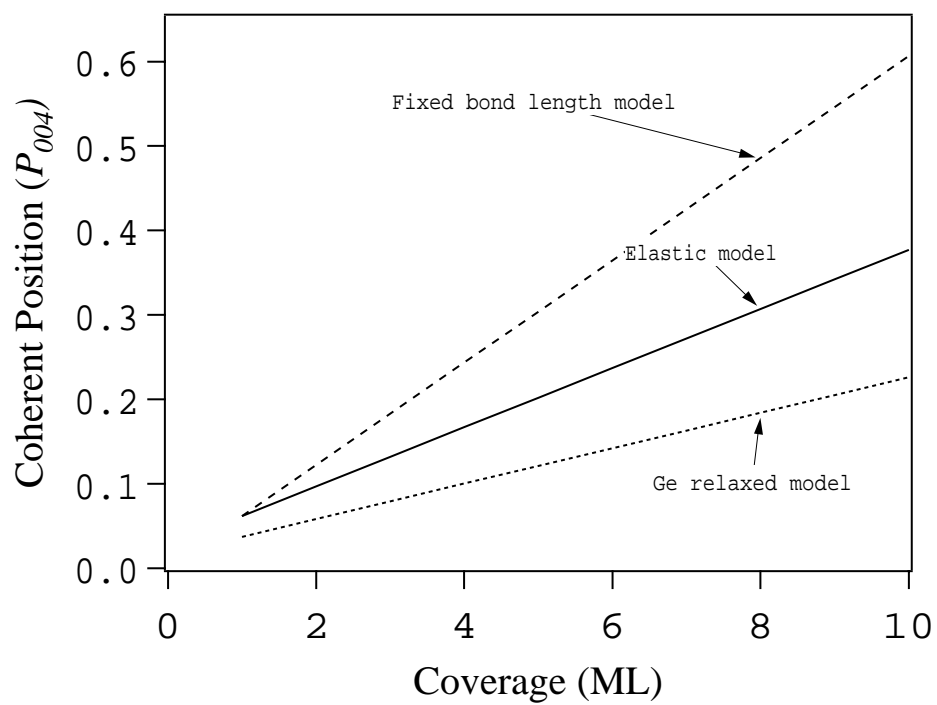


Figure 28: Calculated coherent position of Ge for (a) fixed bond length model, (b) elastic model (c) relaxed Ge model as a function of coverage.

Coverage (ML)	Bi Surfactant?	$F_C(004)$ ± 0.02	$P_C(004)$ ± 0.01	$F_C(022)$ ± 0.02	$P_C(022)$ ± 0.01
1.1	No	0.639	0.026	0.736	0.004
1.6	Yes	0.822	0.063	0.954	0.050
1.7	Yes	0.820	0.062	0.944	0.035
3.0	Yes	0.695	0.122	0.857	0.066
3.4	Yes	0.699	0.135	0.758	0.050
4.6	Yes	0.398	0.187	0.708	0.095
7.1	Yes	0.260	0.337	0.518	0.120
10.0	Yes	0.075	0.045	0.294	0.214

Table 2: Results of (004) and (022) XSW measurements for the Ge for all samples in figures 29 through 36. In each figure the angular dependence of the Ge $K\alpha$ fluorescence yield and the x-ray reflectivity of Si substrate for that particular Bragg reflection are plotted. The circles are measured values while solid lines are based on x-ray dynamical diffraction theory. The angular dependence of the fluorescence yield as described in Chapter 3 is given by the following equation

$$Y(\theta) = Y_{OB}\{1 + R(\theta) + 2\sqrt{R}F_H \cos[v(\theta) - 2\pi P_H]\}. \quad (28)$$

Table 2 list values for F_H and P_H for (004) and (022) reflections for all the samples. Consider a Ge atom at a height h above the top bulk-like Si (004) atomic plane. Then the coherent position of the Ge atom is given by

$$P_{004} = h/d_{004} \quad (29)$$

The projected height of the Ge atom above the (022) lattice planes is $h/\sqrt{2}$ from lattice symmetry. Therefore

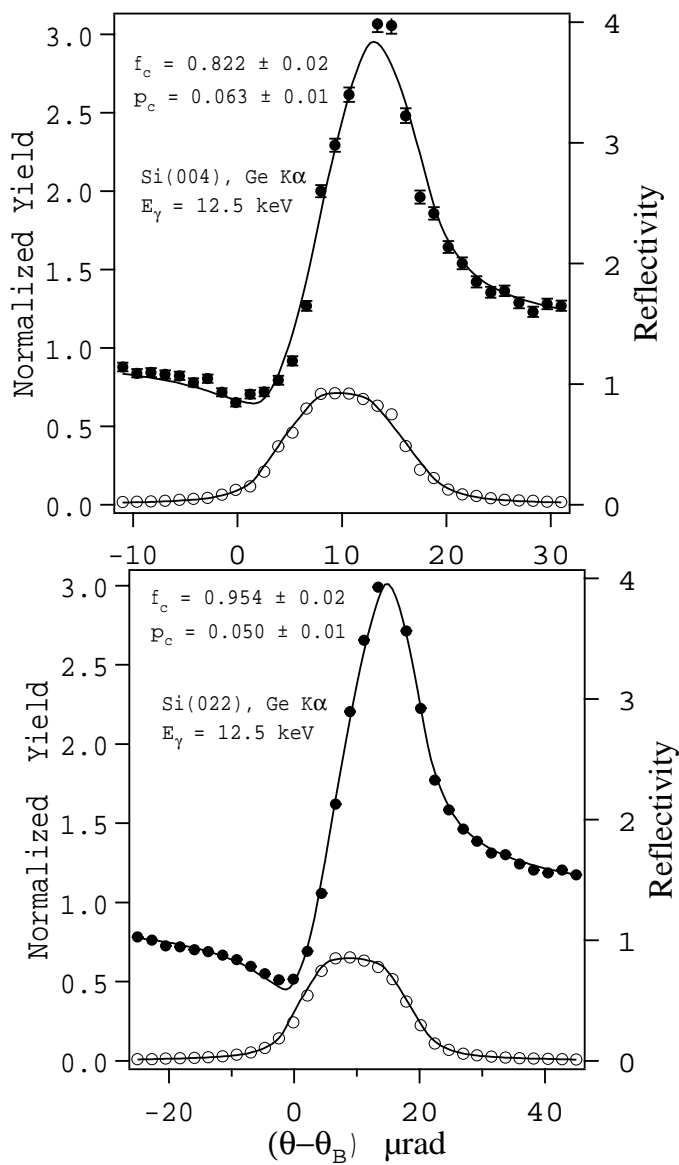


Figure 29: Angular dependence of (004) (top) and (022) (bottom) XSW data and best fit (solid lines) for normalized Ge $K\alpha$ and fluorescence yield and reflectivity for 1.6 ML Ge grown with Bi on Si(001).

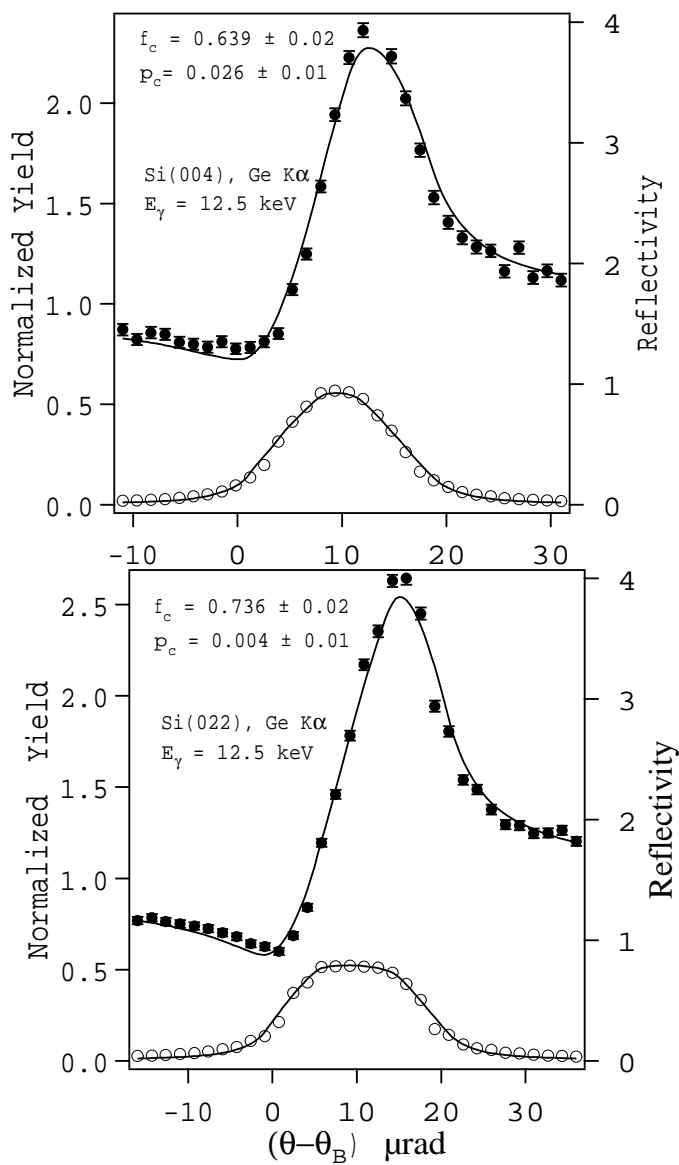


Figure 30: Angular dependence of (004) (top) and (022) (bottom) XSW data and best fit (solid lines) for normalized Ge K α and fluorescence yield and reflectivity for 1.1 ML Ge grown on Si(001).

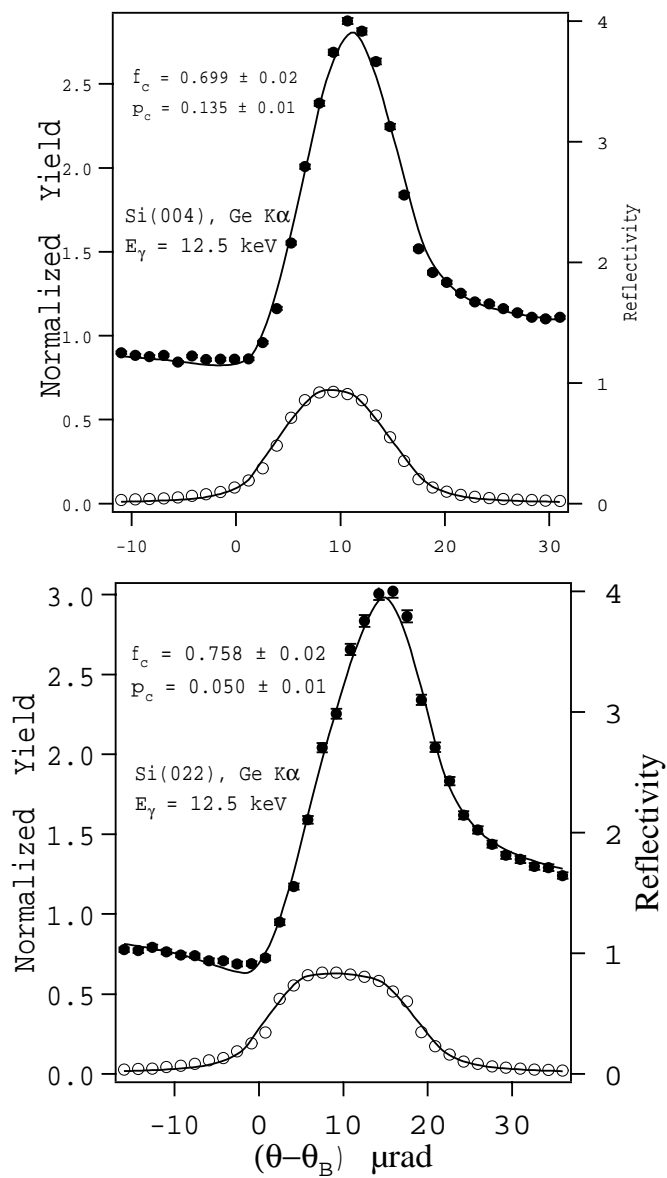


Figure 31: Angular dependence of (004) (top) and (022) (bottom) XSW data and best fit (solid lines) for normalized Ge K α and fluorescence yield and reflectivity for 3.4 ML Ge grown with on Si(001).

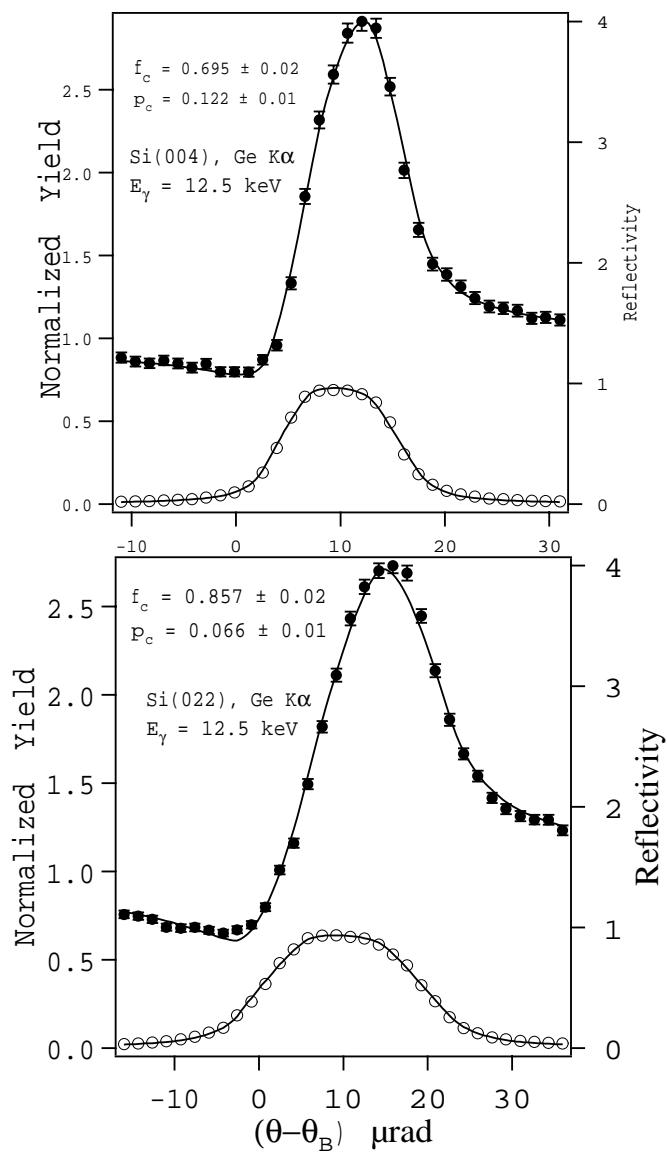


Figure 32: Angular dependence of (004) (top) and (022) (bottom) XSW data and best fit (solid lines) for normalized Ge $K\alpha$ and fluorescence yield and reflectivity for 3.0 ML Ge grown with Bi on Si(001).

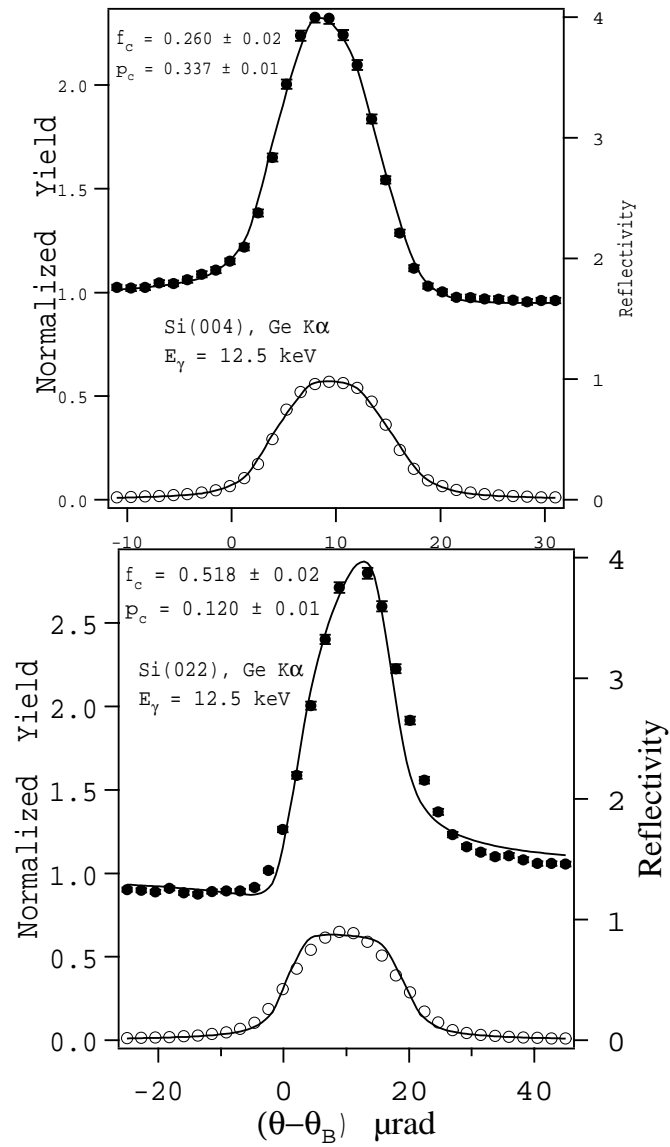


Figure 33: Angular dependence of (004) (top) and (022) (bottom) XSW data and best fit (solid lines) for normalized Ge $K\alpha$ and fluorescence yield and reflectivity for 7.1 ML Ge grown with Bi on Si(001).

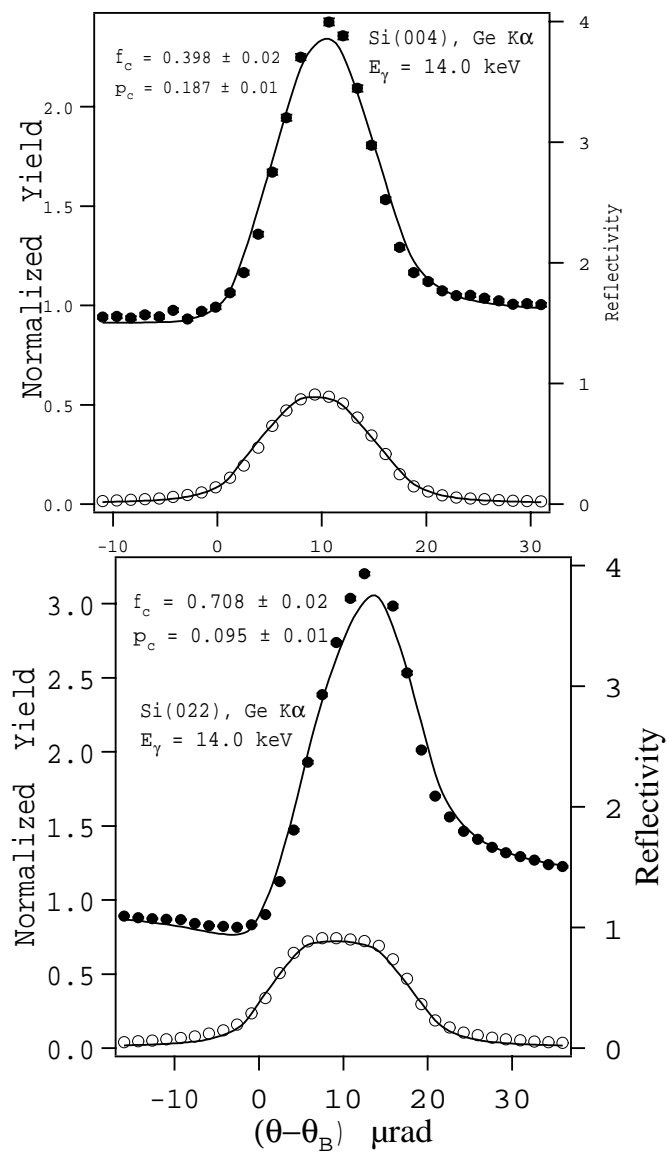


Figure 34: Angular dependence of (004) (top) and (022) (bottom) XSW data and best fit (solid lines) for normalized Ge $K\alpha$ and fluorescence yield and reflectivity for 4.6 ML Ge grown with Bi on Si(001).

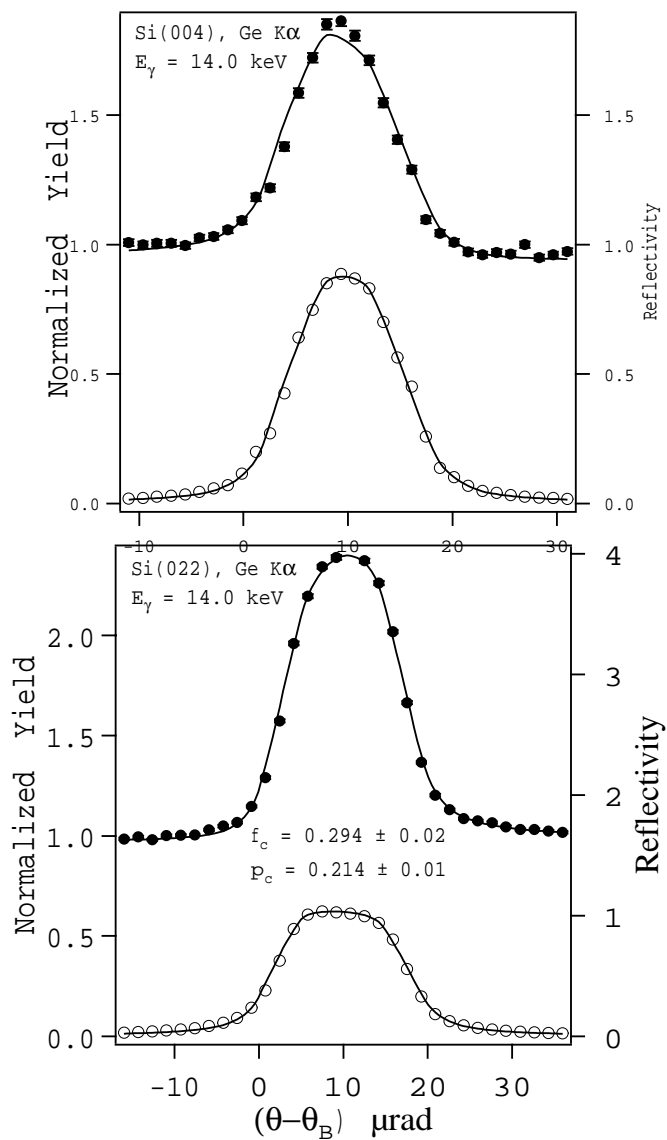


Figure 35: Angular dependence of (004) (top) and (022) (bottom) XSW data and best fit (solid lines) for normalized Ge $K\alpha$ and fluorescence yield and reflectivity for 10.0 ML Ge grown with Bi on Si(001).

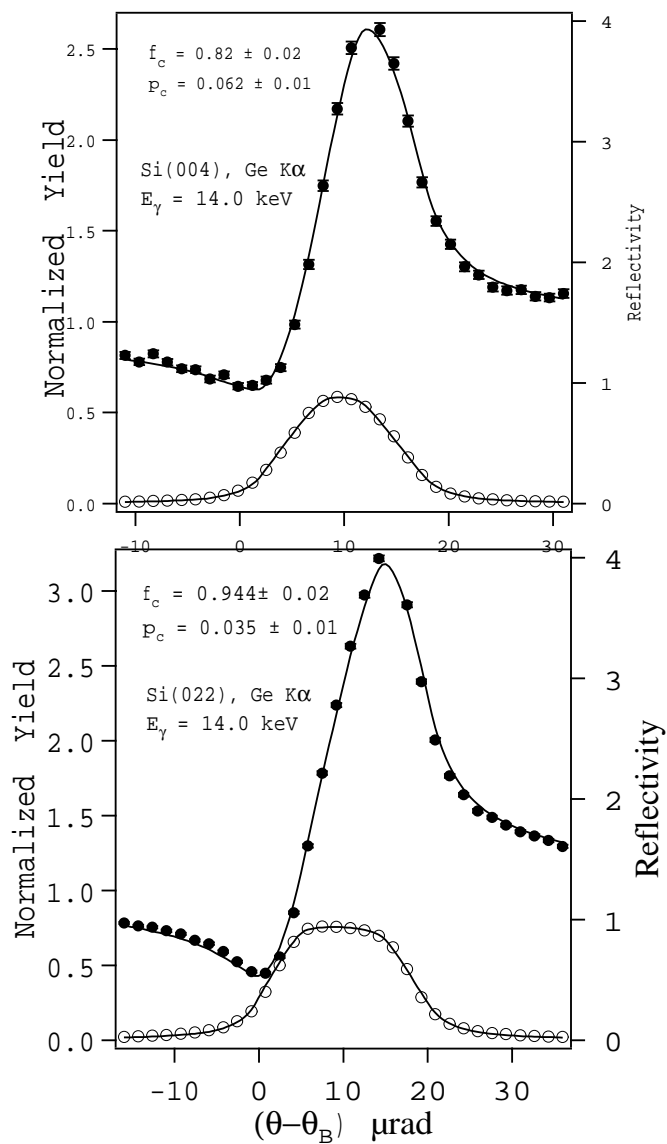


Figure 36: Angular dependence of (004) (top) and (022) (bottom) XSW data and best fit (solid lines) for normalized Ge $K\alpha$ fluorescence yield and reflectivity for 1.7 ML Ge grown with Bi on Si(001).

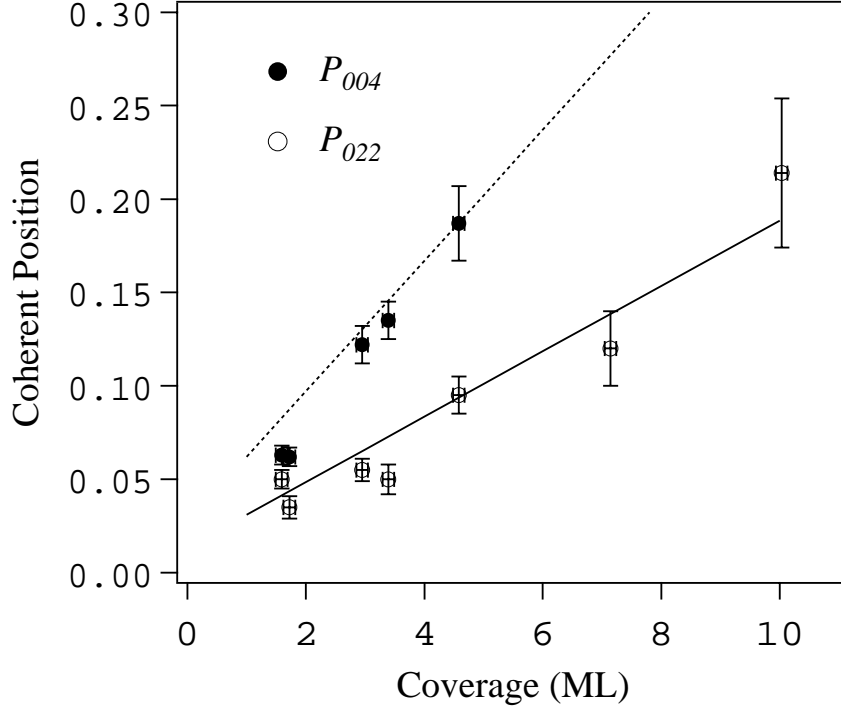


Figure 37: Ge (004) and (022) measured positions (markers) and calculated positions (lines) using continuum elasticity theory as a function of Ge coverage.

$$P_{022} = \frac{h}{\sqrt{2}d_{022}} \quad (30)$$

But $d_{022} = \sqrt{2}d_{004}$ and therefore using equations 29 and 30 we find that

$$P_{022} = P_{004}/2 \quad (31)$$

In figure 37 the measured coherent positions are plotted against the measured Ge coverage, Θ for the (004) and (022) reflections. The Ge coverage calibration is discussed in § 4.5. The solid lines are calculated coherent positions. For the first layer of Ge we fixed the Ge–Si bond length. For all successive layers we expanded the lattice for the Ge films given by the continuum elasticity theory. As

seen in figure 37 our model agrees very well with our data for a coverage below 7 ML. At 10 ML it agrees well only for the (022) reflection. From equation 25 the Ge geometrical factor a_{004} and therefore the coherent fraction F_{004} drops sharply as the Ge coverage increases beyond 7 ML. Therefore at higher coverages the measurement (according to equation 28) is not sensitive to the coherent position because the coherent fraction is below 10%. The measured coherent fractions are plotted in figure 38. For the (004) measurements the coherent fraction are lower than that for the (022), as expected. While the coherent positions agree remarkably with theory, the measured coherent fractions are markedly lower than the calculated values from the equation:

$$F_H = D_H^T \cdot a_H \quad . \quad (32)$$

Here D_H^T is the dynamic Debye–Waller (DW) factor and a_H is the geometrical factor defined in equation 25.

The dynamic DW factor only takes into account the thermal vibrations of the atoms and is given by $e^{-2\pi^2\langle u_H^2 \rangle/d_H^2}$ where $\sqrt{\langle u_H^2 \rangle}$ is the root mean square of the Ge vibrational amplitude in the H direction. For our room temperature measurements we used $D_{004} = 0.95$ and $D_{022} = 0.98$, based on bulk Ge vibrational amplitude of 0.068 Å. Various other factors can contribute to the lowering of the coherent fraction. The main factors are randomly distributed Ge atoms, defects and static variations in the atomic positions. Randomly distributed atoms do not take any particular positions and they do not affect the measured P_H value. Higher order harmonic XSW measurements and temperature dependent XSW measurements can be used to separate out these factors. One such higher order (008) measurement is discussed in § 6.3.4. Our measured P_H values at our measured coverages are

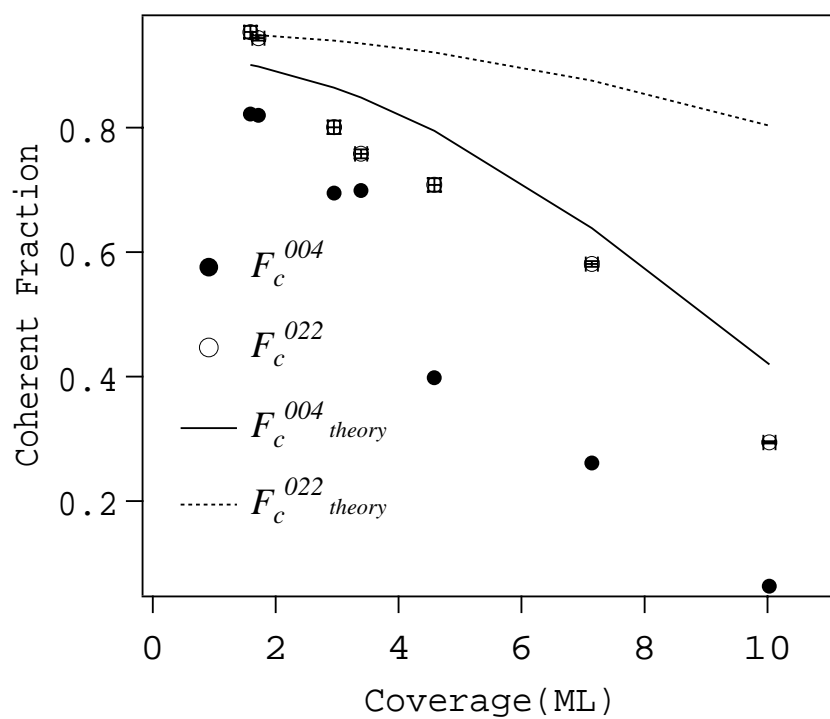


Figure 38: Ge (004) and (022) measured coherent fractions (markers) and calculated coherent fractions (lines) using continuum elasticity theory as a function of Ge coverage.

consistent with the elastic model. Therefore the fraction of randomly distributed Ge atoms is negligible. Equation 32 does not take into account defects in the Ge film which can lower the coherent fraction. These defects can be accounted for by a static DW factor D_H^s , which like the thermal DW factor assumes a Gaussian distribution for the displacement of the Ge atoms about the equilibrium strained lattice positions. We will consider two different models with static DW factor to explain the reduced coherent fraction. In model 1 we consider the static DW factor to be independent of the layer position while in model 2 we assume it to be dependent on the layer position.

6.3.1 Model 1 for Static Debye–Waller Factor

In this model we assume that the defects are evenly spread throughout the Ge film along a particular crystal direction. The number of defects per layer increases as the number of layers increases. We assume the defects have a Gaussian distribution, $\frac{1}{\sigma_H\sqrt{2\pi}}e^{-x^2/2\sigma_H^2}$, where σ_H is the width of the distribution and the distribution is same for all layers. Note that the area under this distribution is still unity except in the case when the top most Ge layer is not complete, in which case it is equal to the fractional occupancy for that layer. It can then be shown that the static DW factor (e^{-W}) is just the Fourier transform of the Gaussian atomic distribution function and is $e^{-2\pi^2\sigma_H^2/d_H^2}$. The coherent fraction then can be written as

$$F_H = D_H^s \cdot D_H^T \cdot a_H \quad (33)$$

where a_H is still the geometrical factor as defined in equation 25. Using our measured values for F_H in equation (33) the static DW factor and σ_H are calculated and shown in figure 39 for (004) and in figure 40 for (022) reflections. It follows

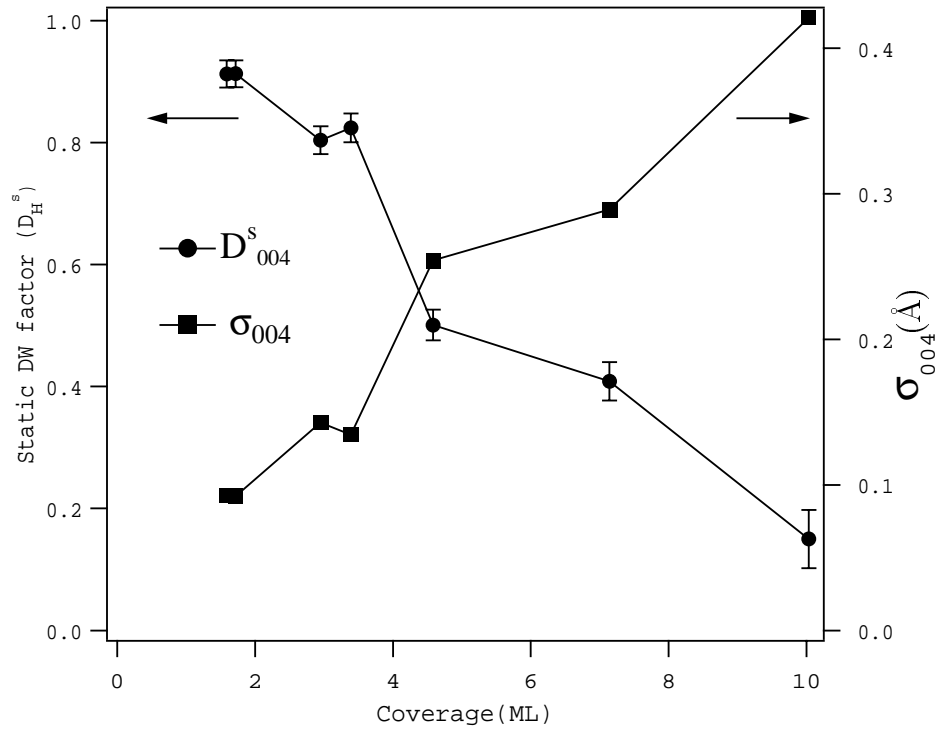


Figure 39: Calculated values of static DW factor and σ_{004} as a function of Ge coverage.

the same trend as measured F_H . For Ge coverage below 5 ML $\sigma_{004} < \sigma_{022}$ while above 5 ML Ge coverage $\sigma_{004} \sim \sigma_{022}$.

6.3.2 Model 2

In model 1 all layers are assumed to be identical to each other. Although, model 1 can explain the lower coherent fraction it is still oversimplified. As our samples were grown with Bi as a surfactant at a moderate temperature (400°C) the Ge/Si heterostructures are metastable. The Ge atomic layers in a given film are therefore not identical to each other. In model 2 the static DW factor will be a function of the layer position. We still assume Gaussian distribution as explained in model 1

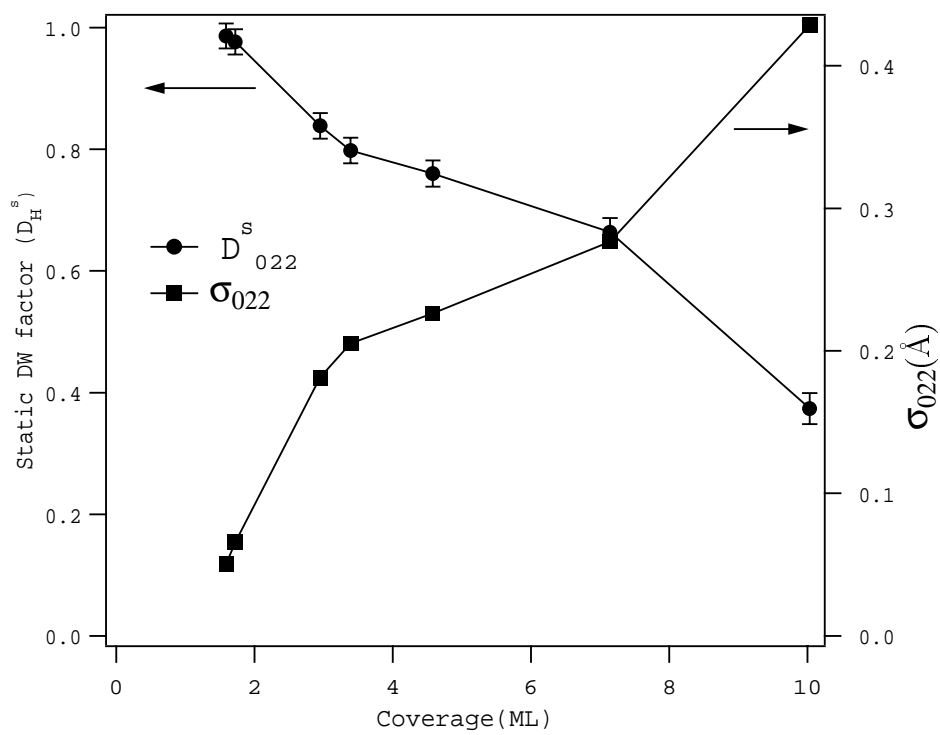


Figure 40: Calculated values of static DW factor and σ_{022} as a function of Ge coverage.

for each layer but the width of the distribution σ_H is different for different layers. However, the area under the Gaussian does not vary from layer to layer and is fixed to 1 except for the top most layer as explained before. The atomic distribution functions are shown in figure 41. In this model we assume that as the number of Ge layers increase they become more disturbed from their ideal positions. These deviations could be from local relaxation of Ge atoms and therefore should increase as more and more layers are added. The successive relaxation of Ge layers probably has a quadratic dependence as a function of height above the Si–Ge interface [19]. Therefore, in our model 2 we allowed the width of the Gaussian peak to increase linearly with the layer height. Note that the mean atomic positions remain unchanged. The geometric factor then can be written as

$$a_H = \left| \sum_{n=1}^N C_n e^{-2\pi^2 \sigma_{n,H}^2 / d_H^2} e^{2\pi i n p_H} \right| \quad (34)$$

where C_n is the fraction of the total atoms in n th layer, d_{hkl} is the d-spacing between the planes and $\sigma_{n,H} = \sigma_{1,H} + (n - 1)\Delta\sigma_H$ is the width for the n th layer. The static DW factor $e^{-W_{n,H}} = e^{-2\pi^2 \sigma_{n,H}^2 / d_H^2}$ for the n th layer.

Using equation 34 the P_H and F_H are fitted to the data using $\sigma_{n,H}$ as a parameter. For (004) reflection $\sigma_{1,004} = 0.044 \text{ \AA}$ and $\Delta\sigma_{004} = 0.052 \text{ \AA}$. For (002) reflection $\sigma_{1,022} = 0.040 \text{ \AA}$ and $\Delta\sigma_{004} = 0.036 \text{ \AA}$. The fits using model 2 for F_H are shown in figure 42. The coherent position P_H is invariant to the width of the atomic distribution, since the mean position does not change and the distribution function is symmetric for each layer. In thicker Ge films, for the topmost Ge layer $\sigma_{N,004}$ is comparable to the d_{004} for Si. As seen from our model $\sigma_{n,022} \leq \sigma_{n,004}$. Therefore the Ge atoms deviate more from their expected positions perpendicular to the plane than in the plane.

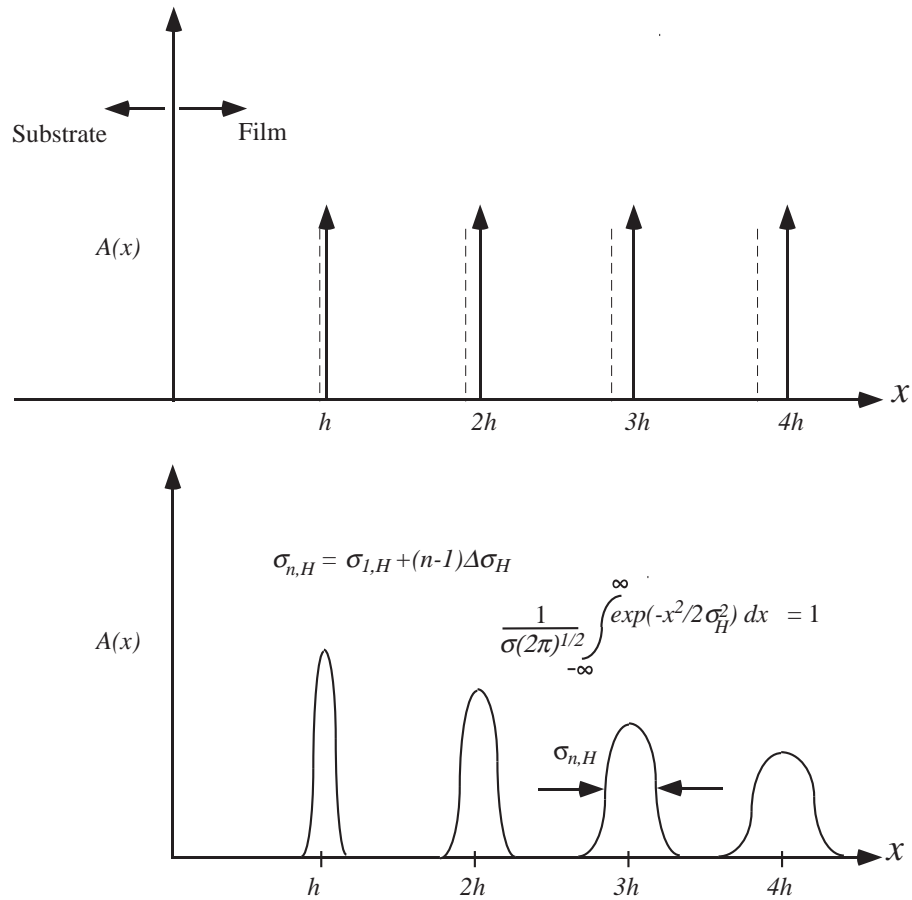


Figure 41: Atomic distributions for Ge layers grown on Si(001) using Bi as the surfactant. (a) Ideal model with each layer uniformly strained and no defects. Each layer is designated by a delta-function. The dotted lines are positions that Si atoms would occupy. (b) A Gaussian distribution for layers to incorporate defects within a layer used in model 2. The width of the distribution increases linearly with the layer number.

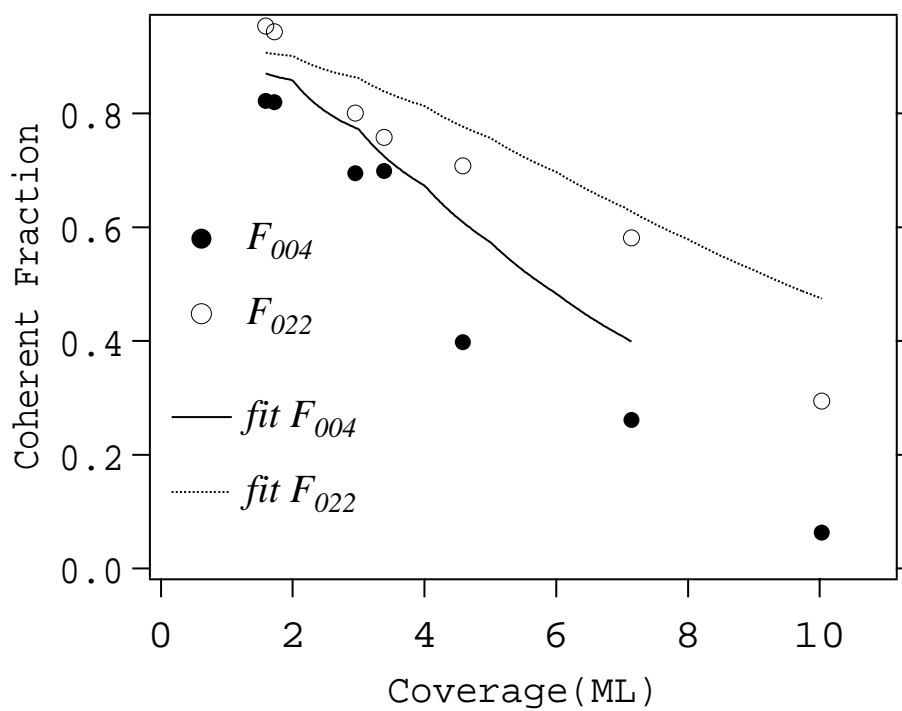


Figure 42: Fits to data (dots) for F_{004} and F_{022} using non-uniform static Debye-Waller factor as in model 2.

The Ge atoms can have slight deviations from their expected positions. If we assume that these deviations have a Gaussian distribution about the expected lattice positions then P_H will not change but F_H will be lowered. These defects can be taken into account by the static Debye–Waller factor D_H^s .

The origin of the defects is quite possibly from the local relaxation of Ge lattice that is tetragonally distorted. These defects increase in magnitude as more layers of Ge are grown. The width $\sigma_{n,H}$ thus increases as the number of Ge layers increase. The anisotropy along the [004] and [022] directions for $\sigma_{n,H}$ can be understood from the constraints due to the Si lattice. The [004] direction is normal to the growth plane while [022] is off-normal and therefore has an in-plane component. In-plane the Ge atoms are constrained by the underlying Si lattice which is presumably defect free. The Ge atoms are fixed to the Si lattice positions in-plane and therefore strained because of the lattice mismatch. In-plane the Ge atoms are less likely to deviate from their positions as that would require modifying the underlying Si lattice. Along the [004] direction there is no stress and so the Ge atoms take positions different from the Si lattice. The Ge atoms take positions that would minimize the total strain energy. Variations in Ge atomic positions along the [004] direction do not significantly affect the in-plane lattice structure. Therefore the Ge atoms are more likely to deviate along the [004] direction. We interpret the lower width for $\sigma_{n,022}$ from its in-plane component. Assuming an ellipsoid one can calculate the in-plane widths $\sigma_{n,\parallel}$ using the values of $\sigma_{n,004}$ and $\sigma_{n,022}$ from model 2 as

$$\frac{1}{\sigma_{n,\parallel}^2} = \frac{2}{\sigma_{n,022}^2} - \frac{1}{\sigma_{n,004}^2}. \quad (35)$$

Since in model 1 individual layers are not considered it may be more applicable

for lower (< 3 ML) Ge coverages. At higher Ge coverages the topmost Ge layers are likely to be more defective than the Ge layers close to the Si substrate and therefore model 2 may be more applicable.

6.3.3 Effect of surfactant

Ge layers grown on a Si(001) surface without surfactants has been extensively studied. It has been now accepted that Ge grows up to 3ML pseudomorphically and thereafter relaxes by island formation. To date there is no reported XSW study of Ge films grown beyond 1 ML without surfactants. We attempted to do a similar study on samples grown without Bi as a surfactant for comparison. As far as *ex situ* measurements are concerned there is a problem. To protect the Ge in open air a Si cap layer has to be grown on top of it. But due to the lower surface energy of Ge than that of Si, Ge segregates into Si to the surface. A direct comparison is therefore not available. The Ge segregation can be inhibited in the absence of any surfactant by growing the samples at room temperature or below. But low temperature growth has shown to result in many defects and generally poor crystallinity. This problem can be solved by performing the measurements in UHV where there is no need for a protective cap layer. We have recently acquired such a capability and therefore it is a topic of future experiments.

We looked at one sample that had 1ML of Ge, buried under a Si cap, grown without Bi but otherwise under identical growth conditions. The XSW measurements for 1ML Ge without Bi and 1.6 ML Ge with Bi are shown in figure 43. Even though the Ge coverage in the SME grown sample is higher, we measured higher coherent fraction and coherent position than for the non-SME grown sample. This clearly shows that Bi prevented segregation of Ge in Si cap as also confirmed by

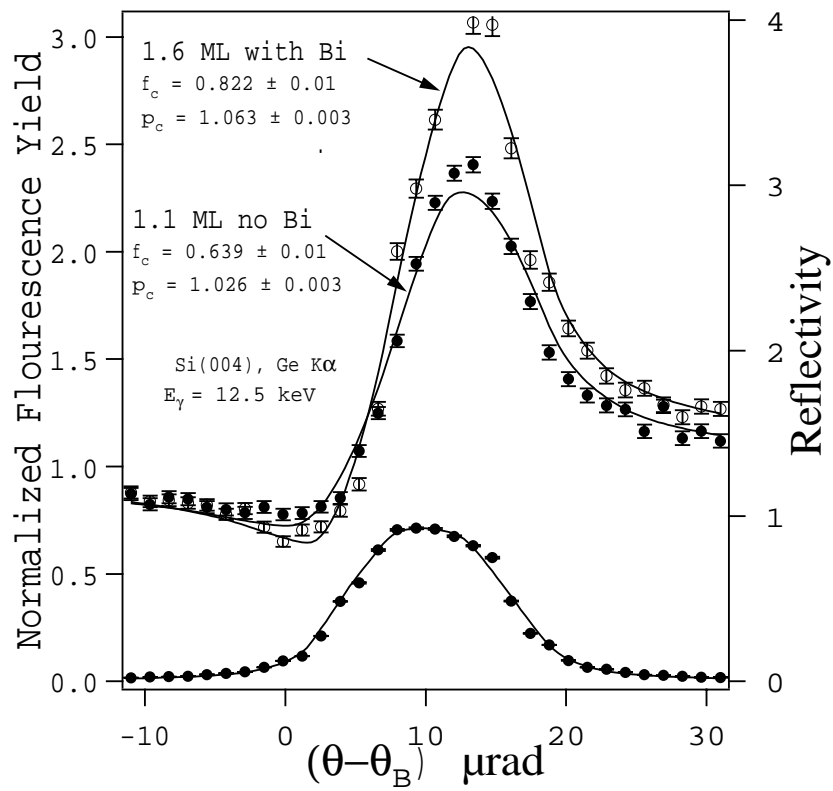


Figure 43: Angular dependence of (004) XSW data (markers) and best fit (solid lines) for Ge $K\alpha$ fluorescence yield and reflectivity for 1.6 ML Ge with Bi and 1.1 ML without Bi on Si(001).

our *in situ* LEED and AES observations (see chapter 4). The lower coherent fraction and coherent position for non-SME growth is consistent with Ge segregation in Si.

6.3.4 XSW (008) Measurement

XSW measurements can be used to calculate the root mean square thermal vibrational amplitudes of adsorbate atoms [71]. Two XSW measurements are necessary to calculate the vibrational amplitude along a particular H direction. Therefore the combination of a (004) and a (008) measurement on the same sample can be used to calculate the vibrational amplitude along the [001] direction. Lyman *et al* [72] have used (008) and (004) reflections to calculate the RMS vibrational amplitude of adsorbates. Ideally the coverage of the adsorbate should be less than 1 ML so that there is only one unique position i.e. $a_{004} = 1$. Although we did not have such a sample we did (008) measurement for the 1.7 ML Ge sample as it had the highest coherent fraction. (The 1 ML Ge sample grown without Bi was not suitable because a significant amount of Ge had segregated into the Si cap layer.) The root mean square vibrational amplitude can be written as

$$\langle u_{001}^2 \rangle = -\frac{d_{004}^2}{6\pi^2} \ln \left(\frac{F_{008} \cos(\pi p_{004})}{F_{004} \cos(n\pi p_{004})} \right) \quad (36)$$

where $n = 1.7$ is the number of layers. Figure 44 shows the XSW measurements for the (004) and (008) reflections at $E_\gamma = 11.2$ keV. Note that $P_{008} = 2P_{004}$ since $d_{004} = 2d_{008}$. Using our XSW measured values of $F_{008} = 0.36$ and $F_{004} = 0.81$ we calculate from equation 36 a room temperature RMS vibrational amplitude of $\sqrt{\langle u_{001}^2 \rangle} = 0.15 \pm 0.01$ Å. This value is higher than the bulk thermal vibrational amplitude for bulk Ge ~ 0.068 Å calculated using Debye temperature of 360 K [73].

Without changing the temperature, one cannot separate the thermal vibrational amplitude and static width σ_H . Therefore our above measurement of $\sqrt{\langle u_{001}^2 \rangle}$ also has a contribution from the static DW effect. The difference between our measured value of $\sqrt{\langle u_{001}^2 \rangle} = 0.15 \text{ \AA}$ and the bulk vibrational amplitude is 0.08 \AA . This can be considered as the value for σ_{004} for 1.7 ML Ge coverage.

The (008) rocking-curve width is much narrower than the (004) and therefore very sensitive to angular drift. To avoid the sample drift problem we scanned the piezo driven rotary stage motor of the first Si(008) channel cut of the post monochromator. The rotation of second Si(008) channel cut which was locked by electronic feedback to the first one then followed automatically. This constitutes an energy scan with a very narrow range 0.07 eV that is much smaller than the energy bandpass 2.95 eV from the high-heat load Si(111) monochromator.

6.4 XSW Results of Si Cap

At a growth temperature above 350°C the Si cap layer above the Ge should be epitaxial and have the same lattice constant as the Si substrate if the Ge layer is pseudomorphically strained. The Si cap lattice will be shifted with respect to the Si substrate lattice by $h + h'$ where h is the position of the top most Ge layer and h' is the additional height due to the difference between Si-Si and Si-Ge bond lengths. The XSW determination of the displacement of the Si cap with respect to the Si substrate is another way to study the strain in the buried Ge film.

6.4.1 X-ray evanescent wave effect

To measure the cap displacement by the XSW technique the Si $K\alpha$ signal from the cap should be effectively isolated from the strong Si $K\alpha$ signal from the bulk. This

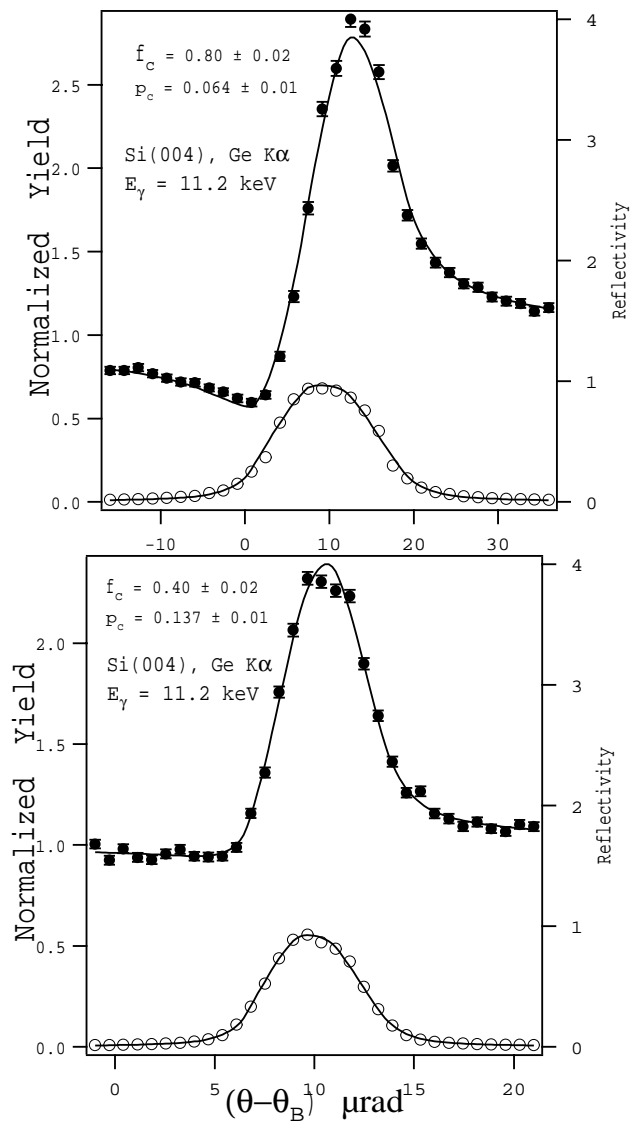


Figure 44: Angular dependence of (004) (top) and (008) (bottom) XSW data and best fit (solid lines) for normalized Ge $K\alpha$ and fluorescence yield and reflectivity for 1.7 ML Ge grown with Bi on Si(001).

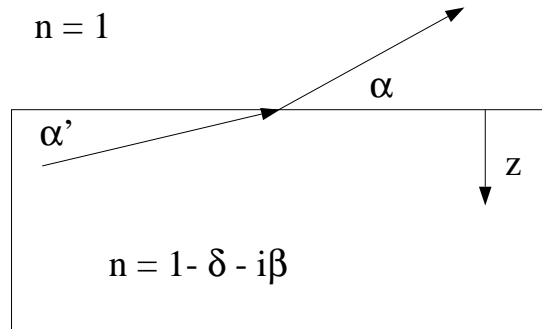


Figure 45: X-ray evanescent wave emission effect to probe surface layers.

could be accomplished by using the surface sensitivity of photoelectron emission. With the usual XSW technique based on fluorescence measurements the surface sensitivity required can be achieved by using the evanescent wave-emission (EW) effect. This EW effect was first demonstrated by Becker *et al* [56] and later combined with the XSW method and used to measure buried layers by Lee *et al* [74].

The emitted fluorescent x-rays are refracted at the surface as show in figure 45. X-rays undergo total external reflection when $\alpha = \alpha_c$, $\alpha' = 0$, where α_c is the critical angle. For $\alpha \leq \alpha_c$ the emission is explained by an exponentially damped evanescent wave. Using the optical reciprocal principle the intensity I_{out} of the fluorescence x-ray emitted from depth z below the surface as a function of angle is given by

$$I_{out}(\alpha, z) \propto I_s(\alpha)e^{-\mu_z(\alpha)z} \quad (37)$$

where I_s is the intensity of the fluorescence x-ray emitted from the surface. The “effective” linear absorption coefficient μ_z is related to the index of refraction $n = 1 - \delta - i\beta$ as [74]

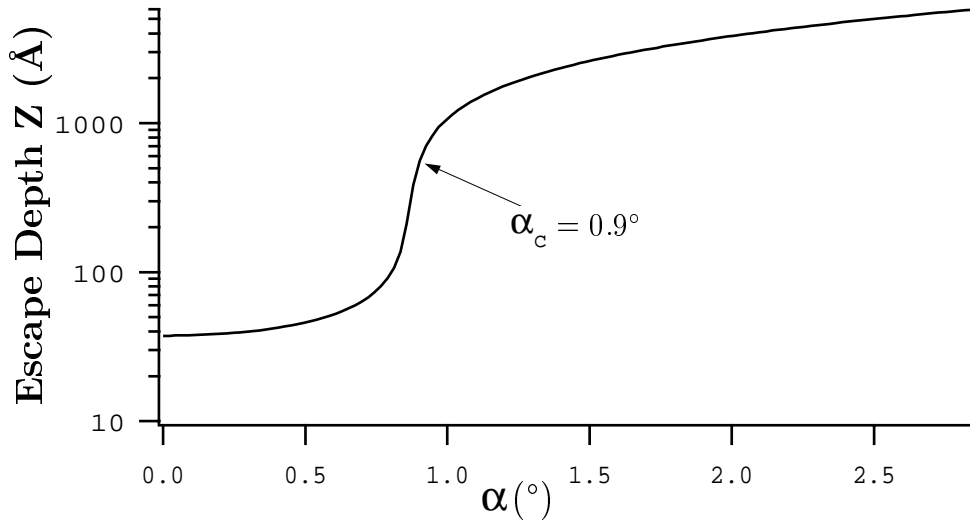


Figure 46: Escape depth of Si K α fluorescence in Si as function of take-off angle.

$$\mu_z = \frac{4\pi}{\sqrt{2}\lambda_2} \{[(2\delta - \alpha^2)^2 + 4\beta^2]^{1/2} + 2\delta - \alpha^2\}^{1/2} \quad \text{for } \alpha \gg \alpha_c \mu_z = \mu_0 z / \sin \alpha. \quad (38)$$

The Si K α energy is 1.74 keV and the critical angle for this wave in Si is $\alpha_c = \sqrt{2\delta} = 0.9^\circ$. Figure 46 shows the calculated escape depth $Z = \mu_z^{-1}$ as a function of take-off angle α . Z has a minimum value of 36 Å at $\alpha = 0$ and then dramatically increases at $\alpha = \alpha_c$. This abrupt reduction in the escape depth below the critical angle makes this technique surface sensitive. All our samples had approximately a 100 Å thick Si cap layer on top of the Ge layer. Below the critical angle at about 0.9° the fluorescence x-rays emitted from the Si substrate will not reach the detector.

The XSW measurements of the Si cap were done using a slit in front of the solid state fluorescence detector. The slit was scanned vertically and the Si K α fluorescence was monitored. The slit was then positioned so that the take-off angle was just below the critical angle. XSW measurements for the (004) reflection were

then carried out as usual. To verify that the contribution to the Si fluorescence signal from the substrate was negligible the slit was lowered further by approximately 0.1° and the measurements were repeated. The absence of any change in the measured Si coherent position indicated that the Si fluorescence from the substrate was negligible. Measurements were done on samples with 1.1 ML, 1.6 ML, 3.0 ML, and 3.4 ML of Ge coverage. The XSW measurements are shown in figure 47 and figure 48. Table 3 shows the measured values of F_C and P_C for the various samples.

If the Ge film is completely strained and pseudomorphic and the Si cap is unstrained and epitaxial then the (004) planes of the Si cap will be shifted with respect to the Si substrate (004) planes, exactly by the sum of coherent positions for the topmost and the first Ge layers. This is assuming that there are an integer number of Ge layers. The coherent positions of the cap layers based on our measured Ge coverage and our measured Ge coherent positions are also shown for comparison in table 3.

Unlike the earlier reported case of 1 ML In buried in GaAs(001) [74], these XSW cap displacement measurements for buried Ge in Si(001) are smaller than expected. Interestingly, for the samples grown with Bi as the surfactant (see table 3), $P_C^c - P_C^a = 0.06 \pm 0.01 \text{ \AA}$. This is equal to the coherent position for the first Ge atomic layer. With our limited number of measurements we cannot explain this effect. Future experiments for higher Ge coverages are required to verify its validity and to explain it.

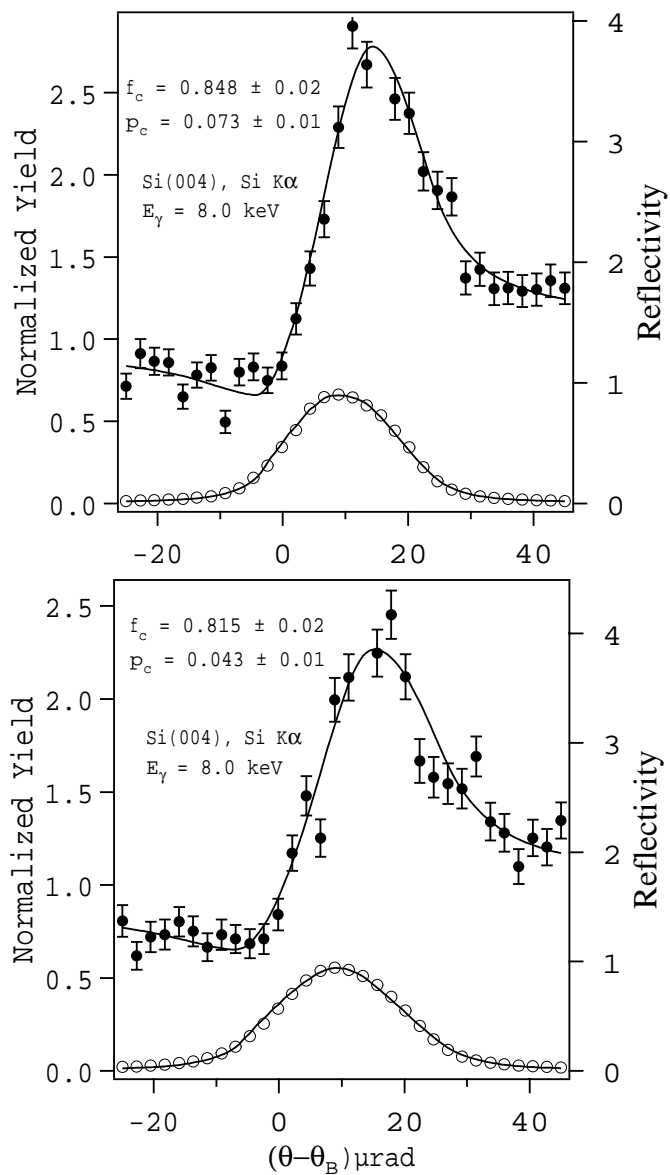


Figure 47: XSW cap measurements for 1.6 ML Ge coverage (top) and 1.1 ML Ge coverage (bottom) performed at 8.0 keV.

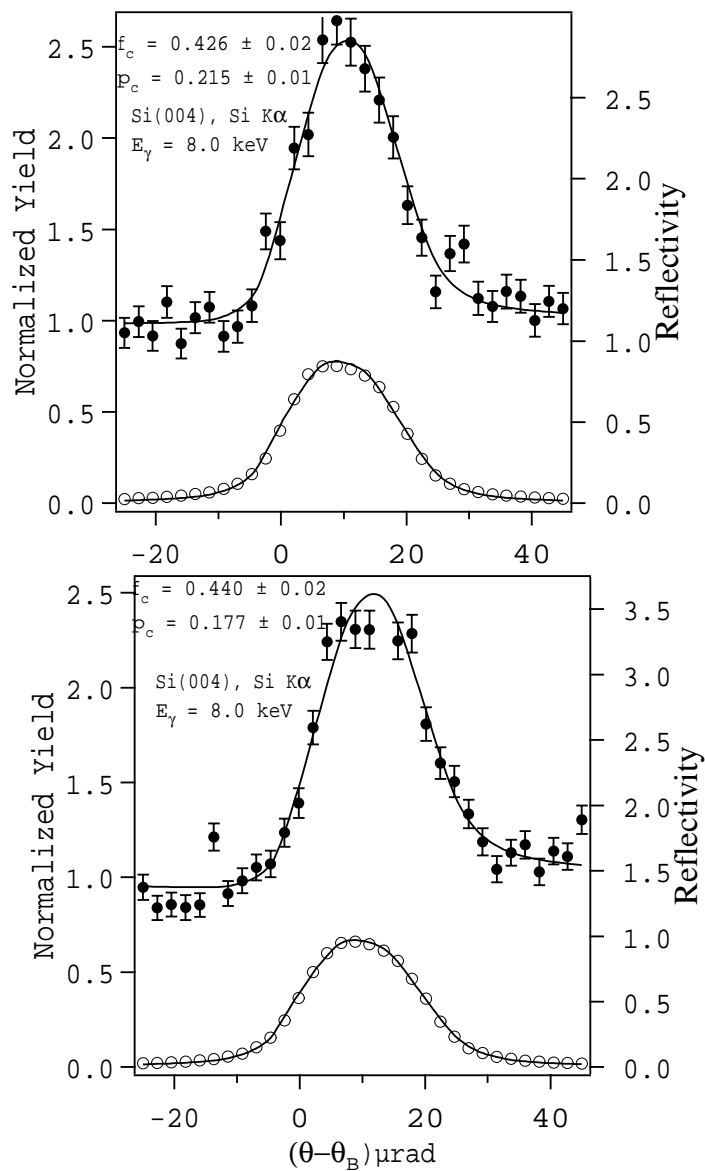


Figure 48: XSW cap measurements for 3.4 ML Ge coverage (top) and 3.0 ML Ge coverage (bottom) performed at 8.0 keV.

Coverage (ML)	Bi Surfactant?	F_C^a ± 0.02	P_C^a ± 0.01	P_C^b -	P_C^c ± 0.02
1.1	No	0.815	0.043	0.126	0.052
1.6	Yes	0.848	0.073	0.129	0.126
3.0	Yes	0.440	0.177	0.266	0.244
3.4	Yes	0.426	0.215	0.308	0.270

Table 3: Results of (004) XSW measurements for the Si cap.^a Measured values, ^b from continuum elasticity theory and ^c based on measured Ge P_{004} values.

Chapter 7

Ge Growth on Patterned Si(001)

7.1 Introduction

Recently there has been much interest in the study of self assembled semiconductor nano-dots also know as quantum dots. Although the important properties of nano-dots and their technological potential were understood for some time, the fabrication of nano-dots has been turned out to be difficult until recently. In the past lithographic techniques were employed to fabricate quantum dots. Although there have been vast improvements in fabricating nanometer-scale structures, fabrication of device-quality nanostructures is still a challenge. Growth of quantum dots by self assembly is very attractive both scientifically and technologically. The Stranski-Krastanov growth mode [6] can be used to grow nano-dots that are self-organizing and self-limiting in size [67].

7.2 Electronic properties

When the size of a solid becomes comparable to the de Broglie wavelength of charge carriers (electrons and holes), they see a confinement potential which drastically alters the electronic and optical properties of the system. The continuous spectrum of electronic density of states becomes discrete. The discrete energy levels are like from atoms and sometimes quantum dots are referred to as “artificial atoms” [75]. In solids the quantum confinement effect is observed for size in the range of 1–100 nm. Electron transition between the discrete levels produces sharp photoluminescence lines. These discrete energy levels for example can be the basis of a semiconductor laser that can achieve the luminosity and coherence of a gas vapor laser. Variations in the size and shape of the nano-dots will smear the discrete edges degrading their optical and electronic properties. Therefore a high degree of homogeneity in size, shape and strain at macroscopic length scales is essential to achieve usable performance from quantum dot devices.

7.3 Self assembled Ge island growth on Si(001)

The 4.2% lattice mismatch between Ge and Si results into Ge quickly forming 3-D islands for coverages higher than 3–4 ML. After the first reports of coherent growth of Ge islands on Si [2], this system has been extensively studied. The strain relaxation in these coherent islands is achieved by elastic deformation of the substrate. In chapter 1 we looked at the growth of Ge islands on Si(001). We will look at some of the studies done on this system [18, 83, 84].

7.3.1 Island distribution

After the early reports of Ge island formation on Si(001) [2] the evolution and distribution of size and shape of the islands recently has been extensively studied by R. S. Williams and co-workers at HP Laboratories. In their studies they report three kinds of 3D islands [83, 84]. For growth temperatures between 550 to 650°C, the 3D islands initially have {105} facets and rectangular base, with their edges along the $\langle 100 \rangle$ directions [18]. As the islands grow they become dome shaped with more facets, {113}, {102} and {518} along with {105} and {001} facets appear and the base becomes polygonal [76]. Further growth results into larger shaped domes called superdomes with presumably {111} or similar facets. Figure 49 shows the AFM image and distribution of different shapes of islands observed by Williams *et al* after depositing 13 ML of Ge onto Si(001) and annealing for 30 min at 550°C. They have reported transitions between the different island shapes as a function of substrate temperature and Ge coverage. They experimentally determined the shape diagram as shown in figure 49 as a function of Ge coverage and temperature.

Kästner *et al* found that at lower temperature (300°C) and coverages only 1-2 ML beyond the wetting layer kinematic limitations prevent formation of larger islands and smaller islands with only {105} facets are formed [79]. Although they pointed out that such a kinetic limitation should favor a narrow island distribution they observed continuous nucleation of new islands [79]. The island distribution also depends on annealing times. At lower temperatures and longer annealing times, the islands evolve to a relatively stable, steady-state distribution while at higher temperatures alloying of Ge and Si determines the island shape [77]. Alloying decreases the misfit between the islands and the substrate and larger islands appear. It also delays the onset of dislocations in the islands [78].

The size distribution of the islands is still not very well understood and currently two different views exist. One model views the island size and distribution is based on kinetic process of Oswald ripening [80, 81, 82]. Real time TEM by Ross *et al* during Ge growth on Si(001) by chemical vapor deposition at 650°C shows that island size changes continuously over time [81]. Another model considers the islands to be in thermodynamic equilibrium with each other [83]. Thus according to the second model pyramids and domes correspond to two energetically stable island configurations of strained coherent islands. The observations of Ross *et al* are not consistent with the second model. The inconsistency could be due to Ge islands being metastable with respect to alloying with the substrate [76]. Alloying decreases the misfit and increases the critical island size. In addition even at constant temperature alloying may vary with deposition time. Apart from growth temperature and time alloying seems to depend on the strain energy [78]. Domes have higher strain energy densities and alloy at lower temperatures than pyramids [78]. On annealing at 650°C domes have been observed to transform reversibly into pyramids of larger size due to alloying [84].

The composition and thickness of the Ge wetting layer is also not well understood at higher temperatures. If the wetting layer is metastable then during annealing the islands can grow from migration of Ge atoms from the wetting layer into the islands [77]. As with pyramids and domes the wetting layer is also expected to undergo alloying and its critical thickness should presumably increase as well. If this is correct then the alloying of the Ge wetting layer should occur first as it has the largest strain energy density.

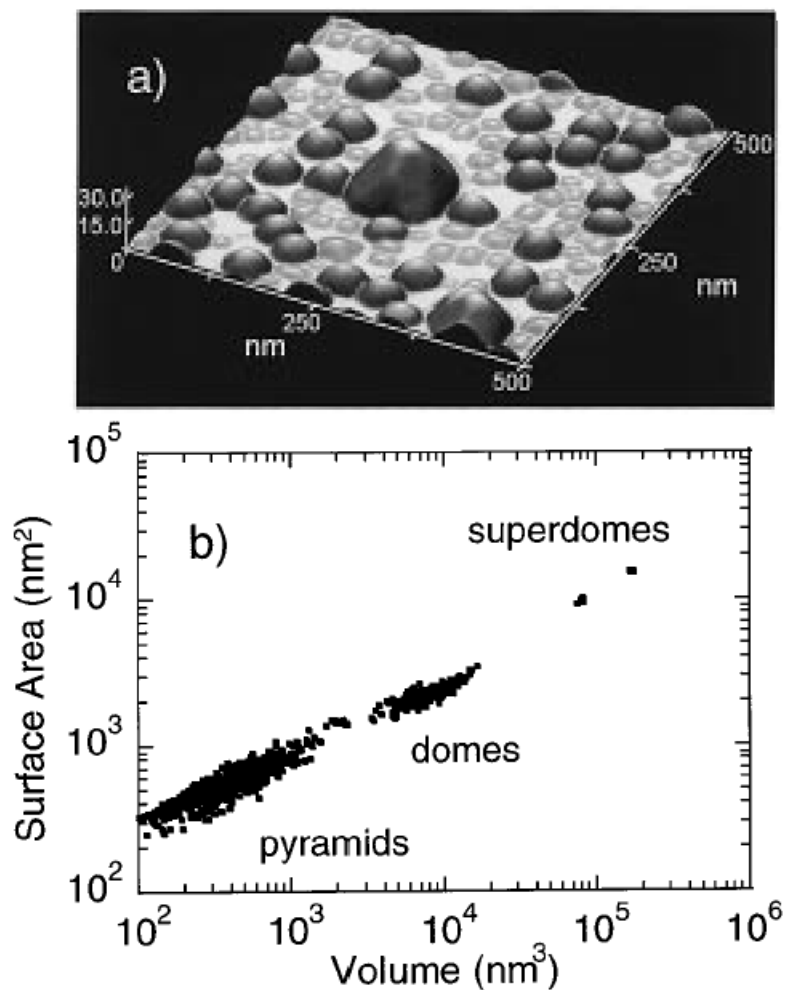


Figure 49: After Williams *et al* [76] (a) Atomic force microscope topograph of a 13 eq-ML film of Ge deposited onto Si(001) and annealed for 30 min at 550°C. The gray scale is keyed to the local facet angle with respect to the substrate plane, with darker shades corresponding to steeper angles. Pyramids, domes and superdomes are readily recognized by both their size and shading. (b) scatter plot showing the exposed surface area of the islands versus their volumes on a $1 \mu\text{m}^2$ area for the same sample as in part a. Each island shape forms a family of points on the graph, allowing the members of each family to be identified for statistical analysis.

7.3.2 Lateral ordering

The islands interact with each other through the substrate [85]. TEM studies have shown that the islands generate significant strain fields around them in the substrate [2, 86]. These strain fields cause the islands to repel each other [87]. LeGoues *et al* have reported real time observation of small islands repelled by larger islands as the boundaries of their base approach each other [88]. Elastic interaction between the islands can make them stable against transformation to larger islands or domes [89]. Thus strain due to lattice mismatch can lead to narrower distribution of islands with uniform island–island spacing. This strain field interaction can also lead to short–range ordering of the islands on the substrate [90]. Such lateral ordering is observed for $\text{Si}_{1-x}\text{Ge}_x/\text{Si}(001)$ at low values of x ($x = 5 - 15\%$) by Dorsch *et al* [91]. Due to the low misfit they observed ripples which self–organize along the (100) directions. On further growth they saw the ripples transform into coherent islands. The base of the islands was determined by the initial ripple pattern. They measured the wavelength of the periodic separation of islands to be $6.5\ \mu\text{m}$ at 5% Ge content to $1.1\ \mu\text{m}$ at 15% Ge content.

Schmidbauer *et al* [90] have investigated the ordering of self–assembled $\text{Si}_{1-x}\text{Ge}_x$ islands by grazing incidence small–angle x–ray scattering and AFM. They saw superstructure satellite peaks along the (100) directions in the power spectrum of AFM images indicative of lateral ordering of islands (see figure 50 a). They also observed satellite peaks along the $\langle 100 \rangle$ and $\langle 110 \rangle$ directions in their GISAXS scans (see figure 50 b). They found increase in ordering as the island density increased. Due to larger misfit for pure Ge the lateral ordering is short range.

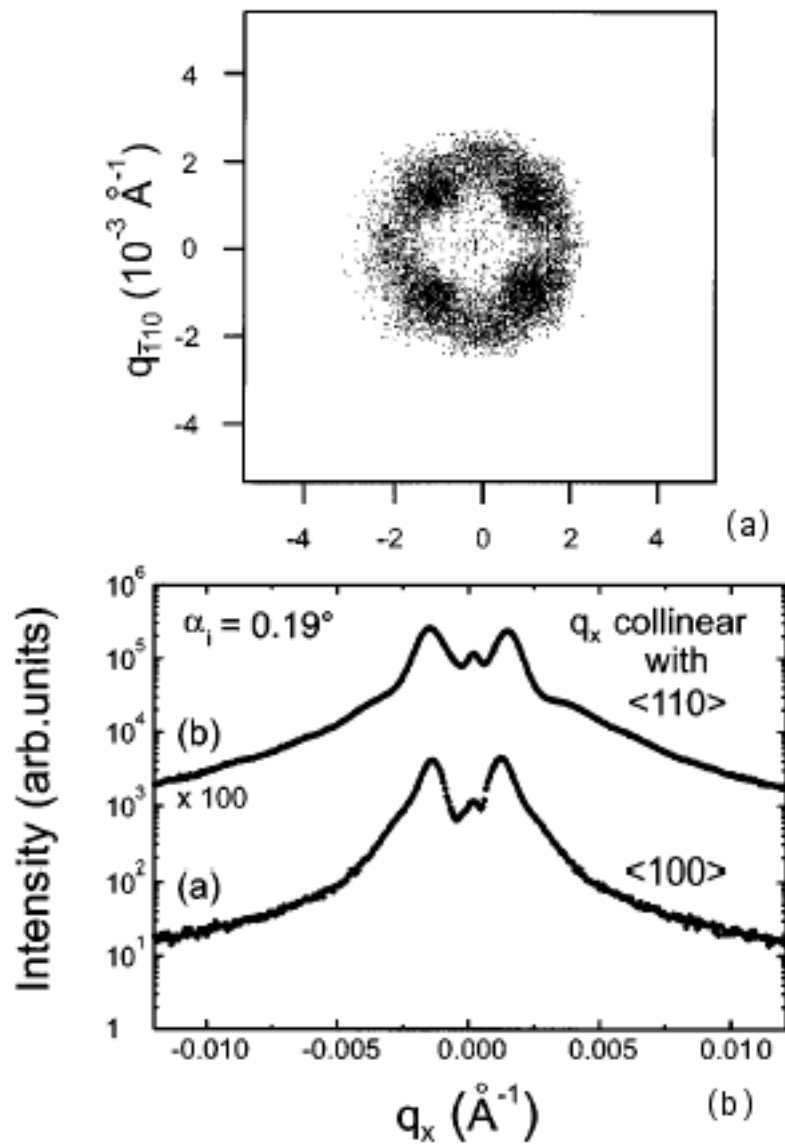


Figure 50: Schmidbauer *et al* [90], (a) Power spectrum of AFM micrograph and (b) GISAXS intensity profile along $\langle 100 \rangle$ and $\langle 110 \rangle$ for $\text{Si}_{1-x}\text{Ge}_x$ ($x = 0.25$) islands on $\text{Si}(001)$.

7.3.3 Vertical ordering

In heteroepitaxial systems with larger misfits island formation on the surface is favored where the the strain at the surface reduces the mismatch between the island and the surface [64]. Alternating growth of islands and substrate material, the islands in successive layers become spatially correlated [92]. Tersoff *et al* [64], gave a generic model based on continuum elasticity theory to explain the correlation between islands in successive layers. They modeled the surface strain ϵ at lateral position x from an island buried at a depth L and $x = 0$ to be

$$\epsilon(x) = C(x^2 + L^2)^{-3/2}[1 - 3L^2/(x^2 + L^2)] \quad (39)$$

Where C takes into consideration the volume of the island, the misfit and the elastic constants. Their model correctly explained the increase in uniformity of the island size and spacing for successive layers. They grew $\text{Si}_{0.25}\text{Ge}_{0.75}/\text{Si}$ superlattices and found that the islands became more regular and uniformly spaced after 20 layers compared to first layer (see figure 51). Some variation in size and shape and spacing is still evident in their AFM images. It is not clear if the model is valid for large number of layers as it assumes the surface to be isotropic (only x as independent variable).

7.4 Growth of Ge on patterned Si(001)

Randomly distributed islands of uniform size and shape may be adequate for optical applications of quantum dots, but for electronic applications precise control over positioning of these islands is required. Although as discussed in section 7.3.3 superlattice structures of islands can be used to position islands on the surface,

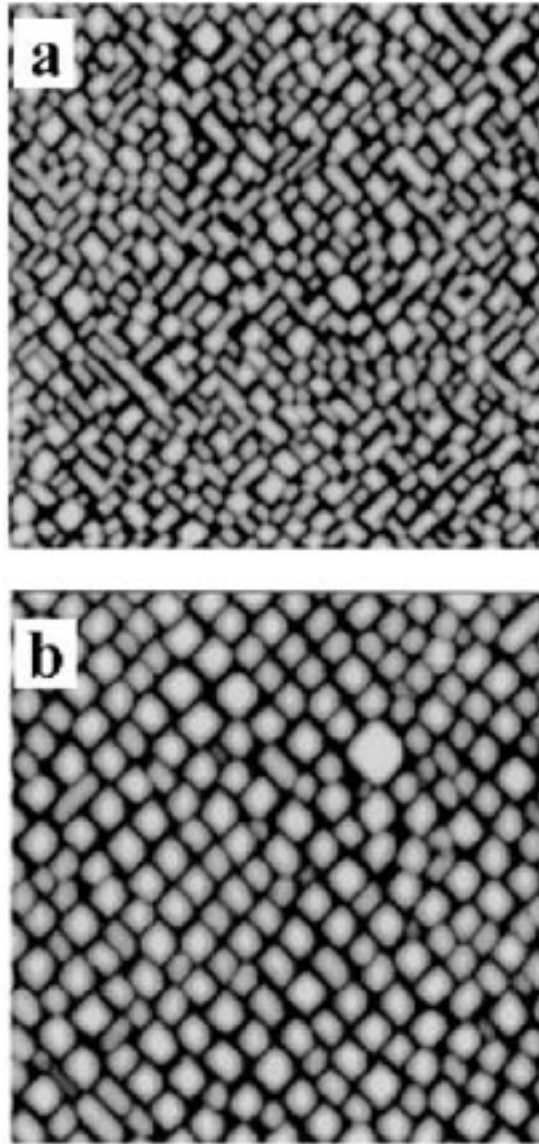


Figure 51: Tersoff *et al* [64], AFM images of $\text{Si}_{0.25}\text{Ge}_{0.75}/\text{Si}$ superlattices. Scanning direction is $[110]$. (a) $0.8\ \mu\text{m} \times 0.8\ \mu\text{m}$ image after deposition of the first alloy layer;(b) $1.25\ \mu\text{m} \times 1.25\ \mu\text{m}$ image after deposition of the 20th alloy layer.

there is still no control over the period and many layers are required to get islands with good uniformity. Such a process is not economical and poses innumerable problems for integrating devices.

A combination of lithography and SK growth mode has been shown to achieve improved control in positioning the islands and making them more uniform [93, 94, 95, 96]. The key idea in the work by Kamins *et al* and later by Jin *et al* is to control coarse positioning of islands by conventional lithography and then use misfit strain to fine tune the position, size and shape of the islands. On an infinite surface the Ge islands are coupled to each other through their diffusion on the surface [97] and the strain fields they generate in the substrate. The diffusion lengths for Ge on Si(001) are quite large at higher temperatures. Strain fields on the other hand are localized near the islands. Therefore diffusion coupling between islands tend to be long range compared to strain coupling. Isolating the island nucleation site by putting barriers to diffusion or modifying it to some degree can lead to dramatic change in the way the islands grow. One such barrier to diffusion is to make the surface dimensions comparable to the diffusion lengths. Patterned surfaces either by selective area growth or etching can isolate nucleation of islands from each other.

Patterning of substrates has been shown to effect the growth of Ge on Si(001). At higher growth temperatures ($> 600^{\circ}\text{C}$) Ge diffuses readily on Ge surface and presumably nucleates along the edges. This nucleation takes place due to the diffusion barrier presented by the edge and is affected by the vicinal surface. Any defects such as dislocations at the edges also results in nucleation. The edge thus offers a site for formation of Ge islands on Si. Along the edge the Ge dots can arrange themselves in a periodic manner due to island–island interaction through strain fields produced by the islands in the substrate. There exist as a function of

growth conditions a distribution of the size of the islands and the island to island separation.

7.4.1 Growth on stripe–mesas

Kamins *et al* [93, 94] investigated the growth of Ge islands on Si stripe–mesas. The Si stripe mesas were formed by selective area growth by chemical vapor deposition. Ge islands were then deposited also by CVD at 600°C. The Si lines on their samples were oriented along the $\langle 100 \rangle$ and $\langle 110 \rangle$ directions and had widths ranging from 450 nm to 10 μm . They observed ordering of Ge islands near the edges of the Si(001) stripe–mesas (see figure 52). For higher coverages the additional rows of Ge islands appeared away from the edges but with decreasing order. The islands were about 75 nm in size. When the Si surface was a narrow ridge they observed only one row of Ge islands. They saw better ordering on $\langle 100 \rangle$ –directed lines than on $\langle 110 \rangle$ lines. It is not clear what was the shape of the islands as they did not show any high resolution images of individual islands. From their images the islands looked dome shaped rather than pyramidal. Jin *et al* [96] observed similar ordering of Ge islands.

The ordering of Ge islands on patterned surfaces could be because of several factors. Kamins *et al* suggested easy nucleation of Ge atoms at atomic steps on the shallow facets of Si stripe–mesas close to the edges. Reflection of Ge atoms from the edges perhaps increases the concentration of Ge adatoms near the edges with the consequent higher probability of nucleation [93]. It is also possible that close to the edges the defect density is higher which in turn leads to greater nucleation of Ge islands. The easier deformation of the Si lattice near the edges also can explain favorable Ge nucleation. No Ge islands were observed in the center of the islands mainly due to strong Ge diffusion. The island spacing along the edges is

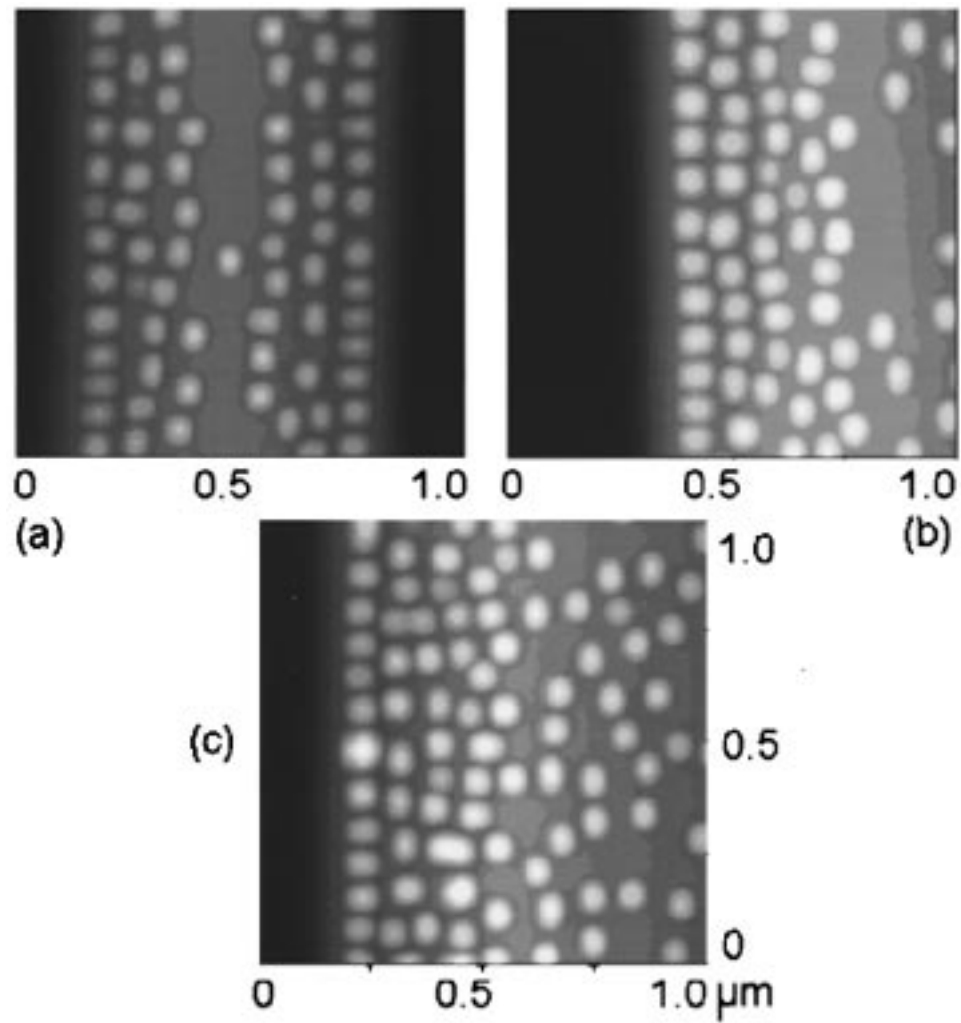


Figure 52: Kamins *et al* [93], AFM images of Ge islands grown on Si stripe-mesas showing ordering of several rows of Ge islands near the edges of the flat Si(001) surface. Widths of Si(001) surface: (a) 670 nm, (b) 1.0 μm, (c) 1.7 μm .

very uniform for the first row mainly due to strain driven self-assembly.

7.4.2 Growth on square-mesas

Growth of Ge islands on square-mesas in principle is similar to that on Si stripe-mesas except now the diffusion of Ge atoms is limited in both x and y directions. Jin *et al* [96] have studied the growth of Ge islands on Si square-mesas. At lower coverage they found four islands formed at the corners of the square-mesa (see figure 53). At sufficient coverage an additional fifth island was formed in the central region. They report the central island to be pyramidal as opposed to dome shaped outer islands.

7.5 *In situ* LEED Studies

We performed *in situ* low energy electron diffraction studies of Ge island growth by MBE on planar Si(001) surface. The samples were prepared in our UHV-MBE chamber. The preparation of growth surface and the MBE growth is explained in chapter 4. Two different studies were performed: one as function of Ge coverage at fixed growth temperature of 650°C and other at fixed Ge coverage of 10 ML. In each case the LEED was performed at room temperature.

7.5.1 Coverage dependence

The coherent Ge islands have faceted surfaces. The islands are believed to be on top of a Ge wetting layer 3–4 ML thick. The transition from 2D to 3D growth as the Ge coverage is increased will change the surface reconstruction. During the 2D growth the normal 2-domain $2 \times n$ reconstruction is expected [98]. When 3D growth begins the tilted surfaces of the islands will produce additional patterns in

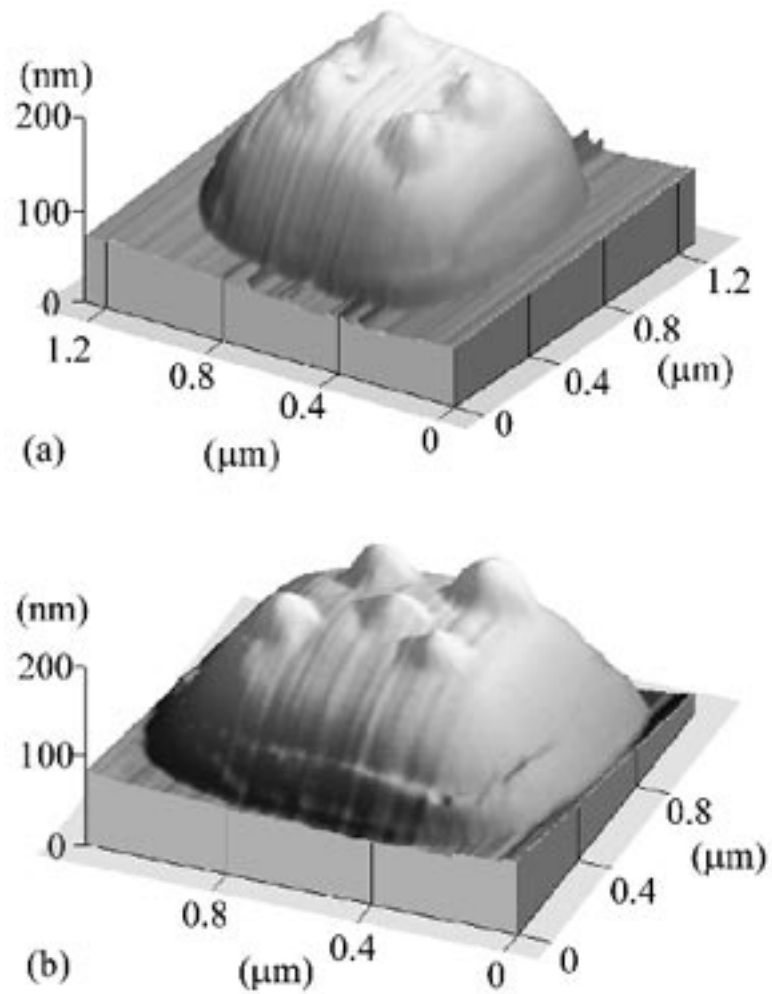


Figure 53: Jin *et al* [96], (a) A 3D AFM image with four Ge islands located at the corners on square mesa with the base lines parallel to the $\langle 110 \rangle$ directions. The Ge thickness is 9 ML. (b) A 3D AFM image with five Ge islands with 10 ML Ge. The fifth pyramidal island is formed in the central region.

the LEED image. Figures 54 and 55 show the LEED images taken after different coverages of Ge deposited at 640°C.

After about 3 ML of Ge is deposited a $2 \times n$ reconstruction was seen with $n \sim 7$. At this coverage the Ge growth is still 2D but the usual 2×1 reconstruction changes to $2 \times n$ to reduce the number of dangling bonds as originally proposed by Pandey [99]. At 5 ML additional spots appear in the diffraction pattern. These peaks have 4-fold symmetry and are collinear with the $\langle 11 \rangle$ directions which is same as the $\langle 100 \rangle$ directions of the Si lattice. Additionally energy scans of the LEED showed that these spots moved with respect to the 2×1 LEED pattern. This indicated that the additional peaks were from the faceted surfaces intersecting the (001) surface along the $\langle 100 \rangle$ directions. Our LEED observations and analysis agree with the $\{105\}$ faceting of Ge islands on Si(001) reported in literature. At 12 ML the Ge island density is higher and therefore the peaks from the faceted surfaces become more intense.

7.5.2 Temperature dependence

The annealing studies were performed for 10 ML of Ge deposited at room temperature. The sample temperature was then ramped at 1°C/s, held at a given temperature for 10 min and then cooled down naturally to room temperature. LEED was then performed. Figure 56 shows the LEED images taken after annealing the sample at different temperatures. In figure 56a the LEED is that of clean Si(001) reconstruction. At room temperature the Ge is mostly amorphous and therefore no LEED pattern was observed. As the temperature was raised the Ge started to become more crystalline and diffraction spots began to appear in the LEED image. At about 525°C (figure 56b) a faint 2×1 reconstruction appeared probably from the wetting layer. The presence of high LEED background and no

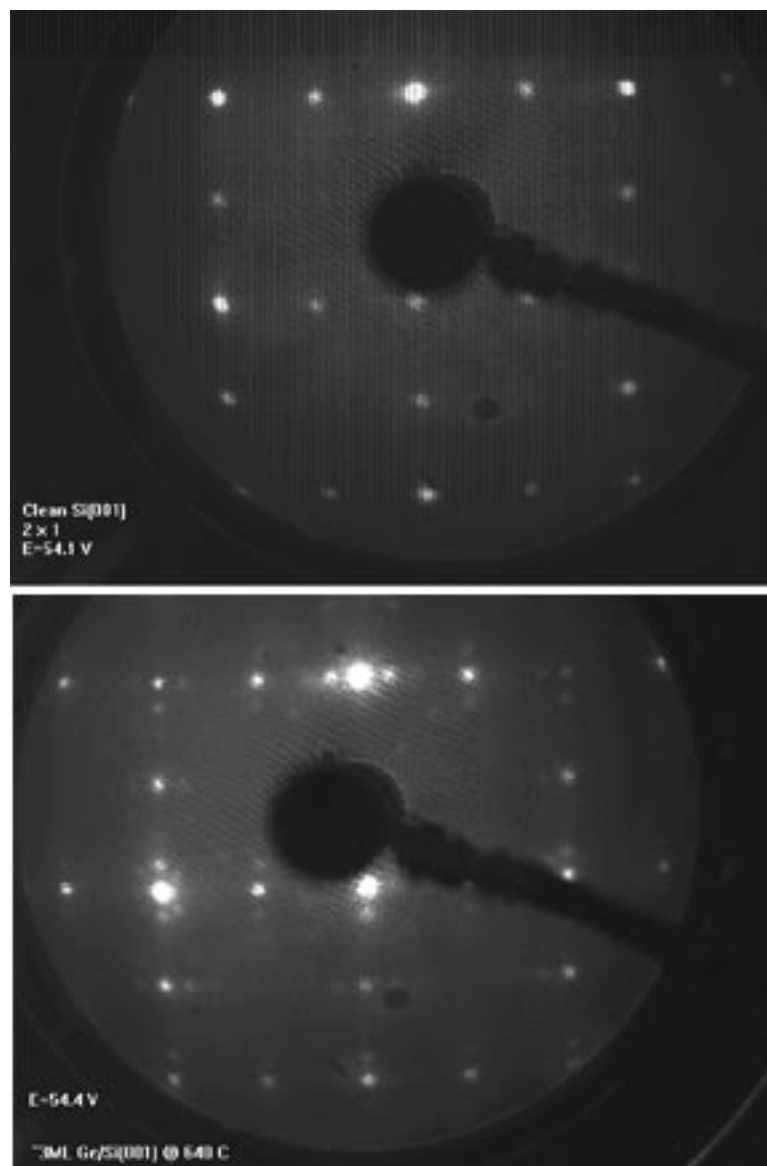


Figure 54: LEED images after various coverages of Ge. (a) clean Si surface, 2-domain 2×1 reconstruction, (b) after 3 ML of Ge $2 \times n$ reconstruction; cont'd. in figure 55.

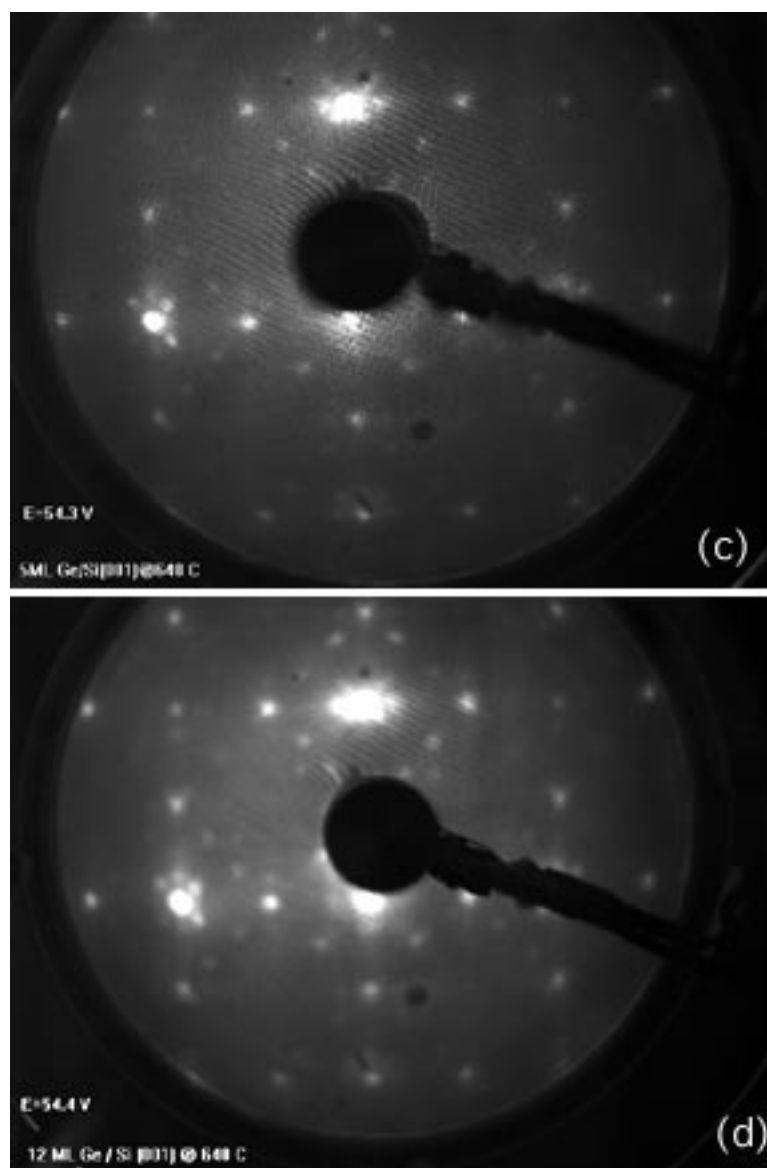


Figure 55: LEED images after various coverages of Ge, cont'd. from figure 54 (c) after 5 ML of Ge additional spots with 4-fold symmetry due to the faceted surfaces on the islands appear, (d) after 12 ML of Ge the reconstruction is similar to (c) with higher intensity in the spots from faceted surfaces.

additional peaks other than the 2×1 pattern in figure b indicates that on the surface significant amount of Ge remained amorphous and no islands were formed. After annealing at 623°C islands were formed as seen from the LEED pattern in figure 56c. This is in agreement with our observation in previous section.

The LEED pattern then remained stable up to around 775°C when the diffraction peaks from the islands began to disappear. At this temperature the diffusion of Si from the substrate in the Ge is very high resulting in alloying. The thickness of the wetting layer increases exponentially as the Si content in the SiGe alloy increases. Therefore at higher temperatures the Ge islands are absorbed to form a energetically more favorable thicker wetting layer. This can explain why the diffraction spots from the islands disappeared in figure 56c. At 852°C only the wetting layer is present and the LEED pattern was $2 \times n$ again consistent with our observation for pure Ge wetting layer. After annealing at 900°C the LEED pattern was pure 2×1 as the Ge layer had completely and irreversibly absorbed into the Si substrate (figure 56f). Using the diffraction spots we calculated the lattice constant of the alloy to be 3% larger than the Si lattice constant. Using Vegard's law we estimated the alloy composition after annealing at 900°C to be $\text{Si}_{0.3}\text{Ge}_{0.7}$.

7.6 Morphology Studies

We studied the morphology of Ge grown on Si (001) surface patterned into stripe-mesas. The surface was patterned into stripe-mesas using e-beam lithography and reactive-ion etching as explained in chapter 4. The stripe-mesas were $160 \mu\text{m}$ long, about $0.6 \mu\text{m}$ wide and $0.2 - 0.3 \mu\text{m}$ tall. The separation between two neighboring stripe-mesas was $1.0 \mu\text{m}$. Figure 57 shows the AFM image after RIE etching. The

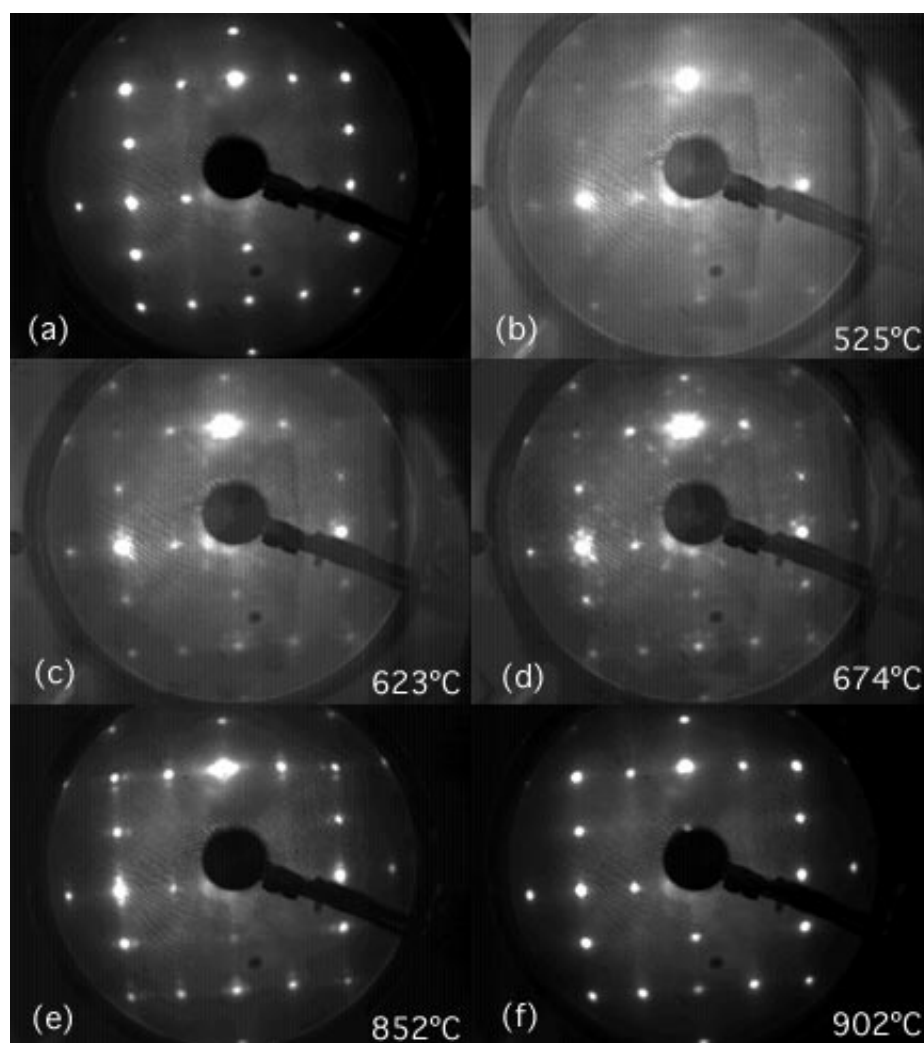


Figure 56: (a) LEED image of clean Si(001) surface. (b)–(f) LEED images after annealing the the sample at temperatures indicated. The Ge coverage was fixed at 10 ML. All the LEED images were taken at RT.

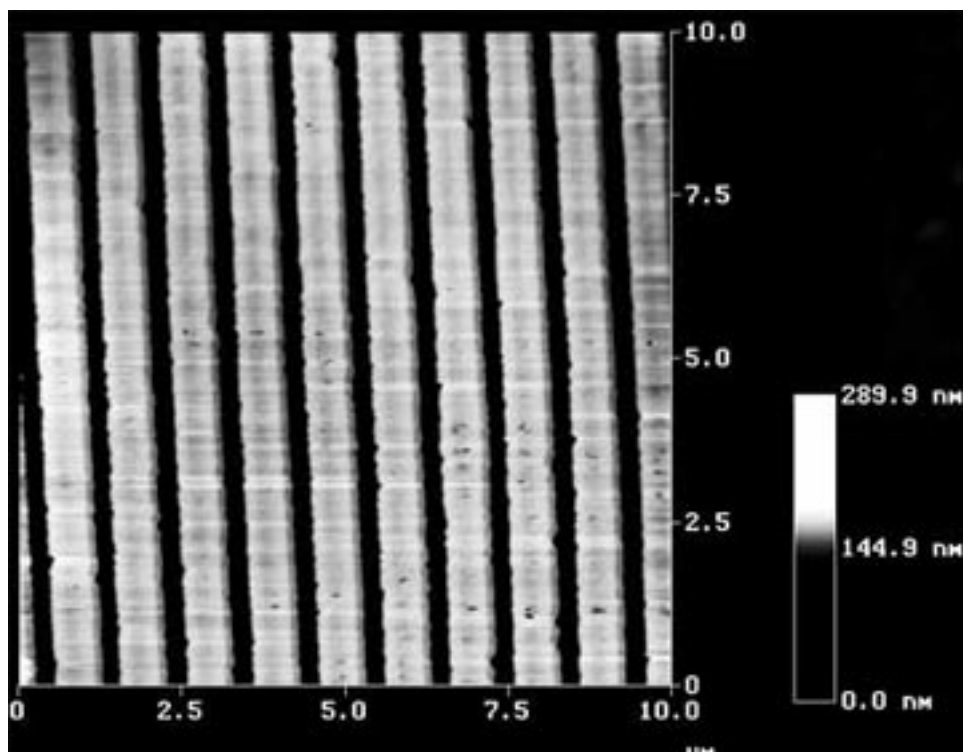


Figure 57: AFM micrograph of Si surface patterned into a column of stripe-mesas by e-beam lithography and RIE.

total patterned surface was only $160 \times 160 \mu\text{m}^2$. As seen the edges of the lines are not very sharp due to the limitations of the e-beam writer. The lines were patterned along $\langle 100 \rangle$ and $\langle 110 \rangle$ directions. The Ge was grown in our MBE chamber at 640° . The surface preparation and Ge growth is explained in chapter 4. Approximately 8–12 ML of Ge was deposited. Ge was also deposited on unpatterned Si to compare the results. The coverage was estimated by timing the deposition. All the samples were imaged by AFM *ex situ* at the Materials Research Center.

Figure 58 shows the AFM micrograph of the surface after depositing approximately 15 ML of Ge. The scan area is $5 \times 5 \mu\text{m}^2$. A distribution of islands is clearly visible. The largest islands are about 400 nm in size with square base with

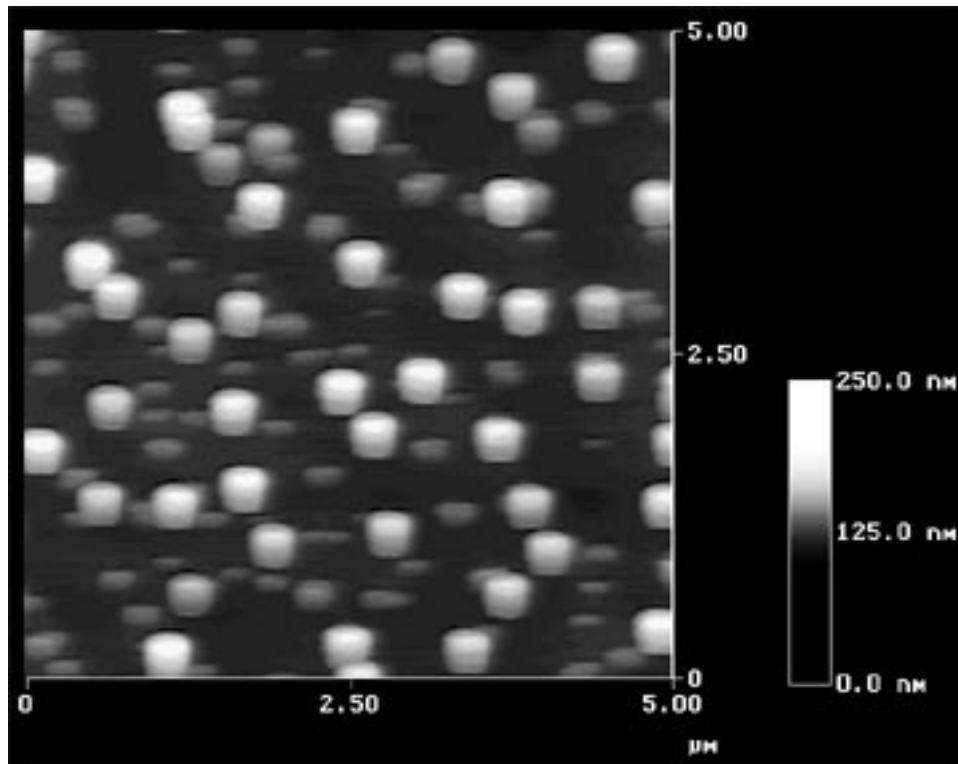


Figure 58: AFM micrograph of Ge islands on unpatterned Si(001) surface. The Ge coverage is about 15 ML.

sides along the $\langle 100 \rangle$ directions. The smallest islands are about $100 \times 200 \text{ nm}^2$.

The AFM micrograph of a patterned surface after depositing approximately 10 ML of Ge is shown in figure 59. Compared to figure 57 the stripe-mesas have almost disappeared. The surface has three distinct features: (a) pits (b) plateaus and (c) islands. The pits are the regions from where Si was etched during RIE. The *in situ* sample annealing at 900°C to prepare a clean surface prior to Ge deposition modified the patterned surface considerably. At 900°C the native oxide layer is desorbed. Depending on the oxide thickness which can be nonuniform because of the lithography and etching the final clean surface will be different from the original surface. In addition at 900°C Si diffusion on the surface is also significant.

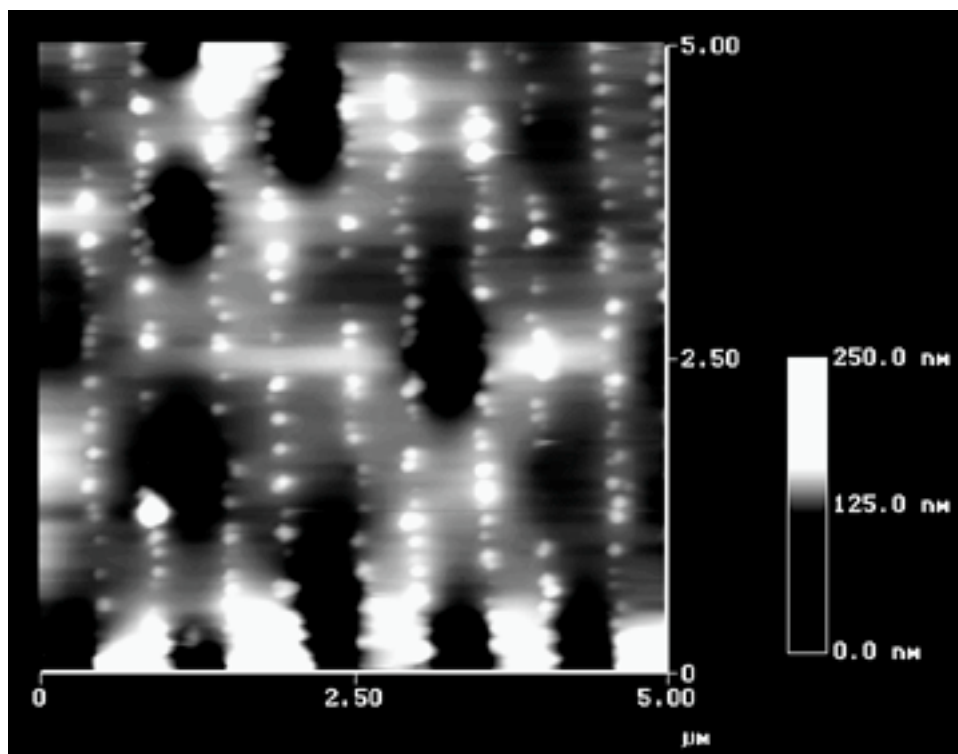


Figure 59: AFM micrograph of Ge islands on patterned Si(001) surface. The island rows are along $\langle 110 \rangle$ direction. The Ge coverage is about 10 ML.

Annealing at temperatures lower than 900°C did not completely remove carbon and oxygen contamination from the surface necessary to grow Ge. The above two factor we think were responsible for the flattening of the surface.

Even after the surface is modified the edges of the stripe-mesas were preserved as evidenced from the aligning of the Ge islands. The islands clearly appear to have grown along a line in one direction presumably the edge of the strip-mesas. The separation between the lines of these islands is approximately same as the width of the stripe-mesas. Compared to Ge grown on planar surface the Ge islands on the patterned surface have a much narrower distribution in size and shape. Also the island size is smaller and the shape of all islands is same.

Figure 60 shows a high resolution AFM micrograph of the islands. The island rows are along $\langle 110 \rangle$ directions. The islands approximately have a square base and also appear to be faceted. As marked in the figure there are two rows of islands. The first row on the left side has islands spaced uniformly along the edge and they are all of the same size. The average spacing between the islands is about 100 nm and the size of the island is about 60 nm. A second row with relatively bigger islands is also seen. The spacing between the islands in the second row is not uniform. This is consistent with observations of Kamins *et al* [93]. The uniform spacing between the islands in the first row is indicative of the fact that along the edges the islands interact with each other presumably through strain fields generated in the substrates and self-assemble. The presence of an edge increases the probability of nucleation [93] along it. After the first row is formed the islands grow to their maximum size and second row begins to nucleate. The second row is not as uniform because of the absence of any edge in the immediate vicinity. The Ge atoms diffusing from the center get scattered by the first row of Ge islands. Unlike the straight edge scattering from islands is probably less ordered consequently forming a less ordered second row of islands. Following the same reasoning the relatively less uniform first row on the right hand side of the stripe-mesa in figure is due to an edge that is not straight. As the edge is not visible in the AFM micrograph the above explanation cannot be verified. Compared to the first row the nucleation of islands in the second row is shifted. The islands in the second row are formed next to the gaps between the islands in first row. No Ge islands are formed in the center due to lower nucleation probability.

The region between the stripe-mesas is also island free. This is little bit surprising as that region is expected to have large nucleation sites due to etching. But due to annealing at 900°C the defect density probably is reduced considerably.

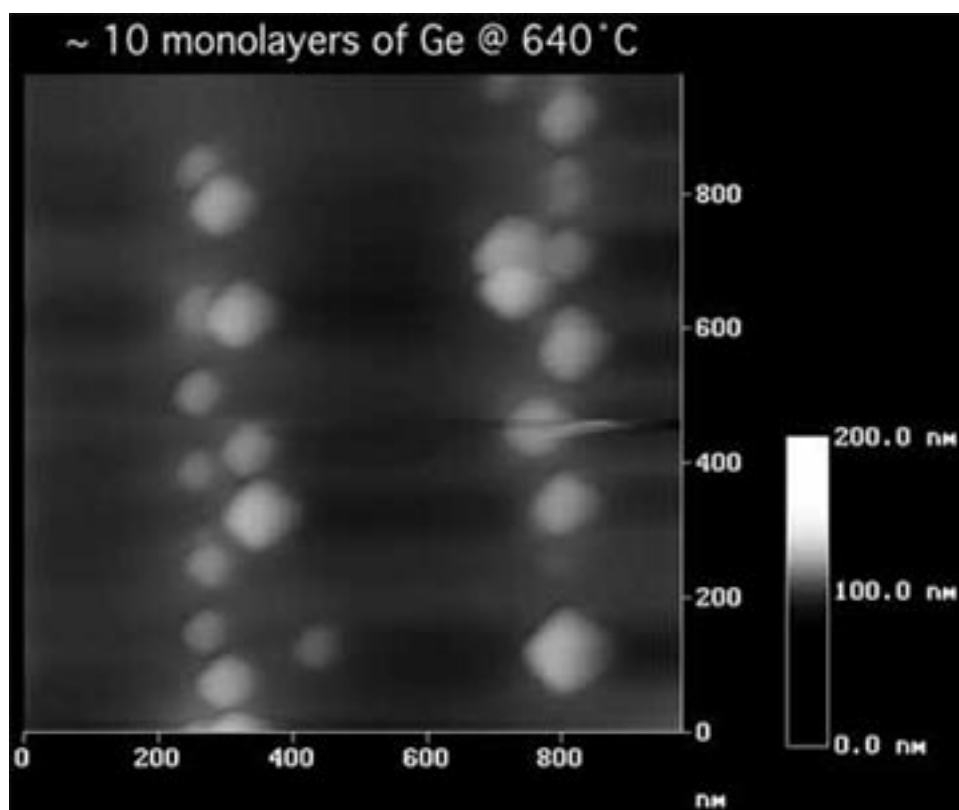


Figure 60: High resolution AFM micrograph of Ge islands on patterned Si(001). The edges are along $\langle 110 \rangle$ direction. The Ge coverage is about 10 ML.

Also due to etching this region has large roughness $\sim 10\text{nm}$ possibly retarding the Ge surface diffusion [95]. The lack of sufficient diffusion may have prevented Ge island formation.

Chapter 8

Summary

8.1 Thesis Summary

In this thesis we studied the epitaxial growth of Si/Ge heterostructures on Si(001) surface with Bi as a surfactant with x-ray standing wave technique, grazing incidence x-ray diffraction and x-ray specular reflectivity using synchrotron radiation. We also initiated a study to understand the growth mechanism of Ge nano-dot structures on patterned Si(001) by MBE.

Traditionally XSW technique has been mainly used for studying surfaces. We demonstrated how XSW technique can be used to do structural studies of films of several atomic layers. We investigated the layer by layer growth of Ge on Si(001) in the presence of Bi as a surfactant by performing Si(004) and Si(022) XSW measurements. By comparing approximately 1 ML Ge growth with and without Bi we showed that Bi prevents segregation of Ge in Si. Under the assumption of layer by layer growth and continuum elasticity theory, our measured coverage for Ge agreed with our measured coherent positions for (022) reflection up to 10 ML of Ge coverage and for (004) reflection up to 7 ML of Ge coverage. The coherent fractions were considerably lower than expected. We showed that the reduction in

coherent fraction can be explained by a static Debye–Waller factor. The simplest interpretation of our XSW data is that each Ge atom is likely to have a static displacement about its expected position. For this static displacement field we assumed a Gaussian distribution centered about the expected Ge atomic position. We further extended this model by a semi ad–hoc assumption that the static deviation increases linearly with the Ge atomic layer distance from the Si substrate. The partial physical basis for this assumption is that as the Ge layer distance increases it becomes more and more relaxed. Using this model we explained the reduction in coherent fraction. One important result is that the width of this displacement distribution in the $[022]$ direction is smaller than in the $[004]$ direction. Our conclusion is that the Ge atoms are more deviated in the normal direction to the surface than in the direction in the plane of the surface.

Using GIXD we found that with Bi as a surfactant the critical thickness for pseudomorphic growth for Ge was increased to 7 ML. Even at 10 ML of Ge growth no island formation was observed but the Ge layer was partially relaxed. In the case when Bi was not used we clearly showed that the Ge was relaxed and a SiGe alloy was formed due to the segregation of Ge into Si cap layer. Using x–ray reflectivity we showed that the film roughness increases dramatically as the Ge layer thickness increased from 7 ML to 10 ML. These measurements are consistent with our XSW measurements.

We also studied the self assembly of Ge nano–dots on Si stripe–mesas by atomic force microscopy. The goal here was to arrange the Ge nano–dots of identical size and shape in a periodic array by combination of strain field interaction between the islands and coarse–scale lithography. We showed that compared to growth on planar surfaces the Ge dots are of approximately uniform shape and size and aligned along the edges of the stripes.

8.2 Future Work

The XSW structural analysis I discussed is model dependent because of the limited number of measurements I was able to perform. XSW is very unique because it does not suffer from the well known phase problem. Temperature dependent and higher order (e.g. similar to (008) we performed) XSW measurements can be performed to get more accurate and direct picture of Ge/Si(001) and other similar systems. Due to the Ge segregation in the Si cap I was not able to do a similar study for the Ge grown without surfactant. Also depth dependent XSW measurements can be performed by monitoring the photoelectron yield. All these experiments would require a UHV environment which we now have available at the 5ID-C undulator beamline of the APS. These experiments can be performed for other surfactants like Te and Sb as well.

The growth of nano-dots is very interesting and very little is known about their growth on patterned surfaces. Surfactants like Sn under certain conditions promote island growth and therefore may also be used to grow such structures. To this date there is no such study reported. All of my AFM studies were performed *ex situ* and therefore surfaces of the nano-dots could not be studied at atomic resolution. Currently we are in the process of combining our UHV-MBE system with a UHV-STM/AFM system. *In situ* STM/AFM studies should give more clearer and deeper picture of the growth of such nano-dots. With future improvements in x-ray micro-focusing and micro-diffraction techniques it would be possible to study the strain in individual nano-dots [100]. These studies can be extended to magnetic nano-dots as well. The current availability of high brilliance synchrotron sources for x-ray and even more intense fourth generation source that are proposed now would make the study of magnetic nano-dots by x-rays possible.

References

- [1] M. Copel, M. C. Reuter, E. Kaxiras, and R. M. Tromp, Phys. Rev. Lett., **63**, 632 (1989).
- [2] D. J. Eaglesham and M. Cerullo Phys. Rev. Lett., **64**, 1943 (1990).
- [3] E. Bauer, Z. Kristallogr. **110**, 372 (1958).
- [4] F. C. Frank and J. H. van der Merwe, Proc. Roy. Soc. London A **198**, 205 (1949).
- [5] M. Volmer and A. Weber, Z. Phys. Chem. **119**, 277 (1926).
- [6] I. N. Stranski and Von L. Krastanow, Akad. Wiss. Wien. **146**, 797 (1938).
- [7] E. Bauer and J. H. van der Merwe, Phys. Rev. B **33**, 3657 (1986).
- [8] E. Tourine and K. H. Ploog, Thin Solid Films, **42**, 43 (1993).
- [9] T. Narusawa and W. M. Gibson, Phys. Rev. Lett. **47**, 1459 (1981).
- [10] M. Asai, H. Ueba, and C. Tatsuyama, J. Appl. Phys. **58**, 2577 (1985)
- [11] P. C. Kelires and J. Tersoff, Phys. Rev. Lett. **63**, 1164 (1989).
- [12] J. W. Matthews J. Vac. Sci. Technol. **12**, 126 (1975).
- [13] J. Tersoff, Phys. Rev. B **43**, 9377 (1991).
- [14] L. N. Aleksandrov, R. N. Lovyagin, O. P. Pchelyakov, and S. I. Stenin, J. Cryst. Growth **24/25**, 298 (1974).
- [15] H. -J. Gossman, L. C. Feldman, and W. M. Gibson, Surf. Sci. **155**, 413 (1985).

- [16] K. Miki, K. Sakamoto, and T. Sakamoto, in *Chemistry and Defects in Semiconductor Heterostructures* edited by M. Kawabe, e. R. Weber, and R. S. Williams, MRS Proc. Symp. D (1989).
- [17] A. A. Williams, J. M.C. Thornton, J. E. Macdonald, R. G. van Silfhout, J. F. van der Veen, M. S. Finney, A. D. Johnson, and C. Norris Phys. Rev. B, **43**, 5001 (1991).
- [18] Y. -W. Mo, D. E. Savage, B. S. Swartzentruber, and M. G. Lagally Phys. Rev. Lett., **65**, 1020 (1990).
- [19] A. J. Steinfort, P. M. L. O. Scholte, A. Ettema, M. Nielsen, E. Landemark, D. -M. Smigies, R. Feidenhans'l, G. Falkenberg, L. Seehofer, and R. L. Johnson Phys. Rev. Lett., **77**, 2009 (1996).
- [20] G. Medeiros-Ribeiro, T. I. Kamins, D. A. A. Ohlberg, and R. S. Williams, Phys. Rev. B, **58**, 3533 (1998).
- [21] K. Sakamoto, T. Sakamoto, S. Nagao, G. Hashiguchi, K. Kuniyoshi, and Y. Bando, Jpn. J. Appl. Phys. **26**, 666 (1987).
- [22] P. M. J. Marée, K. Nakagawa, F. M. Mulders, and J. F. van der Veen, Surf. Sci. **191**, 305 (1987).
- [23] S. S. Iyer, J. C. Tsang, M. W. Copel, P. R. Pukite, and R. M. Tromp, Appl. Phys. Lett. **54**, 219 (1989).
- [24] E. Kasper and H. Jorke, in *Chemistry and Physics of Solid Surfaces*, edited by R. Vanselow and R. F. Howe (Springer Verlag, Berlin, 1988), p. 557.
- [25] J. C. Bean, L. C. Feldman, A. T. Fiory, S. Nakahara and I. K. Robinson, J. Vac. Sci. Technol. A **2**, 436 (1984).
- [26] P. R. Berger, K. Chang, P. K. Bhattacharya, J. Singh and K. K. Bajaj, Appl. Phys. Lett. **53**, 684 (1988).
- [27] H. J. Osten, J. Klatt, G. Lippert, B. Dietrich, and E. Bugiel, Phys. Rev. Lett. **69**, 450 (1992).
- [28] D. J. Eaglesham, F. C. Unterwald, and D. C. Jacobson, Phys Rev. Lett. **70**, 966 (1993).

- [29] H. J. Osten, J. Klatt, G. Lippert, E. Bugiel, and S. Hinrich, *Appl. Phys. Lett.* **60**, 2522 (1992).
- [30] M. Horn-von Hoegen, B. H. Müller, A. Al-Falou, and M. Henzler, *Phys. Rev. Lett.* **71**, 3170 (1993).
- [31] M. Copel, M. C. Reuter, M. Horn-von Hoegen, and R. M. Tromp, *Phys. Rev. B*, **42**, 11682 (1990).
- [32] B. Voigtländer, A. Zinner, T. Weber, and H. P. Bonzel, *Phys. Rev. B* **51**, 7583 (1995).
- [33] R. I. G. Uhrberg, R. D. Bringans, R. Z. Bachrach, and J. E. Northrup, *Phys. Rev. Lett.* **56**, 520 (1986).
- [34] D. H. Rich, T. Miller, G. E. Franklin, T.-C. Chiang, *Phys. Rev. B* **39**, 1438 (1989).
- [35] R. M. Tromp, and M. C. Reuter, *Phys. Rev. Lett.* **68**, 954 (1992).
- [36] D. Yu and A. Oshiyama, *Phys. Rev. Lett.* **72**, 3190 (1994).
- [37] F. K. LeGoues, M. Copel, and R. Tromp, *Phys. Rev. B*, **42**, 11690 (1990).
- [38] J. M. C. Thornton, A. A. Williams, J. E. Macdonald, R. G. van Silfhout, M. S. Finney, and C. Norris, *Surf. Sci.* **273**, 1 (1992).
- [39] P. C. Zalm, G. F. A. van de Walle, D. J. Gravesteijn, and A. A. van Gorkun, *Appl. Phys. Lett.* **55**, 2520 (1989).
- [40] K. Sakamoto, K. Kyoya, K. Miki, H. Matsuhata, and T. Sakamoto, *Jpn. J. Appl. Phys.* **32**, L204 (1993).
- [41] W. Rodrigues, O. Sakata, T.-L. Lee, D. A. Walko, D. Marasco, M. J. Bedzyk, *J. Appl. Phys.*, accepted for publication (2000).
- [42] S. Higuchi and Y. Nakanishi, *Surf. Sci. Lett.* **254**, L465 (1991).
- [43] X. W. Lin, Z. Liliental-Weber, J. Washburn, and E. R. Weber, A. Sasaki, A. Wakahara, and T. Hasegawa *J. Vac. Sci. Technol. B* **13**, 1805 (1995).
- [44] I.-S. Hwang, T.-C. Chang, and T. T. Tsong, *Phys. Rev. Lett.* **80**, 4229 (1998).
- [45] S. Higuchi and Y. Nakanishi, *J. Appl. Phys.* **71**, 4277 (1992).

- [46] T. Schmidt, J. Falta, G. Materlik, J. Zeysing, G. Falkenberg, and R. L. Johnson, *Appl. Phys. Lett.* **74**, 1393 (1999).
- [47] T. Hanada and M. Kawai, *Surf. Sci.* **242**, 137 (1991).
- [48] W. C. Fan, N. J. Wu, and A. Ignatiev, *Phys. Rev. B* **45**, 14167 (1992).
- [49] H. P. Noh, Ch. Park, D. Jeon, K. Cho, T. Hashizume, Y. Kuk, and T. Sakurai, *J. Vac. Sci. Technol. B* **12**, 2097 (1994).
- [50] Y. Qian, M. Bedzyk, P. F. Lyman, T. -L. Lee, S. Tang, and A. J. Freeman, *Phys. Rev. B*, **54**, 4424 (1996).
- [51] S. Tang, and A. J. Freeman, *Phys. Rev. B*, **50**, 1701 (1994).
- [52] B. W. Batterman, *Phys. Rev.* **133**, A759 (1964).
- [53] J. Zegenhagen, *Surf. Sci. Rep.* **18**, 199 (1993).
- [54] Y. Qian, Ph.D. Thesis, Northwestern University (1995).
- [55] A. Krolzig, G. Materlik, M. Swars, and J. Zegenhagen, *Nucl. Instr. and Meth.* **219**, 430 (1984).
- [56] R. S. Becker, J. A. Golovchenko, and J. R. Patel, *Phys. Rev. Lett.* **50**, 153 (1983).
- [57] R. Feidenhans'l, *Surf. Sci. Rep.* **10**, 105 (1989).
- [58] H. Dosch, B. W. Batterman, and D. C. Wack, *Phys. Rev. Lett.* **56**, 1144 (1986).
- [59] P. S. Pershan and J. Als-Nielsen, *Phys. Rev. Lett.* **52**, 749 (1984).
- [60] M. Born and E. Wolf, *Principles of Optics* (Pergamon Press, 1980).
- [61] A. Ishizaka and Y. Shiraki, *J. Electrochem. Soc.* **133**, 666 (1986).
- [62] T. N. Rhodin and J. W. Gadzuk, *The Nature of the Surface Chemical Bond*, pp 113–273 (North-Holland, 1979).
- [63] The LEED images are similar to that in figure 55.
- [64] J. Tersoff, C. Teichert and M. G. Lagally *Phys. Rev. Lett.*, **76**, 1675 (1996).

- [65] R. L. Headrick, J.-M Baribeau, D. J. Lockwood, and T. E. Jackman, M. J. Bedzyk, *Appl. Phys. Lett.* **62**, 687 (1993).
- [66] P. F. Lyman and M. J. Bedzyk, *Appl. Phys. Lett.*, **69**, 978 (1996).
- [67] V. A. Shchukin, N. N. Ledentsov, P. S. Kop'ev, and D. Bimberg *Phys. Rev. Lett.*, **75**, 2968 (1995).
- [68] M. Takahasi, S. Nakatani, T. Takahashi, X. Zhang, M. Ando, S. Fukatsu, and Y. Shiraki, *Jpn. J. Appl. Phys.* **34**, 2278 (1995).
- [69] J. Falta, D. Bahr, G. Materlik, B. H. Müller, and M. Horn-von Hoegen, *Appl. Phys. Lett.* **68**, 1394 (1996).
- [70] J. Hornstra and W. J. Bartels, *J. Cryst. Growth* **44**, 513 (1978).
- [71] M. J. Bedzyk, G. Materlik, *Phys. Rev. B* **31**, 4110 (1985).
- [72] P. F. Lyman, Y. Qian, T.-L. Lee, M. J. Bedzyk, *Physica B* **221**, 426 (1996).
- [73] N. W. Ashcroft and N. D. Mermin, , *Solid State Physics*, pp. 461 (Saunders College, 1976).
- [74] T.-L. Lee, Y. Qian, P. F. Lyman, J. C. Woicik, J. G. Pellegrino, and M. J. Bedzyk, *Physica B* **221**, 437 (1996).
- [75] X. Deng and M. Krishnamurthy, *Phys. Rev. Lett.* **81**, 1473 (1998).
- [76] R. S. Williams, G. M-. Ribeiro, T. I. Kamins, and D. A. A. Ohlberg, *J. Phys. Chem. B*, **102**, 9605 (1998).
- [77] T. I. Kamins, G. M-. Ribeiro, D. A. A. Ohlberg, and R. S. Williams, *J. App. Phys.*, **85**, 1159 (1999).
- [78] S. A. Chaparro, J. Drucker, Y. Zhang, D. Chandrasekhar, M. R. McCartney, and D. J. Smith, **83**, 1199 (1999)
- [79] M. Kästner and B. Voigtländer, *Phys. Rev. Lett.*, **82**, 2745 (1999).
- [80] J. Tersoff, F. K. LeGoues, *Phys. Rev. Lett.*, **72**, 3570 (1994).
- [81] F. M. Ross, J. Tersoff, R. M. Tromp, *Phys. Rev. Lett.*, **80**, 984 (1998).
- [82] M. Z-. Allmang, L. C. Feldman, M. H. Grabow, *Surf. Sci. Rep.*, **16**, 381 (1992)

- [83] G. M-. Ribeiro, A. M. Bratovski, T. I. Kamins, D. A. A. Ohlberg, and R. S. Williams, *Science*, **279**, 353 (1998).
- [84] T. I. Kamins, G. M-. Ribeiro, D. A. A. Ohlberg, and R. S. Williams, *Appl. Phys. A*, **67**, 727 (1998).
- [85] V. A. Shchukin, N. N. Ledentsov, P. S. Kop'ev, and D. Bimberg, *Sov. Phys. Semicond.*, **75**, 2968 (1995).
- [86] O. V. Kolosov, M. R. Castell, C. D. Marsh, and G. A. D. Briggs, *Phys. Rev. Lett.*, **81**, 1046 (1998).
- [87] H. T. Johnson and L. B. Freund, *J. Appl. Phys.*, **81**, 6081 (1997).
- [88] F. K. LeGoues, M. C. Reuter, J. Tersoff, M. Hammar, and R. M. Tromp, *Phys. Rev. Lett.*, **73**, 300 (1994).
- [89] J. A. Floro, G. A. Lucadamo, E. Chason, L. B. Freund, M. Sinclair, R. D. Twisten, and R. Q. Hwang, *Phys. Rev. Lett.* **80**, 4717 (1998).
- [90] M. Schmidbauer, Th. Wiebach, H. Raidt, M. Hanke, and R. Köhler, *Phys. Rev. B* **58**, 10523 (1998).
- [91] W. Dorsch, B. Steiner, M. Albrecht, H. P. Strunk, H. Wawra, G. Wagner, *J. Cryst. Growth*, **183**, 305 (1998).
- [92] Q. Xie, A. Madhukar, P. Chen, and N. P. Kobayashi, *Phys. Rev. Lett.* **75**, 2542 (1995).
- [93] T. I. Kamins and R. S. Williams, *Appl. Phys. Lett.* **71**, 1201 (1997).
- [94] T. I. Kamins, R. S. Williams, and D. P. Basile, *Nanotechnology* **10**, 117 (1999).
- [95] T. I. Kamins, D. A. A. Ohlberg, R. S. Williams, W. Zhang, and S. Y. Chou, *Appl. Phys. Lett.* **74**, 1773 (1999).
- [96] G. Jin, J. L. Liu, S. G. Thomas, Y. H. Luo, and K. L. Wang, *Appl. Phys. Lett.* **75**, 2752 (1999).
- [97] J. R. Heath, R. S. Williams, J. J. Shiang, S. J. Wind, J. Chu, C. D'Emic, W. Chen, C. L. Stanis, and J. J. Bucchignano, *J. Phys. Chem.* **100**, 3144 (1996).

- [98] U. Köhler, O. Jusko, B. Müller, M. Horn–von Hoegen, and M. Pook, *Ultramicroscopy* **42–44**, 832 (1992).
- [99] K. C. Pandey, in *Proceedings of the Seventeenth International Conference on the Physics of Semiconductors*, edited by J. D. Chadi and W. A. Harrison (Springer–Verlag, New York, 1985), p. 55.
- [100] Z. H. Cai, W. Rodrigues, P. Ilinski, D. Legnini, B. Lai, W. Yun, E. D. Issacs, K. E. Lutterodt, J. Grenko, R. Glew, S. Sputz, J. Vandenberg, R. People, M. A. Alam, M. Hybersten, and J. P. Ketelsen, *Appl. Phys. Lett.* **75**, 100 (1999).

Appendices

Appendix A

Shiraki Etch for Si

A.1 CP4 Etch

CP4 etch is performed to etch damaged or strained Si to render a strain-free Si substrate. The procedure is as follows:

Mix in a polyethylene bottle $\text{CH}_3\text{COOH}:\text{HNO}_3:\text{HF}$ (3:5:3). Carefully immerse the Si substrate to be etched with polyethylene tweezers. Add few drops of Br to increase the etch rate. Remove the Si substrate after 30 s and rinse with de-ionized (DI) water thoroughly. Repeat if necessary.

A.2 Shiraki Etch

Shiraki etching [61] is performed to remove contaminants from the Si growth surface and grow a thin, protective oxide layer before introducing the Si substrate into the UHV-MBE chamber. We used a slightly modified version of Shiraki etch as follows.

1. Boil Si substrate in conc. HNO_3 for 10 min. to remove any organic residue left after degreasing in acetone and methanol.

2. Treat for 5 min. in $\text{H}_2\text{O}:\text{NH}_4\text{OH}:\text{H}_2\text{O}_2$ (4:1:1) at 80°C
3. Rinse in DI water 3 times
4. Dip into $\text{H}_2\text{O}:\text{HF}$ (1:1) for 30 s at room temperature (RT)
5. Rinse in DI water 3 times
6. Treat for 5 min. in $\text{H}_2\text{O}:\text{HCl}:\text{H}_2\text{O}_2$ (5:1:1) at 80°C
7. Rinse in DI water 3 times
8. Repeat steps 4 to 7 twice
9. Dip into $\text{H}_2\text{O}:\text{HF}$ (1:1) for 30 s at room temperature (RT)
10. Rinse in DI water 3 times
11. Treat for 10 min. in $\text{H}_2\text{O}:\text{HCl}:\text{H}_2\text{O}_2$ (1:3:1) at 60°C
12. Rinse in DI water 3 times
13. Blow dry with nitrogen.

Use fresh chemicals each time and different containers for different solutions. Also use Teflon[®] tweezers to handle samples. The ratios are for volumes. The concentration of the chemicals used are HNO_3 (70%), NH_4OH (29%), HF (49%) and HCl (37%). As H_2O_2 evaporates very fast it should be replenished few times during each treatment.

Appendix B

MBE Control System

The collection of LEED images and Auger spectrum, and the annealing of the sample inside the chamber were controlled by a dedicated personal computer.

The LEED imaging system consisted of a Cohu[®] monochrome CCD camera with on-chip integration and a frame grabber PCI board and software for Windows95[®] from Scion[®]. The on-chip integration allows imaging even at lower light intensities.

The Auger spectrum collection and sample annealing is controlled by LabView[®] based data acquisition and control from National Instruments. Custom made graphical user interfaces (GUI) were prepared with programming in LabView. The GUI **Ramp.vi** controls the sample annealing and the GUI **Auspec.vi** is used to collect Auger spectrum. The GUI for Auger uses a dedicated pair of analog-to-digital converter (ADC) and digital-to-analog converter (DAC). The entire control system is shown in figure 61. The DAC output with a range from 0–6 V linearly controls the electron scan energy from 0–2040 eV for the Auger system. The analog Auger signal is digitized by the ADC and stored inside the computer. The GUI lets the user select the current energy in idle mode and in scanning mode accepts

start energy, final energy , number of scan points and signal integration time. It displays the signal in real time as it is being collected and also the previous Auger spectrum collected.

The GUI for sample annealing uses a DAC and reads temperature from the external pyrometer and the internal thermocouple (TC) next to sample inside the chamber. The DAC output with a range from 0–5 V linearly controls the current from 0–25 A following through the sample heating system. The user can control the filament current manually or ramp it automatically between two points in a specified amount of time. This is very useful for slowly heating or cooling the sample. There is also a feature to control the sample temperature as read by the pyrometer or the TC automatically.

The temperature of the two Knudsen cells is controlled by dedicated temperature controllers while the RGA is controlled by the computer using a RS232 serial connection.

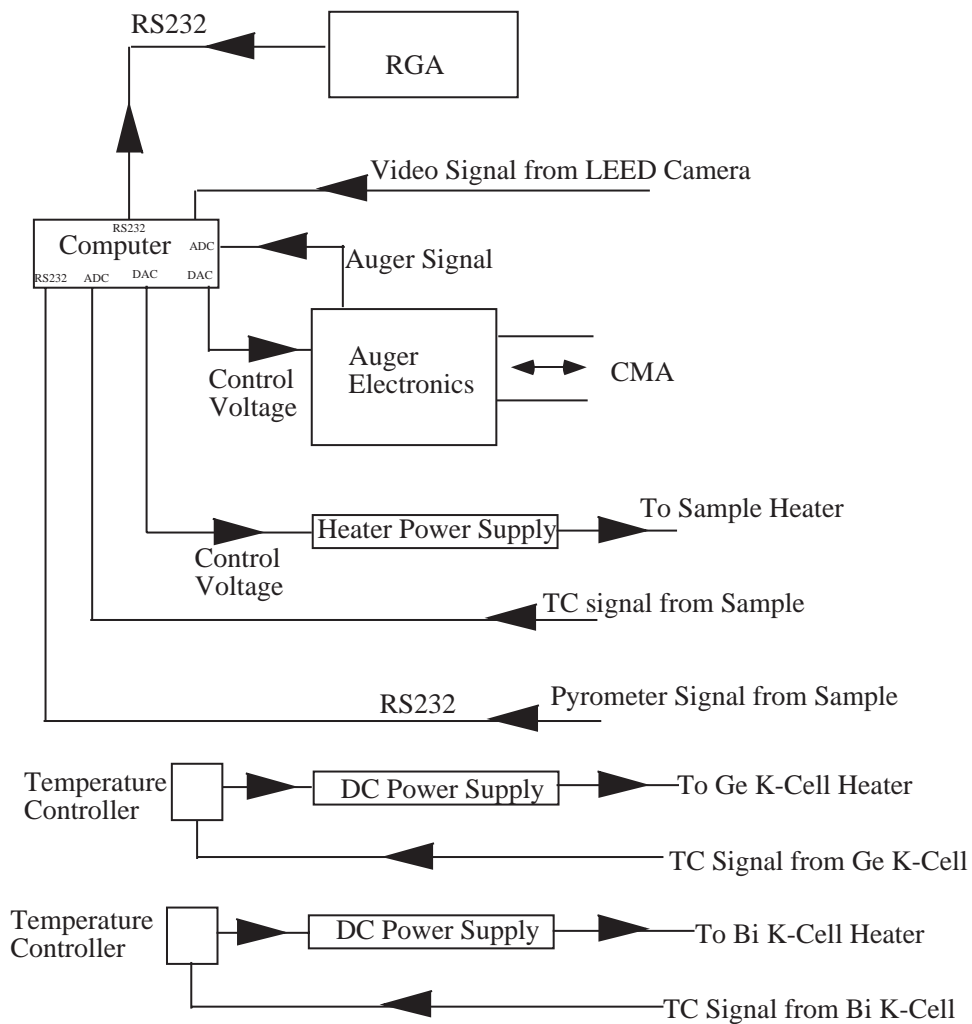


Figure 61: Control system for the LEED imaging, Auger, RGA, and sample and Knudsen cell heating on the UHV-MBE system.